UNIVERSITA' DEGLI STUDI DI PARMA
Dottorato di Ricerca in Scienze della Terra

XXIV CICLO- ANNO 2012

When the continental crust melts: a combined study of melt inclusions and classical petrology on the Ronda migmatites

Coordinatore:
Chiar.mo Prof. Renzo Valloni

Tutor:
Chiar.mo Prof. Sandro Meli

Tutor:
Chiar.mo Prof Bernardo Cesare

Tutor:
Chiar.mo Prof. Antonio Acosta-Vigil

Dottorando: Omar Bartoli

Abstract

Melt inclusions hosted in peritectic minerals of migmatites represent a novel and powerful small-scale tool to investigate the anatexis of the continental crust. In this thesis, taking advantage of a new experimental approach developed during this work, a combined study of classical petrology and melt inclusions in migmatites was performed to characterize in detail the composition and the physical properties of anatectic melts, the fluid regimes, and the melting mechanisms and conditions during the anatexis of the metasedimentary crust located below the Ronda peridotite (Betic Cordillera, S Spain). Here, the tectonic emplacement of mantle rocks within the continental crust produced high-temperature metamorphism and partial melting in the underlying metasedimentary rocks. The investigated migmatites are quartzo-feldspathic metatexites located towards the base of the crustal sequence and quartzo-feldspathic mylonitic migmatites found close to the contact with the peridotite.

The petrologic study was made by petrographic observations, compositional characterization of minerals and bulk rocks, conventional thermobarometry and pseudosection calculations. The quartzo-feldspathic migmatites are mainly composed of Qtz + Pl + Kfs + Bt + Sil + Grt and probably derived from a greywacke protolith. Muscovite, very rare in the metatexites, is absent in the mylonites. Graphite is present in all migmatites. The former presence of melt is recorded by melt inclusions and melt pseudomorphs at the microscale, and by peraluminous leucogranitic leucosomes at the mesoscale. The changes in phase compositions and modal contents from the metatexites to the mylonites, along with thermobarometric calculations and pseudosection modelling, are consistent with an increase of melting conditions and degree towards the contact with the peridotite.

Melt inclusions have been found in peritectic garnets of the investigated quartzo-feldspathic migmatites. A detailed study was carried out to characterize the microstructural features of melt inclusions and their chemical composition by microscope observation, FESEM imaging, piston cylinder experimental remelting, Raman and EMP analyses. The inclusions are primary in origin and were trapped within peritectic garnet during crystal growth. They are very small in size, mostly ≤ 10 μm,

and typically show a well-developed negative crystal shape. Three types of inclusions were identified: totally crystallized (nanogranites), partially crystallized and preserved glassy inclusions. Crystallized melt inclusions contain a granitic phase assemblage with quartz, feldspars and micas. In this study, a new approach for the experimental re-homogenization of melt inclusions was developed, performing remelting experiments at 5 kbar pressure using a piston cylinder apparatus. At the minimum re-homogenization temperature of 700 °C, most melt inclusions are completely re-homogenized. Conversely, melt inclusions display decrepitation cracks and CO_2 bubbles when remelted at higher experimental temperatures. For the first time, a pseudosection was constructed using the bulk composition of the fully re-homogenized melt inclusions from the metatexites. This approach constrained the melt entrapment at temperature close to the minimum re-homogenization temperature (T ~700 °C). The composition of those melt inclusions re-homogenized at 700 °C is comparable to that of preserved glassy inclusions in the same rock. In general all the studied melt inclusions in the migmatites and mylonites have peraluminous leucogranitic compositions. However, inclusions in the mylonites (mostly glassy) display quite variable Na_2O/K_2O and have lower primary H_2O contents (1.0-2.6 wt%) than melt inclusions in the metatexites (3.1-7.6 wt%).

Combining information from the melt inclusions and from the classical petrology allowed a better understanding of the melting processes occurred in the crustal sequence below the Ronda peridotite. The data collected in this study suggest that the crustal melting at Ronda mainly occurred under H_2O-undersaturated conditions by the continuous Bt dehydration melting reaction and at temperatures that did not exceed ~800 °C. In the metatexites, towards the base of the crustal sequence, crustal anatexis likely started at the solidus (T ~700 °C) in presence of H_2O-rich intergranular fluids. The growing peritectic garnets entrapped melt droplets produced at slightly different temperatures, whose composition was mainly diffusion-controlled. Melt inclusions seem to record the evolution of melt composition during prograde anatexis. Conversely, most of the peraluminous leucogranitic leucosomes are primary melts produced at, or close to, the metamorphic peak. The anatectic melts at Ronda have viscosity values greater than those commonly considered for granitic melts formed at

the same P-T conditions, implying much longer timescales for melt extraction and ascent through the metasedimentary crust at Ronda, as well as much greater strength of the migmatites.

The consistency of the collected compositional data along with the careful multidisciplinary approach adopted in this research, indicate that melt inclusions in peritectic minerals from migmatites represent a unique microstructure where anatexis is recorded and can be characterized *in situ*, in its earliest stage.

Riassunto

Le inclusioni di fuso silicatico in minerali peritettici di migamtiti rappresentano un nuovo strumento a disposizione dei petrologi per studiare il processo di anatessi della crosta continentale. Nel presente lavoro di tesi, grazie ad un nuovo approccio sperimentale sviluppato durante questa ricerca, è stato condotto uno studio combinato di petrologia classica ed inclusioni di fuso silicatico in migmatiti, per caratterizzare in dettaglio la composizione e le proprietà fisiche dei fusi anatettici, i regimi fluidi e le condizioni e i meccanismi di fusione durante l'anatessi della crosta meta sedimentaria, che si trova al di sotto delle peridotiti di Ronda (Cordigliera Betica, Spagna meridionale). In questa zona, l'impilamento tettonico di porzioni di mantello litosferico al di sopra di successioni di crosta continentale ha prodotto un metamorfismo di alta temperatura e innescato processi di fusione parziale nelle sottostanti rocce metasedimentarie. Le migmatiti studiate sono costituite da metatessiti quarzo feldspatiche, che affiorano verso la base delle sequenza crostale e da migmatiti milonitiche quarzo feldspatiche presenti in prossimità del contatto con le peridotiti.

Lo studio petrologico è stato condotto attraverso osservazioni petrografiche, caratterizzazione composizionale dei minerali e delle rocce, termobarometria convenzionale e pseudosezioni. Le migmatiti sono principalmente composte da Qtz + Pl + Kfs + Bt + Sil + Grt e probabilmente derivano da grovacche. La muscovite è rara nelle metatessiti e scompare nelle miloniti. La grafite è presente in tutte le rocce. La presenza di fuso anatettico nelle rocce studiate è testimoniata alla microscala da inclusioni di fuso silicatico e dalle pseudomorfosi di minerali su originari film di fuso e alla mesoscala da leucosomi leucogranitici peralluminosi. Le variazioni delle composizioni dei minerali e dei contenuti modali, i risultati dei calcoli termobarometrici e delle pseudosezioni indicano un aumento delle condizioni e del gradi di fusione dalla base della sequenza crostale verso il contatto con le peridotiti.

Le inclusioni di fuso silicatico sono state rinvenute nei granati peritettici delle migmatiti. La petrografia, le microstrutture e la composizione chimica delle inclusioni sono state caratterizzate attraverso l'uso del microscopio ottico e del microscopio elettronico a scansione con sorgente ad emissione di campo (FESEM), la rifusione

sperimentale con *piston cylinder* e le analisi alla microsonda elettronica (EMP) e in spettroscopia Raman. Le inclusioni di fuso silicatico hanno un'origine primaria e sono state intrappolate durante la crescita del granato. Esse hanno dimensioni ≤ 10 μm e spesso mostrano un'evidente forma a cristallo negativo. All'interno dello stesso granato, sono state individuate tre tipologie di inclusioni: completamente cristallizzate (nanograniti), parzialmente cristallizzate ed inclusioni vetrose preservate. Le inclusioni cristallizzate contengono una paragenesi mineralogica granitica caratterizzata da quarzo, feldspati e miche. In questo lavoro di tesi è stato sviluppato un nuovo approccio per la riomogeneizzazione sperimentale delle inclusioni di fuso silicatico, effettuando esperimenti di rifusione a 5 kbar di pressione con il *piston cylinder*. Alla temperatura minima di rifusione di 700 °C, molte delle inclusioni nei granati sono completamente riomogeneizzate. Le inclusioni invece sono decrepitate e contengono bolle di CO_2 quando vengono rifuse a più alta temperatura. Per la prima volta è stata costruita una pseudosezione utilizzando la composizione delle inclusioni completamente riomogeneizzate presenti nella metatessite. La pseudosezione indica temperature di intrappolamento del fuso silicatico molto vicine a quella minima di rifusione delle inclusioni (T ~700 °C). La composizione delle inclusioni riomogeneizzate a 700 °C è simile a quella delle inclusioni vetrose preservate nella stessa roccia. In generale, tutte le inclusioni di fuso silicatico nelle metatessiti e nelle miloniti hanno composizioni leucogranitche peralluminose. Tuttavia, molte delle inclusioni vetrose nella milonite mostrano un rapporto Na_2O/K_2O variabile e hanno contenuti primari di H_2O (1.0-2.6 wt %) più bassi delle inclusioni nella metatessite (3.1-7.6 wt%).

Una miglior comprensione dei processi di fusione si può avere combinando le informazioni ottenute dalle inclusioni di fuso silicatico e quelle dallo studio petrologico. I dati ottenuti in questo studio indicano che la fusione crostale a Ronda è avvenuta principalmente attraverso le reazione di fusione continua di deidratazione della biotite in condizioni di sottosaturazione di H_2O, a temperature più basse di 800 °C. Nelle metatessiti, verso la base della successione crostale, la fusione probabilmente è iniziata al *solidus* (T ~700 °C) in presenza di una fase intergranulare ricca in H_2O. Il granato peritettico che stava crescendo ha intrappolato delle piccole porzioni di fuso anatettico prodotto a temperature leggermente diverse, le cui composizioni erano controllate

principalmente dalla diffusione. Le inclusioni sembrano registrare l'evoluzione della composizione del fuso durante la storia prograda. Molti leucosomi leucogranitici peralluminosi, invece, rappresentano dei fusi primari prodotti in condizioni prossime a quelle del picco metamorfico. I fusi anatettici a Ronda hanno una viscosità più alta di quella comunemente considerata per fusi granitici prodotti alle stesse condizioni di pressione e temperatura. Questa caratteristica implica tempi molto più lunghi per l'estrazione di questi fusi anatettici e la loro ascesa attraverso la crosta metasedimentaria.

La consistenza dei dati composizionali ottenuti e l'accurato approccio multidisciplinare adottato in questa ricerca indicano che le inclusioni di fuso silicatico in minerali peritettici da migmatiti rappresentano l'unico strumento con cui studiare e caratterizzare le fasi più precoci dell'anatessi crostale.

Contents

Chapter 1
Partial melting (anatexis) of the continental crust

1.1 Introduction

Crustal anatexis, melt extraction and ascent to upper crustal levels promote the chemical differentiation (Hawkesworth and Kemp, 2006; Sawyer *et al.,* 2011; Brown et *al.,* 2011) and the weakening (Rosenberg and Handy, 2005; Jamieson *et al.,* 2011) of the Earth's continental crust (Fig. 1.1), with dramatic effects on tectonic processes, mountain building and geodynamics (Vanderhaeghe, 2001; Rosenberg and Handy, 2005; Jamieson *et al.,* 2011).

Crustal anatexis produces granitoid melts (Clemens, 2006) that can segregate from their source regions and migrate up to the Earth's surface (Fig. 1.1), with the formation of i) deeper-level residual granulitic terrains (Clemens, 1990; Vielzeuf *et al.,* 1990), ii) crustal S-type granites emplaced in the middle-to-upper continental crust (Clemens, 2003) and iii) felsic lavas (Clemens *et al.,* 2011; Di Martino *et al.,* 2011). Migmatites, which constitute former partially melted rocks where melt extraction was incomplete, dominate in the middle crust (Sawyer, 2008) and represent the zones of both melt generation and melt transfer (Brown, 2004).

Common crustal metasedimentary rocks (metapelites and metagreywackes) may start to melt when the temperature exceeds 650 °C. Water plays a significant role during anatexis, constraining melting conditions and reactions, and the production, composition and migration of granitic magma (Scaillet *et al.,* 1996; Clemens and Watkins, 2001; Holtz *et al.,* 2001; Sawyer *et al.,* 2011). If H_2O is present as a free fluid in the pores and grain boundaries of the rock, the process of melting is called fluid-present and takes place at lower temperatures. Melting can also occur without the presence of H_2O, when hydrous minerals (such as muscovite and biotite) break down at temperatures above 700-750°C (e.g., Clemens 2006, and references therein). This has been referred as to fluid-absent melting, hydrate-breakdown melting or dehydration melting (Thompson, 1982). The production of large volumes of granitic melt in the

continental crust is thought to occur mainly by fluid-absent melting, owing to the low porosity of the crystalline rocks at depth and thus the very little amount of fluid H_2O that they can contain (Clemens and Vielzeuf, 1987).

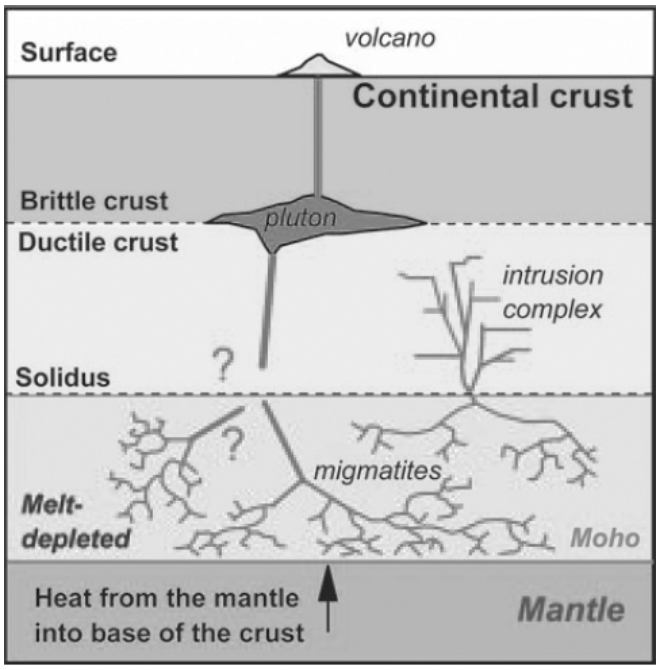

Figure 1.1: Schematic representation of reworking of continental crust by partial melting (modified after Sawyer *et al.,* 2011). See text for explanation.

1.2 Classical approaches to the study of crustal anatexis

The study of migmatites, granulites, S-type granites and rhyolitic lavas provides information on the partial melting of the continental crust. However, studies of natural anatectic rocks are limited by the fact that they constitute the end product of a range of metamorphic, magmatic and deformation processes that operate during their long-lived residence in the deep continental crust. For instance, migmatites and granulites undergo modifications of microstructures (Waters, 2001; Holness *et al.,* 2011) and phase assemblages (e.g., Kühn *et al.,* 2004) below their solidus. Leucosomes in migmatites, besides crystallizing upon cooling, do not commonly represent primary melts owing to reaction between melt and residual solids, entrainment of residual material, and fractional crystallization and cumulus phenomena (Sawyer, 2008 and references

therein). Moreover, compositional variations within, and between S-type granites and rhyolitic lavas have been adequately modelled by magma mixing (Di Vincenzo *et al.,* 1996; Collins and Hobbs, 2001) or entrainment of peritectic phases (Stevens *et al.,* 2007; Villaros *et al.,* 2009; Clemens *et al.,* 2011).

Due to the exposed limitations, the experimental petrology and thermodynamic modelling are used to obtain a snapshot of anatectic processes, advancing our understanding of partial melting of the continental crust. In the last 25 years numerous melting experiments have been performed, using natural and synthetic metasedimentary compositions and different P-T-a_{H2O} conditions (Le Breton and Thompson, 1988; Vielzeuf and Holloway, 1988; Holtz and Johannes, 1991; Patiño Douce and Johnston, 1991; Vielzeuf and Montel, 1994; Gardien *et al.,* 1995; Patiño Douce and Beard, 1995, 1996; Montel and Vielzeuf, 1997; Stevens *et al.,* 1997; Pickering and Johnston 1998; Patiño Douce and Harris, 1998). These studies provided constraints on P-T-a_{H2O} melting conditions, melting reactions, and melt production and composition. Most of the experimental melts have peraluminous, granitoid compositions that varies from granites to trondhjemites. They show low concentrations and rather limited variations in TiO_2, FeO and MgO, as well as high and variable Na_2O and K_2O concentations controlled by the composition of the source, P-T of melting and occurrence or absence of H_2O fluid. The melt compositions obtained in these experimental studies have been used in the geochemical modelling of migmatites and, more importantly, of the generation and differentiation of the continental crust (Solar and Brown, 2001; Guernina and Sawyer, 2003; Hacher *et al.,* 2011). However, experiments cannot reproduce Nature accurately, because there are many pitfalls and sources of uncertainty (summarized in White *et al.,* 2011). For instance, and regarding the composition of the melt, the low Fe contents found in the quenched glasses of most experiments might be due to Fe loss from the capsules (Lavaure and Sawyer, 2011).

An alternative to the experimental investigation of anatexis is to use quantitative thermodynamic calculations based on large, internally consistent datasets and complex activity models (Holland and Powell, 1998, 2003; White *et al.,* 2007). Thermodynamic modelling of melt-bearing equilibria can be applied to specific rock compositions via pseudosections (phase diagrams drawn for a fixed rock composition) and in increasingly

complex chemical systems (e.g., Na_2O-CaO-K_2O-FeO-MgO-Al_2O_3-SiO_2-H_2O-TiO_2 or NCKFMASHTO), providing a more comprehensive view of the phase relationships in rocks than the experiments (see White *et al.,* 2011). Pseudosection modelling is also recognized as a powerful tool to gain thermobarometric information on partially melted rocks because it provides a framework to interpret both textural information and mineral compositions in terms of P-T evolution (Tajcmanova *et al.,* 2006; Indares *et al.,* 2008; Groppo *et al.,* 2009). It is also possible to model the composition of the equilibrium melt produced at the onset of melting for the investigated chemical system and composition; this melt composition is calculated at the intersection of the solidus with a presumed prograde P-T path (Indares *et al.,* 2008; Groppo *et al.,* 2010), and can be added back to the bulk rock composition if the studied rock underwent loss of melt during its prograde evolution. With this re-integrated melt composition, a new pseudosection can be calculated allowing the investigation of the pre-peak history (White *et al.,* 2004; Indares *et al.,* 2008). Melt compositions obtained by thermodynamic calculations have also been used in the geochemical modelling of the migmatitic crust (White *et al.,* 2004). However, the comparison of experiments with thermodynamic calculations on the same compositions and chemical systems shows some differences regarding primarily the composition of the melt (White *et al.,* 2011). Indeed, the end-member thermodynamic properties of many minerals are relatively well constrained (Holland and Powell, 1998), but the activity-composition relationships (a-x) of solutions have significantly higher uncertainties, especially for the case of silicate melts (Holland and Powell, 2001; White *et al.,* 2007). In addition, these techniques have calculated melt compositions at equilibrium with the solid residual assemblage. However, kinetics may play an important role during crustal anatexis (Brearley and Rubie, 1990; Devineau *et al.*, 2005; Acosta-Vigil *et al.,* 2006a, 2006b)

Hence, the studies on crustal melting have currently a major unknown: the composition of anatectic melts in Nature.

1.3 A new approach: the study of melt inclusions in migmatites

Melt inclusions (MI) are small droplets of silicate liquid trapped in crystals that grow in a magma. They represent a powerful tool to gain information on several aspects of igneous processes operating in our tectonically active planet (Webster, 2006; Métrich and Wallace, 2008; Sobolev *et al.,* 2011).

The use of MI to provide a better understanding of crustal melting began with the pioneer studies on metasedimentary anatectic enclaves hosted in peraluminous dacites from the Neogene Volcanic Province (NVP) of S Spain (Cesare *et al.,* 1997; Cesare, 2008 and references therein). In this region, fragments of a partially melted mid-to-lower crust were rapidly brought to the Earth's surface and quenched during the ascent and submarine eruption of the host lavas. This case of "frozen migmatites" shows that droplets of granitic melt can be trapped by minerals growing during incongruent melting reactions (Cesare *et al.,* 2003, 2007; Acosta-Vigil *et al.,* 2007). Owing to the very fast cooling during the eruption, the trapped melt solidified to glass. The microstructural and geochemical characterization of these inclusions (Cesare *et al.,* 2003*,* 2007; Acosta-Vigil *et al.,* 2007, 2010; Ferrero *et al.,* 2011) support the hypothesis that the glass found within MI represents the anatectic melt produced in the rock during incongruent melting reactions at T > 700°C, and that the composition of such trapped melts can be representative of that of the bulk melt in the system during the anatexis of the rock.

Recently, Cesare *et al.* (2009) have showed that inclusions of anatectic melt can also occur in classic granulitic migmatites, as they have found crystallized MI in khondalites from the Kerala Khondalite Belt (KKB, India). These MI occur in peritectic garnets and show a granitic bulk composition rich in K, consistent with that expected from the partial melting of these rocks at the P-T conditions estimated by previous geothermobarometric studies (T~900°C and P~6-8 kbar; Cenki *et al.,* 2002; Shabeer *et al.,* 2005). The continuously-growing list of MI findings in migmatites from different geological settings (Cesare *et al.,* 2011; Ferrero *et al.,* 2012) includes the Ivrea-Verbano Zone, Ulten Zone and Argentera Massif (Italy), Adirondacks and Massachussetes (USA), Himalaya (Nepal) and Ronda (Spain), and suggests that anatectic MI are much less rare than expected and that they have been overlooked until now.

1.4 Aim of the study

Despite the long history of research on crustal anatexis (summarized in Brown, 2007 Sawyer, 2008), the retrieval of the chemical information on natural primary anatectic melts remains a challenging task, particularly at the onset of melting (see above). This is a major weakness of the current studies of crustal petrology, and may constitute as well a drawback of the modelling of the composition and evolution of the continental crust. The present work aims at providing important advances in this direction, performing an unprecedented combined study of MI and classical petrology on migmatites. This study shows how melt inclusions in migmatites have a great potential to obtain information on melt compositions and physical properties, fluid regime and melting mechanisms, compared with the conventional tools of crustal petrology.

This research was carried out as a multidisciplinary study, including field work in an anatectic terrain, petrographic observations, microstructural investigations at μm- and sub μm-scale, experimental petrology, and thermodynamic and geochemical modelling. This novel study allows to compare the information obtained from MI and that from the classical petrology, and shows an improved route to investigate the anatexis of the continental crust.

Chapter 2
A case study: Ronda migmatites (S Spain)

2.1 Geological setting

The Betic Cordillera (S Spain) represents the westernmost part of the peri-Mediterranean Alpine orogen, formed during the convergence of Africa and Eurasia from Late Cretaceous to Tertiary times (Dewey *et al.,* 1989). During this orogenic process, large bodies of subcontinental lithospheric mantle (Ronda Peridotites; Obata, 1980) have been exhumed and emplaced within the continental crust, in the Internal Zone of Betic Cordillera. The Internal Zone, also known as the Betic Zone, shows mainly metamorphic rocks of Paleozoic and Triassic age distributed in three main tectonic complexes that are, from the bottom to the top, the Nevado-Filábride, Alpujárride and Maláguide. This study focuses on anatectic rocks pertaining to the Alpujárride Complex of the western part of the orogen, and structurally located below the Ronda peridotites.

The Ronda peridotites, the largest worldwide exposure of subcontinental lithospheric mantle, belong to the Los Reales nappe, the highest structural unit of the Alpujarride Complex in the eastern Betic Cordillera. The peridotites constitute a slab up to 4 km thick that outcrops primarily in two massifs, Sierra Bermeja and Sierra Alpujata. The ultramafic slab was tectonically emplaced over two units, the Guadaiza and Ojen nappes, formed by metasedimentary sequences, in a syn-collisional tectonic setting (Tubia *et al.,* 1997). These two nappes have a typical Alpujarride lithological sequence with metapelites at the bottom and Triassic marbles at the top (Navarro-Vilá and Tubia, 1983). The metasedimentary sequence of the Ojen nappe seems to be inverted owing to the presence of overturned folds and the location of the metapelites structural above the marbles and in contact with the overlying peridotite slab (Tubia, 1988). The emplacement of mantle rocks produced high-temperature metamorphism and partial melting in the underlying crustal metasedimentary rocks, and the continued movement of the peridotites on top of the migmatites after they crossed the solidus

during the retrograde path produced the mylonites at the contact (Tubia and Cuevas, 1986; Tubia *et al.,* 1997; Acosta-Vigil *et al.,* 2001). Hence from top to bottom, the Ojen nappe is composed of mylonites, migmatites, schists and marbles. This thesis provides observations about the petrology and geochemistry of migmatites and mylonites. The lithological association (including migmatites) and metamorphic features of the Alpujarride Complex resemble those of metamorphic basement found beneath the Alboran Sea (Soto and Platt, 1999).

In the dynamothermal aureole located below the Ronda peridotites, the intensity of metamorphism, deformation and the extent of melting increase towards the contact with the overlying mantle rocks. Thus, the migmatites (hereafter Ronda migmatites) range from metatexites, through diatexites, to mylonitic migmatites (Tubia *et al.,* 1997; Acosta-Vigil *et al.,* 2001). Based on mineral proportions and whole-rock geochemistry, the Ronda migmatites have been grouped into pelitic and quartzo-feldspathic (Acosta, 1998; Acosta-Vigil *et al.,* 2001). Undeformed and deformed leucogranite dykes, liekly related to the partial melting of the metasedimentary rocks, crosscut the peridotites (Tubía and Cuevas, 1986; Acosta-Vigil *et al.,* 2001; Cuevas *et al.,* 2006) and are particularly abundant in the Sierra Alpujata massif. There seems to be a general agreement about an Early Miocene age for the tectonic emplacement of the peridotites into the crust (Loomis, 1975; Priem *et al.* 1979; Zindler *et al.,* 1983; Platt and Whitehouse, 1999). However, the latest evaporation and SHRIMP studies on zircons (Acosta, 1998; Sánchez-Rodríguez, 1998; Acosta-Vigil *et al.,* 2011) have yielded both Hercynian (~300 Ma) and Alpine (~20 Ma) magmatic ages, suggesting the existence of two different anatectic events separated in time in the rocks underlying the Ronda peridotites.

2.2 Sampling and petrologic outline

The studied samples come from the Ojen nappe, in the Sierra Alpujata massif (Fig. 2.1). Here, the Ronda migmatites are exposed along the northern and western side of Sierra Alpujata, and are bounded by schist and marbles to the north and west (located structurally below the migmatites), and by the peridotites to the south and east (above the migmatites). The thickness of the migmatitic and metasedimentary sequence change

along different traverses (up to ~700m; Tubia *et al.,* 1997). Migmatites were collected in the northwestern side of the Sierra Alpujata massif (Fig. 2.1), roughly along the Los Villares transect of Tubia *et al.* (1997). In this sector the dynamothermal aureole consists, from the top to the bottom, of i) mylonitic garnet-cordierite granulites (kinzigites) in contact with the peridotites, ii) quartzo-feldspathic mylonites and iii) quartzo-feldspathic and pelitic diatexites, and iv) quartzo-feldspathic and pelitic metatexites (Fig. 2.2).

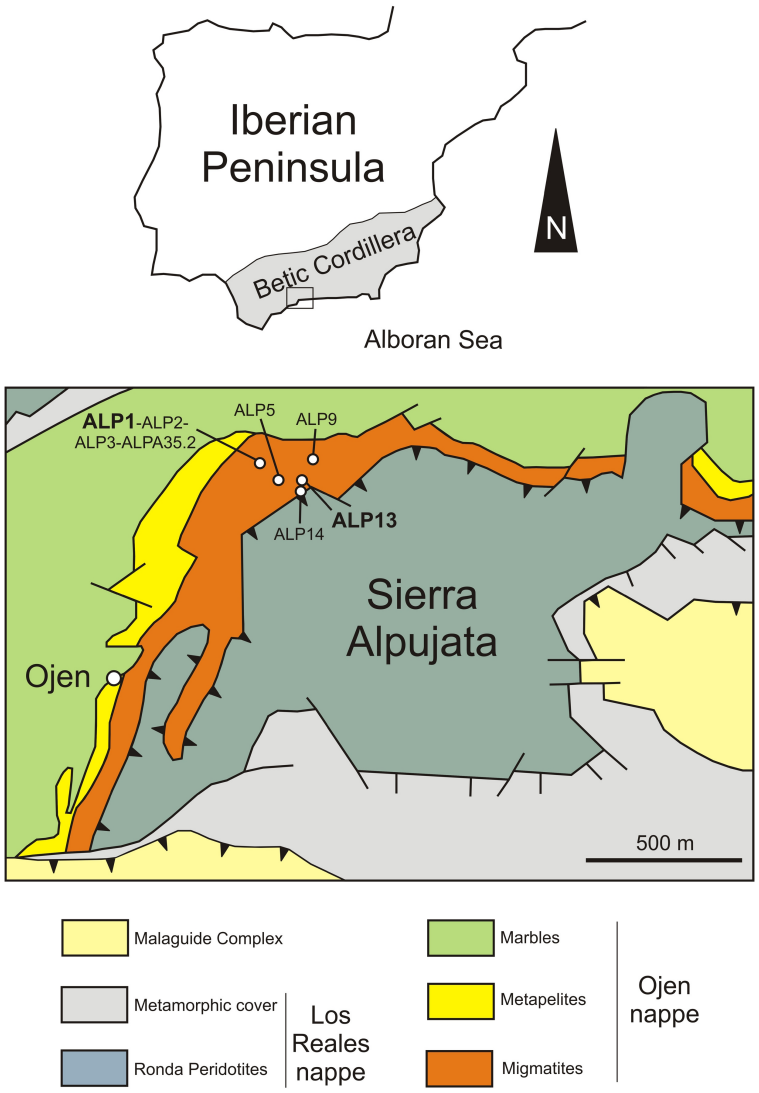

Figure 2.1: Geological map of the Sierra Alpujata massif, showing the location of the studied samples (redrawn after Esteban *et al.,* 2011). ALP1, ALP2, ALP3 and ALPA35.2: metatexites. ALP5 and ALP9: diatexites. ALP13 and ALP14: mylonites.

This study is primarily focalized on the quartzo-feldspathic mylonites and metatexites (labeled in bold in Fig. 2.1). Tubia *et al.* (1997) reported also the presence of amphibolites and some marbles and quartzites in the lowermost part of the aureole and of garnet-biotite-sillimanite schists in the metasedimentary sequence just below the migmatites. This lower contact is characterized by a band (up to 5 m thick) with intensely retrograded migmatites and chlorite-rich schists (Tubia *et al.,* 1997). Amphibolite bands preserve some eclogite-facies assemblages related to an earlier stage of subduction (Tubia and Ibarguchi, 1991). Most of the ductile deformational structures in the crustal sequence indicate a ENE-ward shearing and the orientation of planar and linear structures in quartzo-feldspathic mylonites is concordant with that observed in the overlying peridotitic mylonites (Tubia *et al.,* 1997).

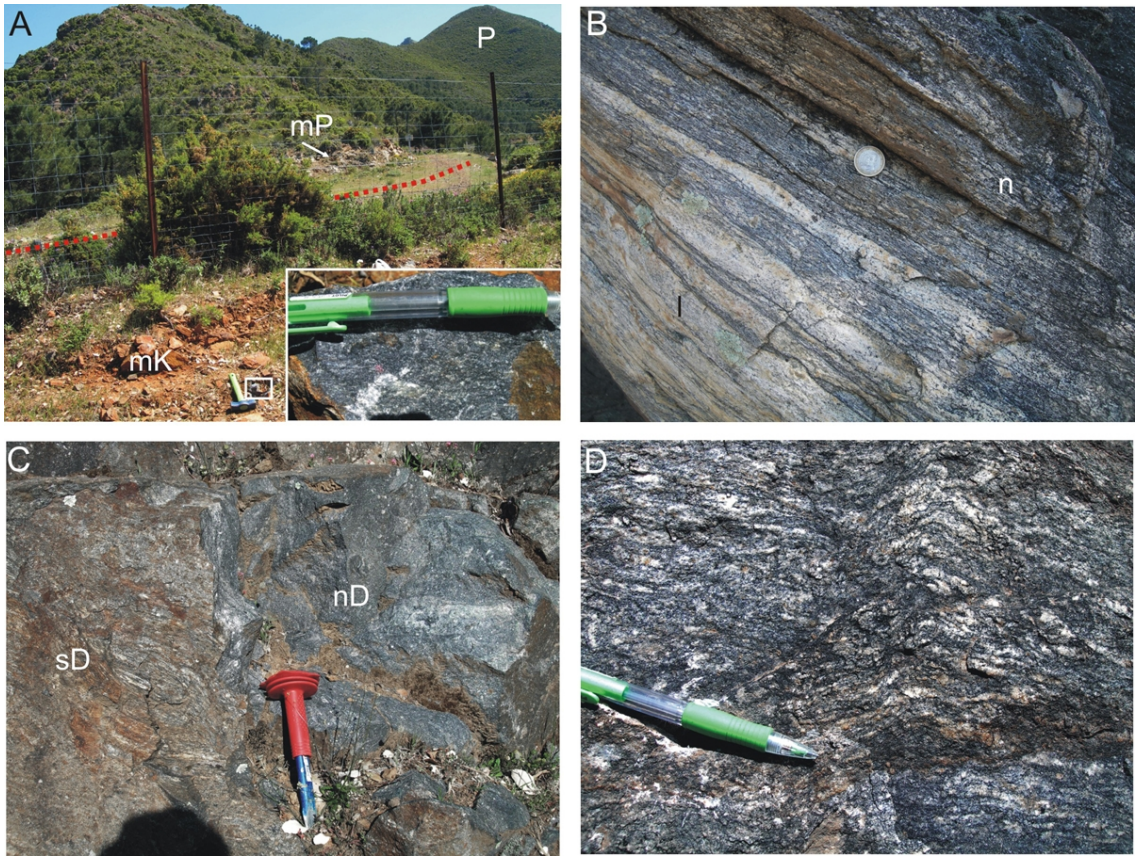

Figure 2.2: Field photographs. (A) Tectonic contact (red line) between the mantle rocks (mP: mylonitic peridotite; P: peridotite) and the mylonitic kinzigite (mK) of the crustal sequence. White box: close-up of the mylonitic kinzigite ALP14. (B) Quartzo-feldspathic mylonitic migmatite ALP13. l: leucosome; n: neosome. (C) Pelitic diatexite ALP9. sD: schlieren diatexite; nD: nebulitic diatexite. (D) Quartzo-feldspathic stromatic metatexite ALP1.

At Sierra Alpujata, the anatectic rocks below the Ronda peridotites show an evolution from HP-HT to LP-HT conditions (Tubia and Cuevas, 1986; Tubia *et al.,* 1997). Tubia *et al.* (1997) suggest a metamorphic peak conditions of 795±25 °C and 8.3±0.7 kbar for the quartzo-fedspathic mylonites at the contact, with a second metamorphic stage at 685±15 °C and 5.5±1.1 kbar. The same authors obtained conditions around 680± 30°C and 4.2±0.2 kbar for the formation of cordierite after garnet in deformed granitic dykes. Mylonitization in peridotites began at HP-HT conditions (800-1000 °C and 11 kbar; Tubia and Cuevas, 1986; Tubia *et al.,* 1997). Tubia and Cuevas (1986) suggest the presence of two partial melting events in the Ojen crustal sequence. A first event at ~725 °C and ~7 kbar produced the biotite-sillimanite-garnet association in migmatites and the Grt-, Crd-bearing leucogranitic dykes cross-cutting the peridotites, later deformed. A late melting event developed at ~750 °C and ~3.5 kbar leading to formation of undeformed tourmaline-bearing leucogranitic dykes.

Despite the studies performed by Tubia and Cuevas (1986) and Tubia *et al.* (1997), crustal anatexis at Sierra Alpujata is still poorly constrained, especially the characterization of melting reactions and conditions, fluid regimes and melt compositions through the migmatitic sequence.

Chapter 3
Analytical methods

The petrographic analysis was made with optical microscopes both in transmitted and reflected light.

Back scattering electron (BSE) imaging and semi-quantitative energy dispersive spectroscopy (EDS) were carried out with several scanning electron microscopes: 1) CAM SCAN MX2500, equipped with LaB6 cathode, at the Dipartimento di Geoscienze, Università di Padova (Italy); 2) Jeol JSM–6500F thermal FESEM, at INGV (Istituto Nazionale di Geofisica e Vulcanologia), Rome, Italy; 3) FEI Quanta 600 FEG, equipped with a Bruker EDX–Silicon Drifted Detector, at the Nanoscale Characterization and Fabrication Laboratory, ICTAS (Institute for Critical Technology and Applied Science), Virginia Tech, USA; 4) Sigma Zeiss Field Emission SEM equipped with Oxford XMax EDS–Silicon Drifted detector at CNR–IENI, Padova (Italy). Backscattered electron images were acquired at variable magnifications and variable accelerating voltage, commonly from 8 to 15 kV. Elemental X–ray maps were acquired at 20 and 15kV accelerating voltage and at variable magnifications, in the range 5000–6000X, depending on the MI size, using the FEI Quanta 600 FEG available at ICTAS (Virginia Tech, USA).

The chemical composition of glass in MI was obtained using a Jeol JXA 8200 Superprobe equipped with 5 spectrometers at the Dipartimento di Scienze della Terra, Università di Milano (Italy). Analytical parameters were: 15 kV accelerating voltage, 2 nA current, 1 µm beam diameter, counting time of 10 s on peak and 2 s on background. Na, K, Al and Si were analyzed first. Natural and synthetic silicates and oxides were used as standards. Owing to the loss of Na during the electron microprobe analysis of rhyolitic glasses with consequences also on the measured contents of K, Al and Si (Morgan and London, 1996 and 2005), concentrations were corrected using conservative factors obtained by the analysis of granitic glass standards of known composition with variable H_2O content at the same working conditions.

The compositions of muscovite, biotite and feldspars were obtained using a Jeol JXA 8200 Superprobe at the Dipartimento di Scienze della Terra, Università di Milano (Italy). Analytical parameters were: 15 kV accelerating voltage, 5 nA current, counting time of 30 s on peak and 10 s on background. Garnet compositions were determined using the Cameca SX50 microprobe of the C.N.R.-I.G.G. (Consiglio Nazionale delle Ricerche-Istituto di Geoscienze e Georisorse), located at the Dipartimento di Geoscienze, Università di Padova, Italy. Measurements were performed using 20 kV accelerating voltage, 20 nA beam current, counting time of 10 s on peak and 5 s on background. Natural and synthetic silicates and oxides were used as standards.

Whole rock analyses of major elements and some trace elements were performed by X-ray fluorescence (XRF), employing a Pan-Alyitical XRF Spectrometer PW2400 at the Dipartimento di Geoscienze, Università di Padova (Italy).

Raman spectroscopy was performed to determine H_2O contents of the glassy MI exposed on the garnet surface, following the first method proposed by Thomas (2000), which is based on the linear relationship between the H_2O content of rhyolitic glass and the intensity of the asymmetric OH stretching band at 3550 cm^{-1}. H_2O content of melt inclusions was determined using a Jobin Yvon Horiba HR 800 Labram confocal Raman microprobe equipped with an Olympus BX 41 petrographic microscope, at the Fluids Research Laboratory, Department of Geosciences, Virginia Tech (USA). The excitation source was a 514.57 nm (green) Laser Physics 100S-514 Ar^+ laser. The analytical settings were a 150 µm slit width, 400 µm confocal aperture, 600 grooves/mm gratings, 100x objective, 3x accumulations, 100 s acquisition time for re-homogenized MI in metatexites and 200 s acquisition time for the preserved glassy MI in mylonite. Spectra were collected between 2600 cm^{-1} and 4000 cm^{-1}. The area under the 3550 cm^{-1} peak was determined after baseline correction. The calibration procedures were performed using a natural (LGB; Behrens and Jantos, 2001) and six synthetic (Ab1-0, Ab1-5, Ab1196A, 040281I, 032481VII and 022881XII; Severs *et al.*, 2007) glasses with known H_2O contents, ranging between 0.98 and 10.11 wt%. The data fit on straight lines (Fig. 3.1) indicating the linear relationship between the H_2O content in glass and the area under the asymmetric OH stretch band at 3550 cm^{-1}. Before and after each MI analysis the Raman calibration was verified using one of synthetic glasses described above.

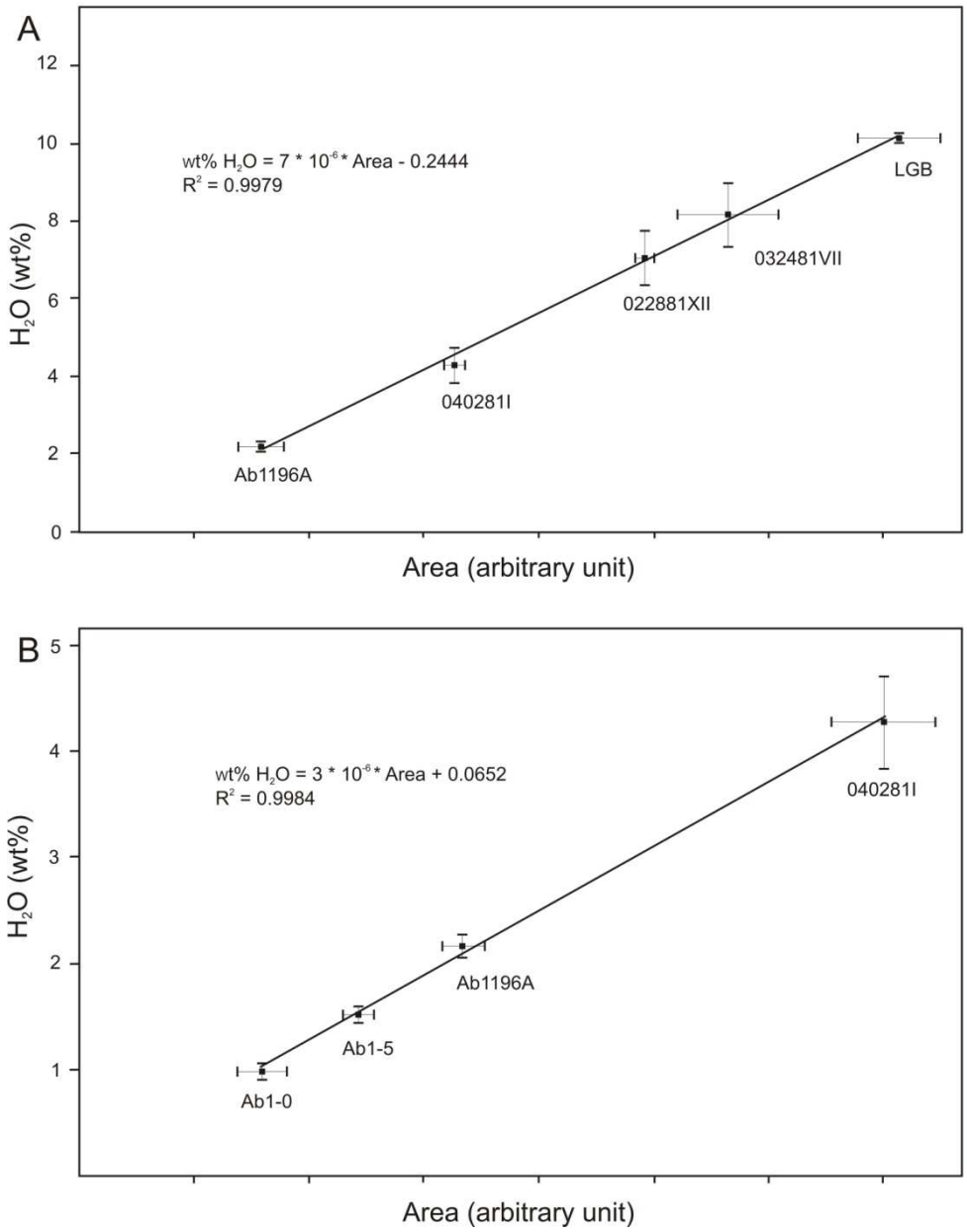

Figure 3.1: Raman calibration curves for the H_2O quantification in re-homogenized MI of metatexite (A) and in glassy MI of mylonite (B), showing the linear relationship between the H_2O content of hydrous glasses and the area under the 3550 cm^{-1} peak. Horizontal bars indicate the standard deviation (1σ) after 3 replicated analyses. Vertical bars represent the analytical errors on H_2O quantification in the glass standards from literature (Behrens and Jantos, 2001; Severs *et al.*, 2007).

Bubbles in MI remelted at 750 and 800 °C were analyzed using the same Raman instrument described above and available at Fluids Research Laboratory, Department of Geosciences, Virginia Tech (USA). The analytical settings for these analyses were a

150 µm slit width, 400 µm confocal aperture, 600 grooves/mm gratings, 100x objective, 3x accumulations and 30 s acquisition time. Spectra were collected between 100 cm^{-1} and 4000 cm^{-1}. CO_2 density was determined from the Raman spectra according to the method based on the dependence of the CO_2 Fermi diad splitting from density (Fall *et al.*, 2011). The position of Raman lines was determined after baseline correction.

Raman hyperspectral images of liquid-H_2O distribution in crystallized MI were obtained with a Labram Raman instrument (Horiba, Jobin-Yvon), equipped with a Peltier-cooled CCD detector and a polarized 514.5 nm Ar^+ laser at the Dipartimento di Scienze della Terra, Università di Siena (Italy). The laser power was 300 mW at the source, and the slit width was 200 µm, with a spectral resolution of 1.5 cm^{-1}. Raman spectra were collected through an excitation spot of 1x1x5 µm in volume (100x objective, n.a.=0.9). Acquisition time was 40 s. Hyperspectral images were collected following a regular grid of points equidistant 1 µm in both directions, using a computer-controlled, automated X-Y mapping stage (Horiba, Jobin Yvon).

Chapter 4
Experimental approach for the remelting of melt inclusions

4.1 Classical techniques

In igneous petrology, various techniques have been used to homogenize the MI, including heating in one-atmosphere furnaces (Student and Bodnar, 1999; Fedele *et al.*, 2003), homogenization using low-pressure (cold-seal) vessels (Skirius *et al.*, 1990; Anderson *et al.*, 2000; Thomas *et al.*, 2003; Student and Bodnar, 2004) and heating in a microscope-mounted high temperature stage (Frezzotti, 1992; Salvioli-Mariani *et al.*, 2002). Each of these techniques has advantages and disadvantages, as described by Bodnar and Student (2006).

4.2 Heating stage

The first re-homogenization experiments of MI in the metatexites were performed at the Laboratorio di Inclusioni Fluide (Dipartimento di Scienze della Terra dell'Università di Parma, Italy) using a LINKAM TS1500 high temperature and room pressure stage, in an inert atmosphere of He to prevent sample oxidation. A temperature correction factor was applied, after having determined a calibration curve with different standards: $K_2Cr_2O_7$, Ag and Au with a melting temperature of 398°C, 962°C and 1064°C, respectively. The accuracy of measurements is ± 15°C. A few tens of chips containing MI-bearing garnets were separated from double-polished thick (~200 µm) sections. The samples were heated up to 500°C with a rate of 50°C/min, followed by 2 hours stop. Then the MI were heated at 40°C/min up to the beginning of melting and the samples were held at the maximum temperature for 5-15 minutes before quenching with liquid nitrogen. The remelting temperature obtained through this approach is about 860°C. A different heating ramp was then selected to try to avoid the MI decrepitation and to reduce the remelting temperature. Using a rate of 30°C/min the samples were heated up to 500°C with stop of 30 min. Then, MI were heated at 20°C/min up to 650°C

with stops of 10 min every 50°C, and finally with a rate of 10°C/min up to the observed melting temperature with stops of 5 min every 25°C. The samples were held at the maximum temperature for 5-10 minutes before quenching. The remelting temperature obtained through this approach is about 780°C.

4.3 Piston cylinder

To avoid inclusion decrepitation, melt-host interaction and volatile loss, a new approach for the MI experimental re-homogenization was subsequently adopted. MI remelting experiments were performed using a single-stage piston cylinder apparatus (Fig. 4.1A) at the Laboratorio di Petrologia Sperimentale, Dipartimento di Scienze della Terra, Università di Milano, Italy.

Single garnet crystals were obtained by initial crushing of the rock followed by steps through an agate mortar mill. The powder was sieved and the crystals with grain-size between 50 and 200 µm were passed through the Frantz isodynamic magnetic separator at Dipartimento di Scienze della Terra, Università di Parma (Italy). A 100% pure garnet concentrate was obtained by hand-picking under a binocular microscope.

After garnet separation, single garnet crystals were loaded into Au capsules (Ø=3 mm) alternating them with powdered silica (Fig. 4.1B and C). Bi-distilled water (~10 wt %) was added in some capsules to evaluate the potential effects of H_2O diffusion in and out of the MI during experiments. The capsules were crimped and sealed by arc welding using a wet tissue around the capsule to prevent H_2O loss. No weight loss of capsules with added H_2O was observed after repeated heating at ~100°C. For each run, three capsules (two dry and one wet) were embedded in MgO-salt (Fig. 4.1D), and a low friction assembly consisting of NaCl sleeve and graphite heater was used. The experiments were run at 5 kbar, 700, 750 and 800°C for 24 h. The temperature was controlled by K-type thermocouples and is considered accurate to ±5°C. Pressure was measured by a load cell into the frame (Johannes-type piston cylinder) and is accurate to ±0.4 kbar. At the end of the experiments, the capsules were quenched and mounted in epoxy and the inclusions in the garnet were exposed by polishing (Fig. 4.1C). An aqueous fluid bubbling out of the capsules with added H_2O was observed during capsule opening.

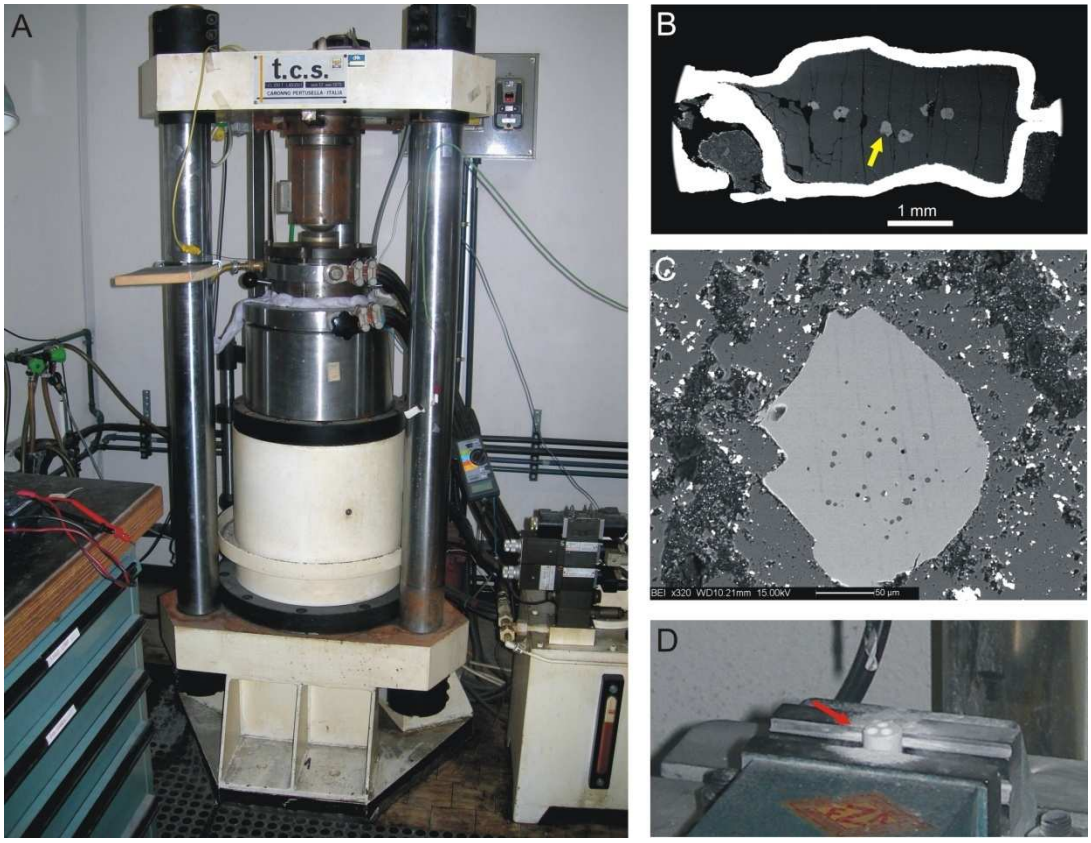

Figure 4.1: (A) Piston cylinder apparatus used for remelting experiments of partially crystallized and nanogranite inclusions. (B) Gold capsule containing garnet crystals (yellow arrow) and re-crystallized SiO_2. (C) Garnet surrounded by SiO_2+Au matrix after remelting experiment. (D) Preparation of a MgO-salt (red arrow). Three holes have been done to accommodate three garnet-bearing capsules.

Chapter 5
Petrology and geochemistry of quartzo-feldspathic metatexites and mylonitic migmatites

5.1 Petrography

Quartzo-feldspathic metatexites and mylonitic migmatites are composed of varying modal amounts of quartz, plagioclase, K-feldspar, biotite, sillimanite and garnet, with minor amounts of graphite, ilmenite, apatite and muscovite. Here, according to Sawyer (2008), the terms used to refer to the domains of a migmatite have the following meaning: “leucosome” will refer to the lighter-colored part derived from the crystallization of the segregated partial melt, whereas “melanosome” will refer to the darker-colored part that represents the solid, residual fraction left after melt segregation. Sawyer (2008) suggested to abandon the term “mesosome”, because it has no unique genetic significance. Hence, the mesocratic portions in the studied migmatites are named “neosome”, as they constitute domains of the pre-anatectic rock that have partially melted and where the melt fraction has not been completely removed.

The metatexites have a stromatic appearance (Fig. 5.1A) with thin (< 1 cm) discontinuous leucosomes surrounded by a fine-grained mesocratic matrix (neosome) with the assemblage biotite, fibrolitic sillimanite, garnet, graphite, quartz, plagioclase, K-feldspar, apatite and ilmenite (Fig. 5.1B). Sometimes melanosomes, formed mostly by biotite and fibrolitic sillimanite, appear at the interface between leucosome and neosome. Leucosomes, occuring sub-parallel to the foliation defined by biotite and fibrolite (Fig. 5.1A), are fine- to medium-grained and contain quartz, plagioclase, K-feldspar, biotite and rare garnet (Fig. 5.1C). Feldspars in the leucosomes are often antiperthitic or perthitic; they may include quartz and garnet and generally have anhedral to subhedral habit (Fig. 5.1C), although some euhedral crystals are present (Fig. 5.1D). Biotite lamellae are abundant, generally clustered with fibrolite, and show a preferred orientation that defines the foliation (Fig. 5.1B).

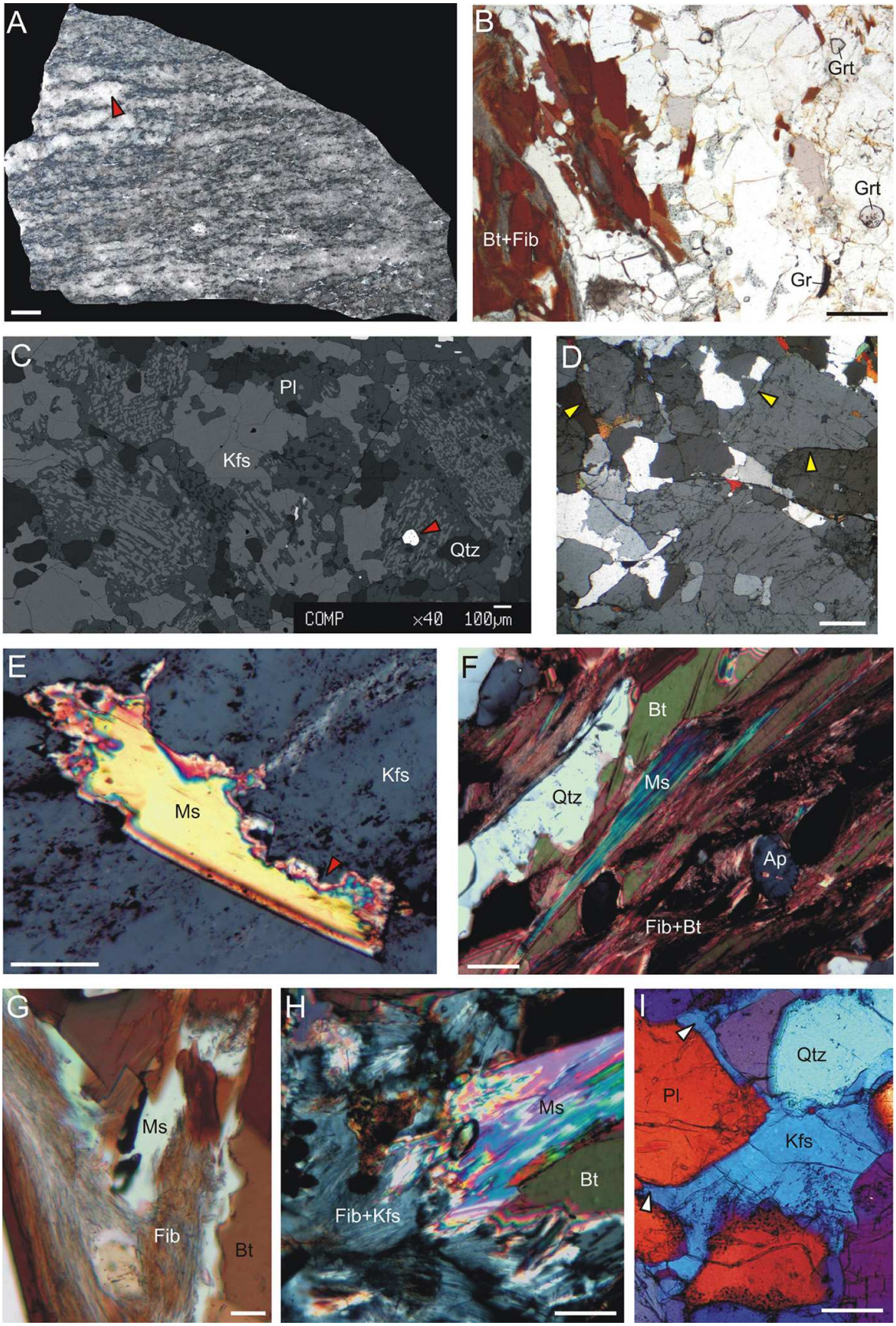
A
B
Grt
Grt
Bt+Fib
Gr
C
Pl
Kfs
Qtz
COMP
×40
100μm
D
E
Kfs
Ms
F
Bt
Qtz
Ms
Ap
Fib+Bt
G
Ms
Fib
Bt
H
Ms
Bt
Fib+Kfs
I
Qtz
Pl
Kfs

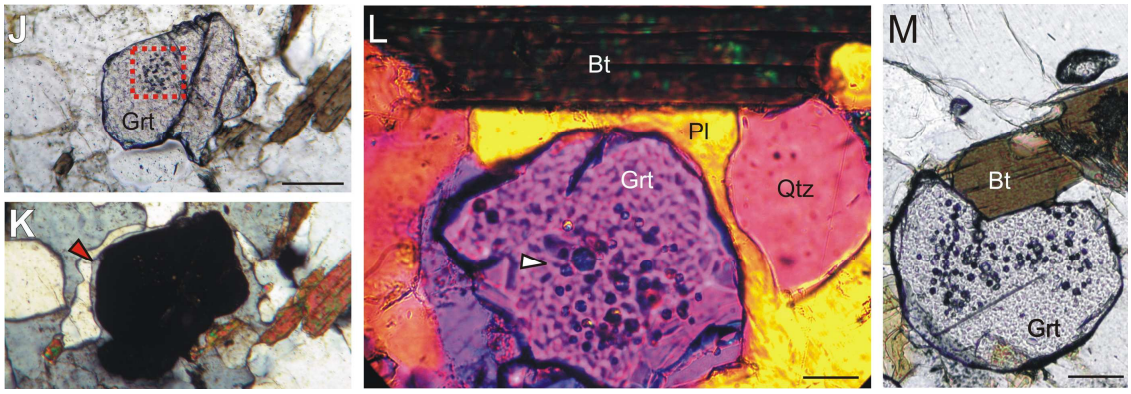

Figure 5.1: Microstructures in the quartzo-feldspathic metatexites. A) Discontinuous leucosomes (red arrow) surrounded by a fine-grained neosome. Scalebar: 1 cm. B) PPL photomicrograph of the mesocratic portion. Scalebar: 300 µm C) SEM-BSE image of a leucosome, containing mainly antiperthitic and perthitic feldspars. Red arrow: MI-bearing garnet. D) Grains of euhedral feldpsars (yellow arrows) in a leucosome, XPL. Scalebar: 100 µm. E) Muscovite included in K-feldspar porphyroblast; XPL. Scalebar: 100 µm. Muscovite crystal with irregular boundaries (red arrow), suggesting that it was resorbed during K-feldspar growth. F) Muscovite associated with fibrolite and biotite in the neosome matrix; XPL. Scalebar: 100 µm. G) XPL Photomicrograph showing primary muscovite partially replaced by fibrolite in the neosome; scalebar: 50 µm. H) Fibrolite and K-feldspar grown on primary fabric-forming muscovite; XPL. Scalebar: 150 µm. I) Melt pseudomorph: K-feldspar with cuspidate outlines (white arrows) that has probably crystallized from a film of melt. The reactant minerals, quartz and plagioclase, are rounded and resorbed (i.e., consumed). XPL with 530 nm λ plate; scalebar: 150 µm. J and K) Subhedral garnet containing a cluster of MI at the core (red box in J) and surrounded by plagioclase that crystallized as a melt pseudomorph (red arrow in K). J PPL and K XPL. Scalebar: 75 µm for both. L) Plagioclase crystallized as a melt pseudomorph in the neosome matrix, between biotite, quartz and garnet. White arrow: MI in garnet. XPL with 530 nm λ plate; scalebar: 30 µm. M) MI-bearing garnet partially replaced by biotite; PPL. Scalebar: 30 µm. Fib: fibrolite. Other mineral abbreviations are after Kretz (1983).

In the leucosome, biotite is interstitial between feldspars and quartz. Muscovite is very rare, and appears included in K-feldspar porphyroblats (Fig. 5.1E) or associated with biotite and fibrolite in the neosome (Fig. 5.1F). Fibrolite apparently grew on primary muscovite (Figs. 5.1G and H). Graphite is scattered in the neosome matrix, whereas ilmenite and apatite are generally surrounded by biotite and fibrolite aggregates. Plagioclase in the neosome is typically finer-grained than in the leucosomes. Alkali feldspar in the neosome is often poikiloblastic and may contain solid inclusions of quartz, plagioclase, biotite, garnet, fibrolite and muscovite. However, garnet and muscovite have never been found included in the same K-feldspar porphyroblast. Myrmekites are commonly present along the K-feldspar boundaries. The neosome contains irregularly shaped domains of feldspars with cuspate outlines (Fig. 5.1I); the adjacent minerals (quartz and plagioclase) are rounded, probably owing to dissolution.

Garnet occurs mostly in the neosome as small subhedral to euhedral crystals (80-200 µm in diameter). It occurs in very low modal amount (<1%) and contains clusters of several melt inclusions (Figs. 5.1J and K). In places garnet may be i) surrounded by thin film of plagioclase or quartz (Figs. 5.1J-L); or ii) partially replaced by biotite or biotite and fibrolite (Fig. 5.1M).

Microstructures indicate that this mylonite represents a partially melted quartzo-feldspathic rock which was affected by deformation both during migmatization and after the rock crossed the solidus during the retrograde path. Nevertheless, the main parts of the original migmatite (leucosome, neosome and melanosome) are still recognizable, and I will refer to them during the description of this sample. This rock consists of alternating bands of well-discernible leucosome and neososome, often with discontinuous thin melanosomes located in between leucosomes and neosome (Fig. 5.2A). Based on the volume of leucosomes and the field relationships, the original migmatite was a diatexite. The finer-grained neosome is composed of quartz, plagioclase, K-feldspar, biotite, sillimanite, garnet, ilmenite, graphite and apatite. The foliation is generally defined by sillimanite and minor biotite and ilmenite (Fig. 5.2B), but locally it is possible to observe a foliation composed of only biotite. Garnet and K-feldspar porhyroblasts are sometimes mantled by sillimanite in the neosome, and may contain inclusions of biotite, quartz, plagioclase, sillimanite and graphite. Layers of the coarser-grained leucosomes (Figs. 5.2C and D) are sub-parallel to the mylonitic foliation (Fig. 5.2A) and mainly contain quartz, plagioclase, K-feldspar and minor sillimanite, garnet and biotite. A discontinuous foliation, marked by sillimanite and concordant with that in the adjacent neosome, may be present in some leucosomes. Locally, some igneous microstructures are still visible, such as feldspars displaying euhedral shapes with straight boundaries (Fig. 5.2C). More often, crystals in the leucosome have been affected by subsolidus deformation and are rounded or elongated (Fig. 5.2D). The presence of finer-grained trails around some of these crystals (Fig. 5.2D) suggests the occurrence of high strain and dynamic recrystallization in the subsolidus state. This is suggested also by the microstructures of quartz such as undulose extinction, subgrains and irregular grain boundaries.

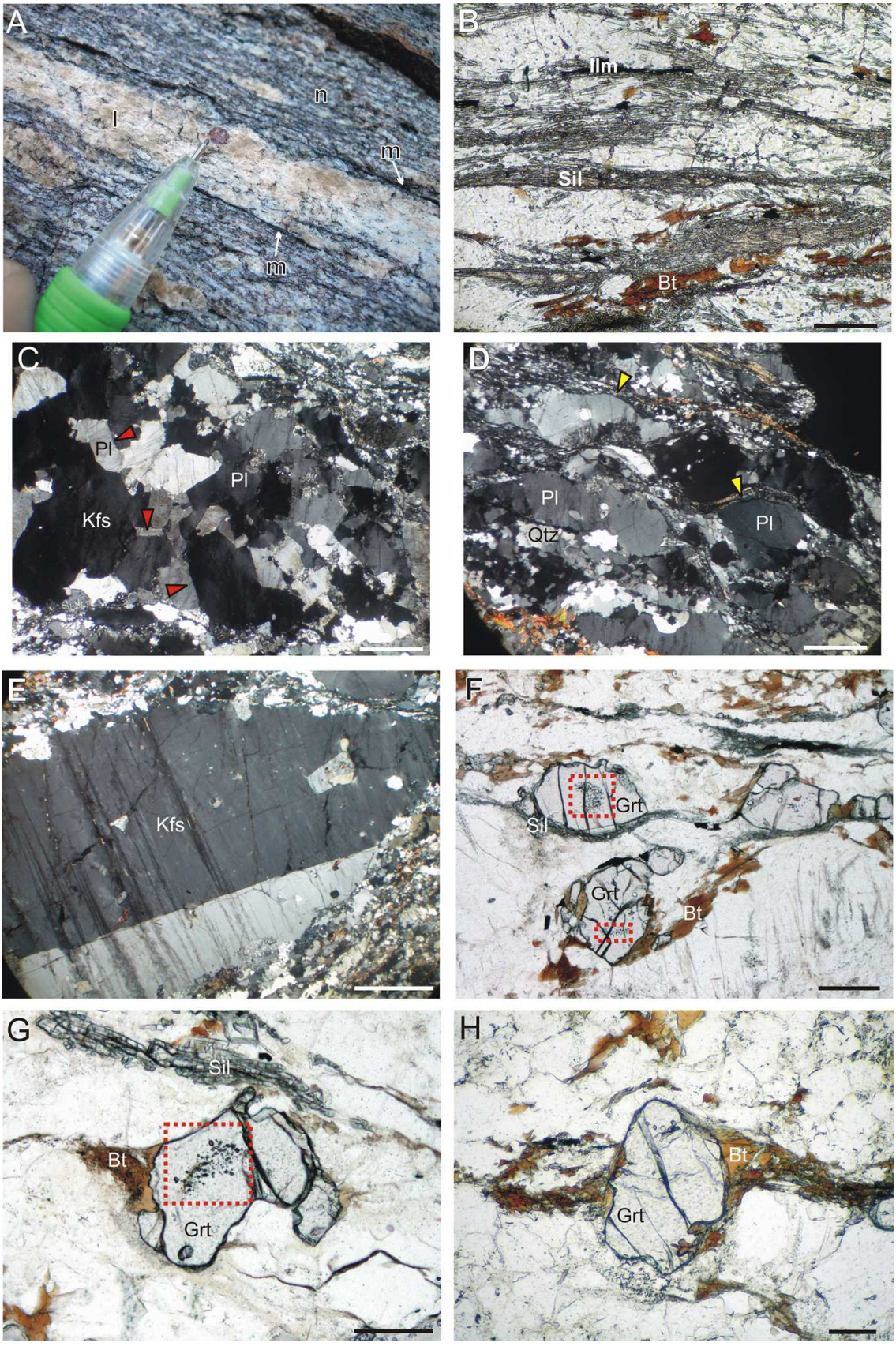
A
l
n
m
m
B
Ilm
Sil
Bt
C
Pl
Pl
Kfs
D
Pl
Qtz
Pl
E
Kfs
F
Grt
Sil
Grt
Bt
G
Sil
Bt
Grt
H
Bt
Grt

Some coarse-grained (up to 2 cm) K-feldspars in the neosome have an augen-like appearance and may show simple twinning and inclusions of euhedral feldspars (Fig. 5.2E), in agreement with the crystallization from a melt. Myrmekites are present along the boundaries of some K-feldspar porphyroblasts. Garnet occurs as subhedral to anhedral crystals (0.1-3 mm in diameter) both in the leucosome (Fig. 5.2A) and in the neosome (Fig. 5.2F). It has a modal amount of ~5-10% and may contain clusters of melt inclusions (Figs. 5.2F and G). Some garnet crystals are partially replaced by biotite or biotite and sillimanite, which often grew in the strain shadows (Figs. 5.2F and G).

Compared with metatexites, the major variations of modal proportions in mylonites regard mainly biotite and garnet, whose contents are inversely correlated, i.e. mylonites are much richer in Grt and poorer in Bt than metatexites. Plagioclase is less abundant in the mylonite neosomes than in metatexite neosomes. Muscovite, very rare in the metatexite, is absent in the mylonite. Sillimanite is fibrolitic in the metatexite and prismatic in the mylonite. The highly deformed rock is also characterized by a greater abundance and greater thickness of leucosomes.

5.2 Mineral chemistry

The composition of muscovite, biotite, garnet, plagioclase and K-feldspar from the metatexite and mylonite has been measured by EMP. The complete dataset is presented in the Supplementary Material (Tabs. S3-S7).

5.2.1 Muscovite

Muscovite from the different microstructural sites of the metatexite (included in K-feldspar porphyroblasts or associated with biotite and sillimanite) does not show systematic differences in composition, which is restricted to a narrow range (Tab. S1).

Figure 5.2 (previous page): Microstructures in the quartzo-feldspathic mylonites. A) Field aspect of the investigated mylonitic migmatite. l: Grt-bearing leucosome. n: neosome. m: melanosome. B) PPL photomicrograph of the neosome, showing fabric-forming sillimanite, biotite and ilmenite. Scalebar: 350 µm. C and D) XPL photomicrographs of two leucosomes; scalebar: 300 µm. In C, feldspars display euhedral shape with planar faces (red arrows), whereas they are deformed and elongated in D (yellow arrows). E) K-feldspar porphyroblast showing simple twinning; XPL. Scalebar: 300 µm. F) Image of garnet crystals in the neosome; red box: cluster of MI; PPL. Scalebar: 200 µm. G and H) Garnet crystals partially replaced by biotite or biotite and sillimanite; PPL. Scalebar: 150 µm. Red box in G: cluster of MI.

Si content ranges between 6.13 and 6.27 apfu (on the basis of 22 oxygens). Muscovite always contains little Na (0.10-0.17 apfu) and Mg (0.06-0.16 apfu). Fe is in the range 0.08-0.21 apfu (0.74-1.84 wt%); F and Cl are below detection limits.

5.2.2 Biotite

Biotites in the metatexites show remarkably constant X_{Mg} values (0.33-0.35; Fig. 5.3), whereas their Ti contents are variable depending on the microstructural location, ranging from 0.24 to 0.32 apfu (based on 22 oxygens) for crystals in contact with garnet, 0.39 to 0.43 apfu for biotite in the leucosome, and 0.42 to 0.49 apfu for crystals in the neosome, either in the matrix or enclosed in K-feldspar porphyroblasts (Tab. S2 and Fig. 5.3). F and Cl contents are low (0.2-0.4 and 0.0-0.1 wt% respectively).

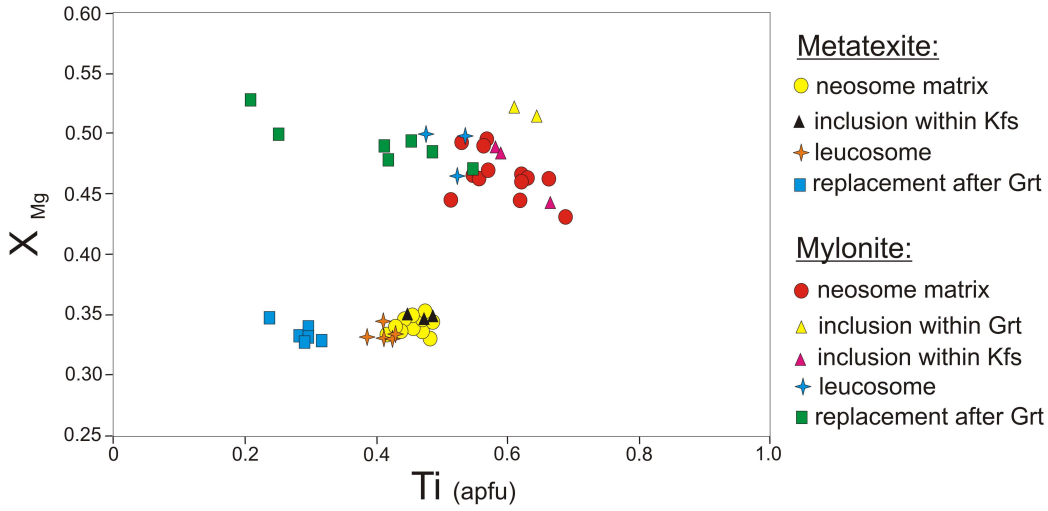

Figure 5.3: X_{Mg} *vs.* Ti diagram for biotite in the investigated metatexite and mylonite.

In the mylonite, biotite composition is more variable, particularly for Ti and X_{Mg} that range from 0.21 to 0.69 apfu and 0.43 to 0.53, respectively (Tab. S3 and Fig. 5.3); these chemical variations display some systematic patterns as a function of the microstructural position (Fig. 5.3). Biotite in contact with garnet has higher X_{Mg} (0.47-0.53) and lower Ti content (0.21-0.55 apfu) than biotite in the neosome (X_{Mg}=0.43-0.50; Ti=0.51-0.69 apfu). In the leucosome, biotite has Ti contents in the range of 0.48-0.53 apfu, whereas biotite included in K-feldspar overlaps the chemical composition of

biotite in the neosome. Biotite enclosed in garnet has the highest Na contents and X_{Mg} values (0.08 apfu and 0.52, respectively). On the other hand, biotite in contact with garnet shows higher F contents (up to 1.5 wt%) than biotite in the neosome (up to 1.0 wt%). Cl is low in all biotites (0.2-0.6 wt%).

TiO_2, F, Cl and X_{Mg} of biotite are lower in the metatexite than in the mylonite. In both rocks there is a systematic variation of TiO_2 content with the microstrucural position of biotite, and there is a negative Ti-X_{Mg} correlation in the metatexite sample (Fig. 5.3). These variations reflect a temperature and reaction control on biotite chemistry (Guidotti *et al.*, 1977; Patiño-Douce *et al.*, 1993): biotites in the neosome and included in garnet grew during the prograde HT metamorphism, but in response to different reactions that imposed them different X_{Mg}; biotite replacing garnet represents retrograde biotite grown at the lowest temperature. The negative Ti-X_{Mg} correlation in biotite from the mylonite (Fig. 5.3) is due to crystal-chemical constraints (Henry *et al.*, 2005). Conversely, the fairly homogeneous X_{Mg} of biotite in the metatexite could be due to retrograde net-transfer reactions (ReNTRs of Kohn and Spear, 2000). Overall, the higher Ti contents of biotite from the mylonites attests for a higher temperature reached by this rock compared to the metatexites, in agreement with other petrographic evidences.

5.2.3 Garnet

Garnet is an almandine-rich solid solution, with small amounts of pyrope, spessartine and grossular components (Tabs S4-S5). Chemical variations between MI-free and MI-bearing domains in the garnet, or between MI-absent and MI-bearing garnets, are absent, both in the metatexites and in the mylonites.

Garnet crystals in the metatexite have a core of composition $Alm_{77-78}Prp_{10-13}Sps_{07-09}Grs_{03-04}$ and are weakly zoned, showing a relatively homogeneous interior domain and an increase in X_{sps} and decrease in X_{alm} and X_{prp} towards the rim (Fig. 5.4). The Ca content is very low and X_{grs} is homogeneous from core to rim. The garnet rim has a composition $Alm_{76-77}Prp_{9-11}Sps_{09-12}Grs_{02-03}$. X_{Mg} slightly decreases from 0.12-0.14 in the core to 0.11-0.12 in the rim. Garnet rims in contact with biotite have X_{Mg}=0.09-0.11.

Garnet cores in the neosomes and leucosomes of the mylonite have a similar composition of $Alm_{72-75}Prp_{20-23}Sps_{02-03}Grs_{02-03}$ with a X_{Mg}=0.21-0.24. Most of the garnets are not zoned, with Fe, Mg, Mn and Ca being fairly homogeneous throughout the crystal (Fig. 5.5A). Garnet rims have a composition of $Alm_{72-73}Prp_{22-24}Sps_{02-03}Grs_{02}$ (X_{Mg}=0.23-0.25) in the leucosome and $Alm_{74-76}Prp_{20-22}Sps_{02}Grs_{02}$ (X_{Mg}=0.21-0.23) in the neosome. Conversely, the garnets in contact with biotite are zoned (Fig. 5.5B): X_{alm} and X_{sps} increase from core to rim, whereas X_{prp} decreases. Thus, garnet rims in contact with biotite display a composition of $Alm_{76-79}Prp_{15-20}Sps_{02-03}Grs_{02}$, with X_{Mg}=0.17-0.20. The Ca content is low and constant.

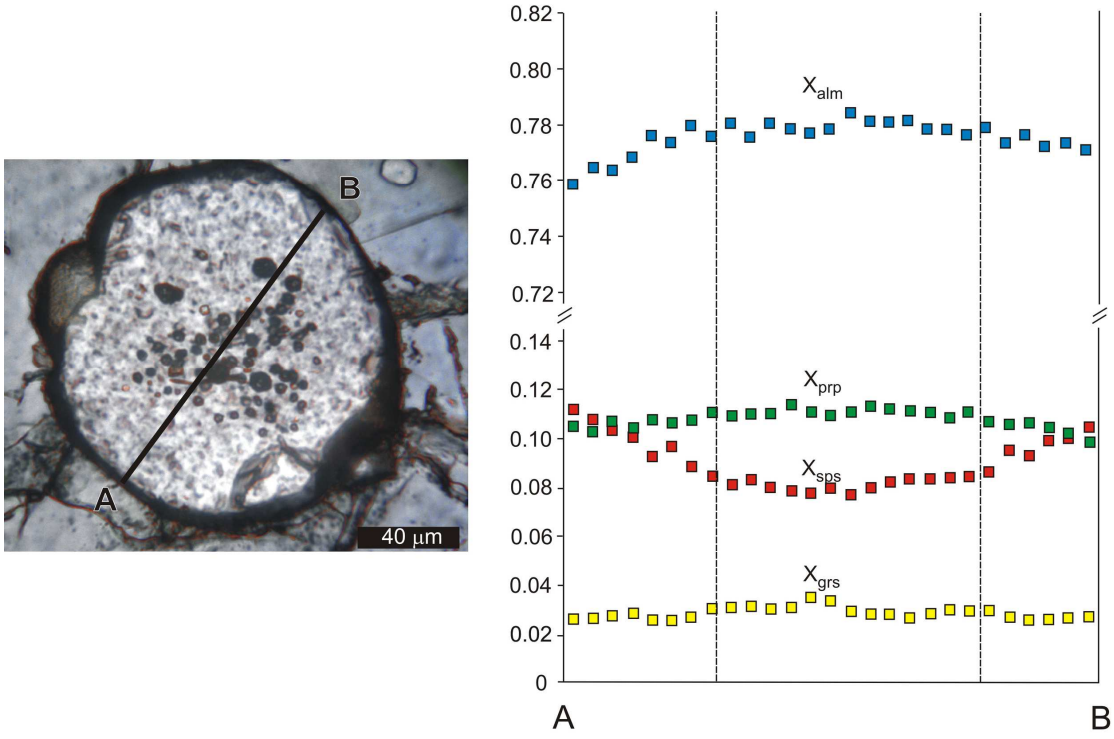

Figure 5.4: Compositional profile of garnet from the metatexite. Black line: trace of the chemical profile. Dashed vertical lines show the location of the boundary between MI-rich core and MI-free rim.

The compositional patterns, flat through most of garnet crystals in the mylonite (Fig. 5.5A), are probably due to the high rates of intracrystalline diffusion associated with the high temperatures during melting (Spear *et al.*, 1999). The zoning patterns characterized by homogeneous cores, increase of X_{sps} and X_{alm} and decrease of X_{Mg} and X_{prp} towards rims are typical of diffusional homogenization at high temperature

followed by garnet dissolution during the retrograde path (Tracy, 1982; Spear *et al.*, 1999; García-Casco *et al.*, 2001). The increase of X_{Mg} in the biotite and of X_{alm} and X_{sps} in the garnet, observed in crystals that are in contact in the mylonite (Fig. 5.5B), indicates the occurrence of garnet dissolution followed by further retrograde exchange reactions. Garnet in the metatexites does not show the bell-shaped Mn zoning pattern that often characterizes the prograde growth; instead, Mn increases from core to rim (Fig. 5.4). However, the euhedral shape along with a decrease of X_{alm} towards the rim (Fig. 5.4) is not consistent with dissolution of the garnet crystal (see above). These observations may rather suggest the involvement of a Mn-bearing phase (ilmenite ?) as reactant in the garnet-producing reaction.

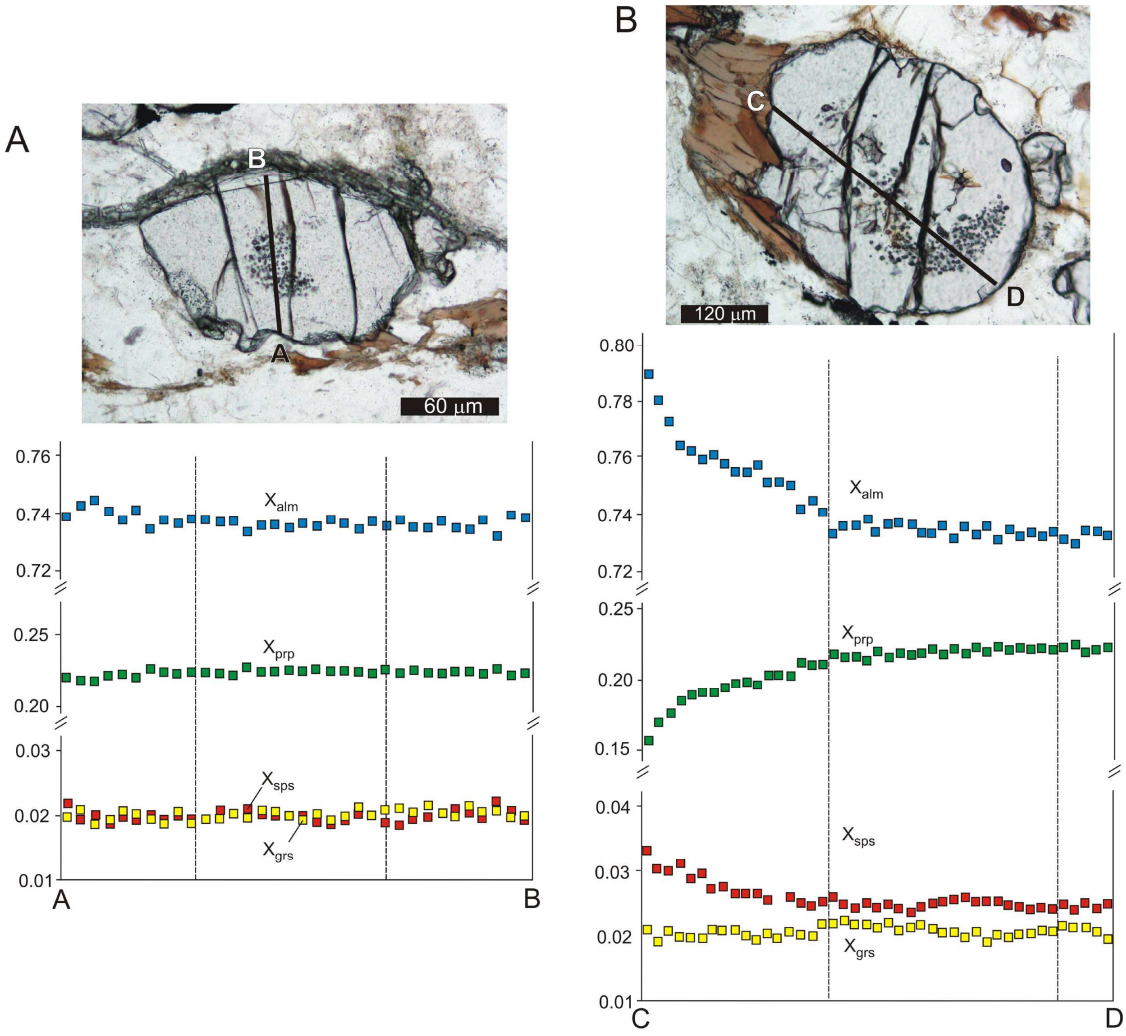

Figure 5.5: A) and B) Compositional profiles of garnets from the mylonite. Black lines: traces of the chemical profiles. Dashed vertical lines show the location of the boundary between MI-rich core and MI-free rim.

5.2.4 Feldspars

Only feldspars without visible exsolutions have been selected for EMP analyses (Tabs. S6-S7). Plagioclase composition varies according to the microstructural position in the studied rocks. The most anorthitic plagioclase (with compositions of $Ab_{66-69}An_{29-33}Or_{1-2}$ in metatexites and $Ab_{66-73}An_{25-32}Or_{1-2}$ in mylonites) forms the matrix of the neosome, whereas crystals slightly more albitic and richer in Or are present in the leucosome ($Ab_{72-77}An_{21-25}Or_{1-3}$ in metatexites and $Ab_{70-76}An_{21-26}Or_{3-5}$ in mylonites). The latter probably represent the plagioclase component crystallized from the anatectic melt (Sawyer, 2001; Hasalová *et al.*, 2008). Plagioclase grains included in the K-feldspar porphyroblasts display compositions ($Ab_{67-69}An_{29-32}Or_{1-2}$ in metatexites and $Ab_{67-72}An_{27-31}Or_2$ in mylonites) that overlap those of plagioclase in the neosome. No compositional differences have been observed between K-feldspar porphyroblasts of the neosome ($Or_{78-82}Ab_{17-22}An_{0-1}$ in metatexites and $Or_{74-83}Ab_{17-26}An_{0-1}$ in mylonites) and crystals in the leucosome ($Or_{78-82}Ab_{18-22}An_{<1}$ and $Or_{75-82}Ab_{18-25}An_{0-1}$, respectively).

5.3 Geochemistry

The whole rock chemical data are presented in Tab. S8 of the Supplementary Material. The bulk analyses of metatexites show granitic compositions, with SiO_2~71 wt%, Al_2O_3~14 wt%, Fe_2O_3 ~3 wt%, MgO<1 wt%, CaO~1 wt%, Na_2O~2 wt% and K_2O~5 wt%; #Mg varies from 0.49 to 0.52, and the ASI from 1.23 to 1.31. Given the heterogeneous nature of the mylonitic migmatite, it is more difficult to obtain representative bulk analyses of this rock. Nevertheless, it also seems to have a granitic composition, comparable to (although slightly richer in SiO_2 and lower in $Fe_2O_{3(tot)}$+MgO that) the metatexites. Given that the several components of metatexites and mylonites (leucosomes and neosomes) have been mechanically separated and analyzed for the bulk composition, I have plotted these data on a series of major element variation diagrams (Fig. 5.6), in order to investigate the chemical differentiation during melting. The existing melanosomes are only a few mm thick and I was not able to separate them. Only in the case of the (Na_2O+CaO) *vs.* SiO_2 diagram, the neosomes are very close to the whole migmatites (Fig. 5.6C). The rest of diagrams, however, shows

clear and systematic differences between neosomes, leucosomes and the whole rock in the two types of migmatites. (Figs. 5.6A, B and D). Leusomes are slightly richer in SiO_2, clearly richer in K_2O and lower in $Fe_2O_{3(tot)}$+MgO compared to the bulk-rock composition, whereas neosomes show opposite trends. This indicates that the neosomes have lost melt to the leucosomes.

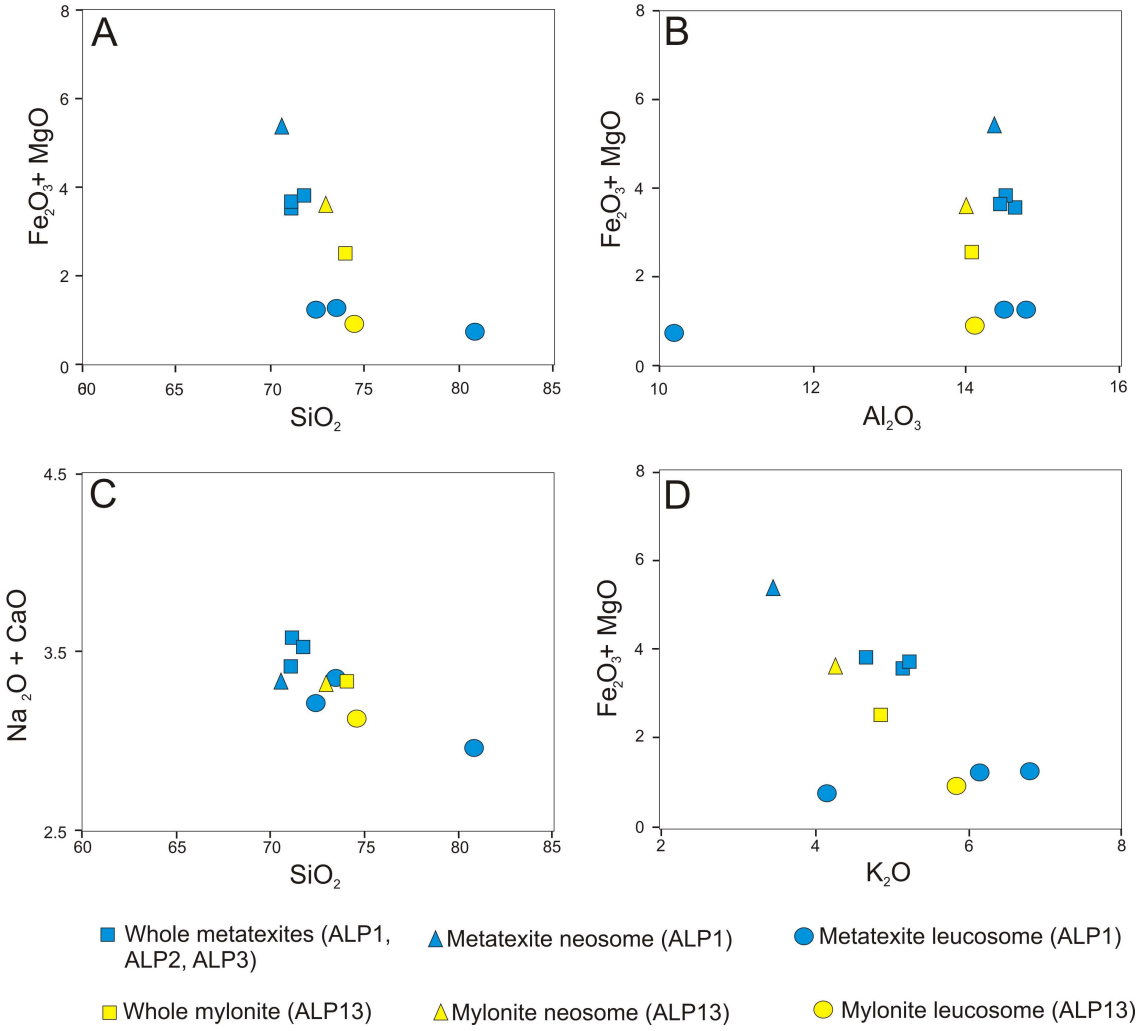

Figure 5.6: Bivariant diagrams showing the compositional variations in the studied migmatites. A) Fe_2O_3+MgO *vs.* SiO_2. B) Fe_2O_3+MgO *vs.* Al_2O_3. C) Na_2O+CaO *vs.* SiO_2. D) Fe_2O_3+MgO *vs.* K_2O.

The leucosomes are peraluminous leucogranitic rocks, with $Na_2O/K_2O<0.5$, and ASI and #Mg in the range of 1.07-1.22 and 0.50-0.54. They are enriched in SiO_2, K_2O, Sr, Ba and Pb and depleted in MgO, Fe_2O_3, TiO_2, CaO, V, Cr, Ni, Y, Zr, Nb and the LREE relative to whole migmatite compositions. Comparing the leucosomes in both types of

rocks, Sr, Zr, Ba and Ce concentrations are higher in metatexites than in mylonites, whereas La and Pb contents are higher in leucosome of the mylonitic migmatites. Among the leucosomes analyzed in metatexites, there is an outlier departing from collinearity with leucosome and bulk rock, showing extremely high concentrations in SiO_2 and low concentrations in K_2O and Al_2O_3 (Fig. 5.6); this leucosome does not seem to represent a primary anatectic melt. Neosomes are enriched in Fe_2O_3, MgO, TiO_2, P_2O_5, V, Cr, Y, Zr and LREE, and depleted in SiO_2, K_2O, Na_2O, Sr, Ba and Pb relative to whole migmatite compositions, in accordance with the lost of a granitic melt to the leucosomes.

5.4 Thermobarometry

The conventional thermobarometric approach has been applied to constrain the melting conditions in the studied migmatites. Temperatures were calculated using the Grt-Bt exchange thermometer (calibrations of Ferry and Spear, 1978 and Perchuk & Lavrent'eva, 1983; hereafter referred as FS78 and PL83). Pressure estimates were determined using the GASP barometer (calibrations of Koziol and Newton 1988 and Koziol, 1989; hereafter KN88 and K89 respectively). In addition, temperature has been evaluated also using the Ti-in-biotite empirical thermometer of Henry *et al.*, (2005).

Considering the MI-bearing garnet cores and biotites in the matrix of the neosome in both types of migmatites, the garnet-biotite thermometry yields temperatures of 670-700 °C (PL83) and 720-775 °C (FS78) for metatexite (at 4 kbar), and 660-760 °C (PL83) and 725-970 °C (FS78) for mylonites (at 6 kbar). The results for mylonites indicating T >> 900 °C are clearly inconsistent with the phase assemblage and with the temperatures obtained by the Ti-in-biotite thermometer (see below). The scattered Grt-Bt temperatures in the mylonite likely indicate that garnet and biotite in the neosome of this rock are not in equilibrium. However, using the biotite crystals included in the garnet, the calibration of Ferry and Spear (1978) yields reasonable peak temperatures of 760-780 °C for the mylonite. These results are in broad agreement with both Ti-in-biotite thermometry (see below) and literature data about the metamorphic peak conditions of quartzo-feldspathic mylonites outcropping at the contact with the

peridotite (T~800 °C; Tubia *et al.*, 1997). On the other hand, the temperature estimates obtained from the Grt-Bt thermometer in metatexites may not represent peak-T conditions, because X_{Mg} of biotite was likely affected by retrograde net-transfer reactions. Using garnet rims and retrograde biotite in mutual contact, the Grt-Bt thermometer gives temperatures of 640-690 °C (PL83) and 615-710 °C (FS78) for the metatexite and 640-700 °C (PL83) and 660-780 °C (FS78) for the mylonite. Application of the Ti-in-biotite thermometer indicates temperature close to 700 °C for the prograde biotites in the metatexites, and temperatures in excess of 750 °C for most of the prograde biotites in mylonites (Fig. 5.7). The Ti content of the retrograde biotite replacing garnet indicates T≤650 °C in metatexites and T≤750 °C in mylonites.

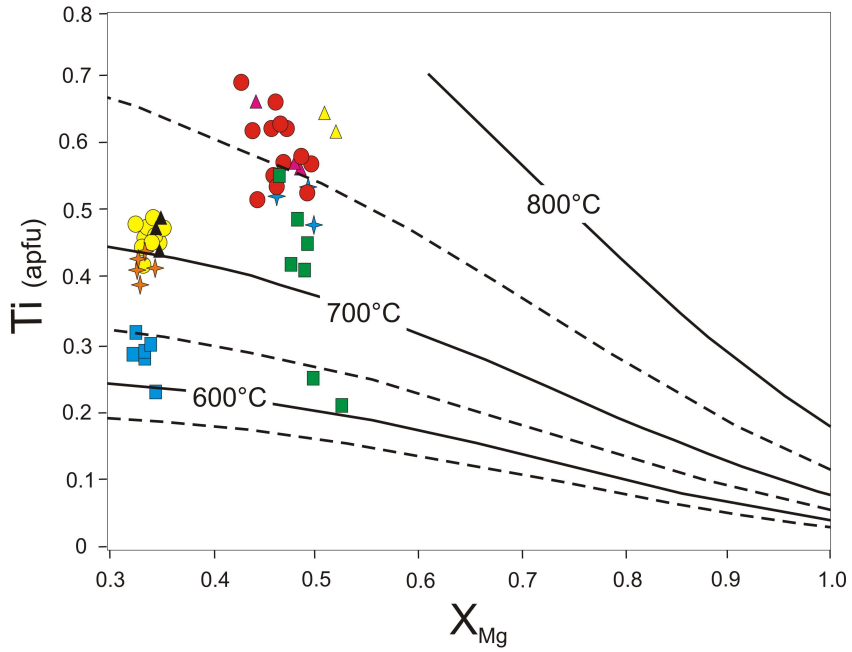

Figure 5.7: Ti *vs.* X_{Mg} diagram for the biotite, with the isotherms from Henry *et al.* (2005). Symbols as in Fig. 5.3.

The GASP geobarometer yields pressures of 4.1-5.8 kbar (K89) and 3.7-5.9 kbar (KN88) for metatexites (at 700 °C), and 5.0-7.6 kbar (K89) and 4.2-6.6 kbar (KN88) for mylonites (at 800 °C), using the core compositions of minerals located in the matrix of the neosomes. However, it should be taken into account that pressure estimates for the mylonite may be (significantly ?) affected by disequilibrium among minerals (see above) and by diffusional homogenization of the garnet zoning at high temperature.

Most of the pressure estimates for mylonites are inconsistent with the literature data that indicate a P=8.3±0.7 kbar (Tubia *et al.*, 1997) for the metamorphic peak in these rocks. However, in their calculations, Tubia and coworkers considered the presence of rutile, whereas its absence in the studied migmatites (ALP1 and ALP13) would indicate melting at pressures lower than 8 kbar. On the other contrary, the pelitic kinzigites outcropping just 20 m above the studied Qtz-feldspathic mylonites contain rutile inside MI (see Chapter 7).

Overall, the thermobarometric data indicate a decrease in temperature (Fig. 5.7) and pressure from the quartzo-feldspathic mylonites to the metatexites.

5.5 Pseudosection on the quartzo-feldspathic metatexite

The phase equilibria in migmatites are sensitive to the bulk composition (White *et al.*, 2001). Since the mineral phases in the metatexite are likely to constitute an equilibrium assemblage (see above), a P-T pseudosection (Powell and Holland, 2010) was constructed using the measured bulk composition of the metatexite ALP1 (Fig. 5.8) to obtain a better understanding of the melting conditions and reactions in this rock. Some important aspects must be taken in account in the thermodynamic modelling of anatectic rocks: 1) the bulk composition effectively in equilibrium (equilibration volume); 2) the choice of a model system; 3) possible chemical fractionation of the bulk rock composition due to zoned porphyroblasts; 4) melt loss during the prograde evolution. A bulk-rock composition obtained by XRF (composition ALP1 in Tab. S8) was chosen as representative of the equilibration volume. The chosen chemical system is MnO-Na_2O-CaO-K_2O-FeO-MgO-Al_2O_3-SiO_2-H_2O-TiO_2 (MnNCKFMASHT). Calculation was performed using the H_2O content derived from the LOI value. The bulk-rock composition used (in mol%) is indicated in the upper left inset of the calculated P-T pseudosections. Because garnet porphyroblasts are rare and small, the chemical fractionation owing to garnet growth is considered negligible. Field (lack of leucosome networks) and petrographic observations (biotite + sillimanite replacing garnet), along with chemical data (lack of depleted bulk-rock compositions), suggest minimal or no melt extraction and loss from the metatexites (Spear *et al.*, 1999; Sawyer,

2008; Brown, 2002) and, thus, no re-integration of melt into the rock composition is needed.

The pseudosection was calculated following the approach of Connolly (1990, revised 2009) based on the minimization of the Gibbs energy, using the thermodynamic software set Perple_X and the internally consistent thermodynamic data set of Holland and Powell (1998, as revised in 2003). The effect of Fe^{3+} was neglected, because, although potentially important, no magnetite was present in the studied samples and thus the amount of Fe^{3+} in biotite and garnet was assumed to be insignificant. Along with a melt phase, the minerals considered in the calculation are garnet, biotite, ilmenite, sillimanite, cordierite, muscovite, quartz, plagioclase and K-feldspar. The melt solution model was taken from White *et al.,* (2007), cordierite from Powell & Holland (1999), garnet from Holland & Powell (2001), white mica from Coggon & Holland (2002), plagioclase from Newton *et al.,* (1980), K-feldspar from Thompson & Hovis (1979) and biotite from Tajčmanová *et al.,* (2009). The Mn solution in garnet was accounted for by the Mn end-member introduced by Tinkham *et al.,* (2001). The minor Mn solution observed in the natural biotite was neglected. An ideal model was used to account for the solution of Mn in ilmenite. The fluid was considered as pure H_2O (a_{H_2O} =1). Although the presence of graphite suggests that the fluid phase was a COH fluid, probably buffered to a high activity of H_2O (see below), to date it is not possible to consider values of the a_{H_2O} different from 1 during the calculation of pseudosections (i.e., there are still problems that affect the pseudosection modelling).

Figure 5.8A shows the pseudosection constructed with the measured bulk composition for the P-T range 2-8 kbar and 600-900 °C. The assemblage garnet+biotite+plagioclase+K-feldspar+sillimanite+quartz+liquid, inferred to be stable during the anatexis of the rock, is modelled by a fairly large large penta-variant field at 670<T<800 °C and 3<P<8 kbar. This field is bordered at low T by the muscovite-out curve and the H_2O-saturated solidus.

Figure 5.8 (next page): P-T pseudosections for the metatexite ALP1 calculated in the MnNCKFMASHT system. Light, medium, dark and very dark grey fields are tri-, quadri-, penta and esa-variant fields respectively. The red dashed area represents the P-T interval inferred for the melting. A) Isopleths of garnet and biotite are reported. Yellow, pink and blue lines refer to the melt-in (solidus), muscovite-out and biotite-out curves, respectively. B) Isomodes for garnet and melt are reported.

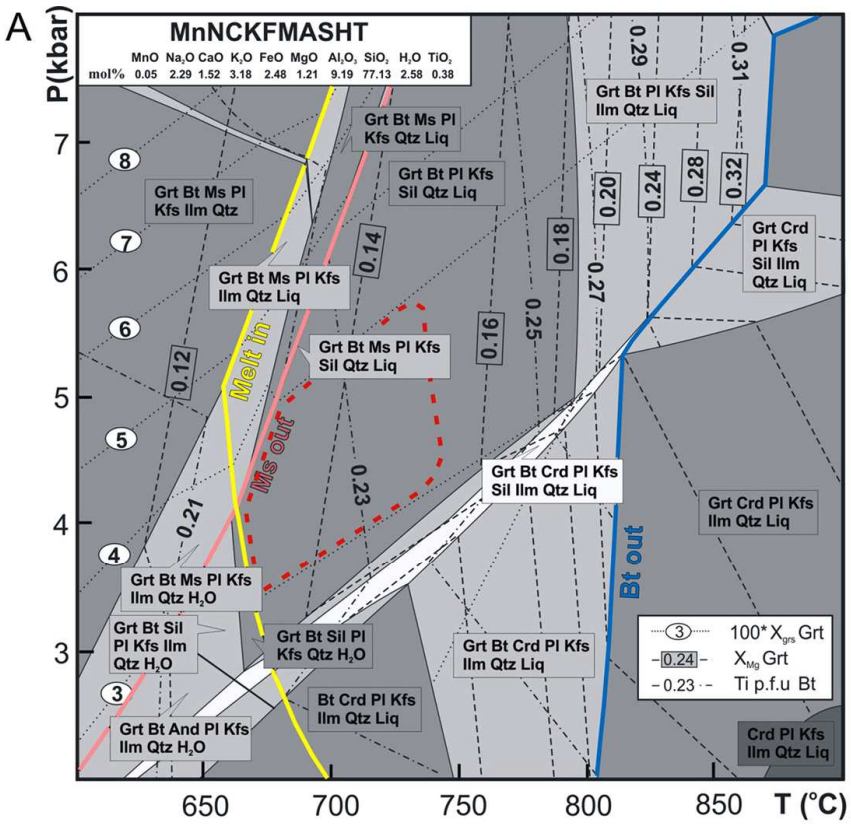
A
MnNCKFMASHT
MnO Na2O CaO K2O FeO MgO Al2O3 SiO2 H2O TiO2
mol% 0.05 2.29 1.52 3.18 2.48 1.21 9.19 77.13 2.58 0.38
P(kbar)
T (°C)
Grt Bt Ms Pl Kfs Ilm Qtz
Grt Bt Ms Pl Kfs Qtz Liq
Grt Bt Pl Kfs Sil Qtz Liq
Grt Bt Pl Kfs Sil Ilm Qtz Liq
Grt Crd Pl Kfs Sil Ilm Qtz Liq
Grt Bt Ms Pl Kfs Ilm Qtz Liq
Grt Bt Ms Pl Kfs Sil Qtz Liq
Grt Bt Crd Pl Kfs Sil Ilm Qtz Liq
Grt Crd Pl Kfs Ilm Qtz Liq
Grt Bt Ms Pl Kfs Ilm Qtz H2O
Grt Bt Sil Pl Kfs Ilm Qtz H2O
Grt Bt Sil Pl Kfs Qtz H2O
Grt Bt Crd Pl Kfs Ilm Qtz Liq
Bt Crd Pl Kfs Ilm Qtz Liq
Grt Bt And Pl Kfs Ilm Qtz H2O
Crd Pl Kfs Ilm Qtz Liq
Melt in
Ms out
Bt out
100*Xgrs Grt
XMg Grt
Ti p.f.u Bt

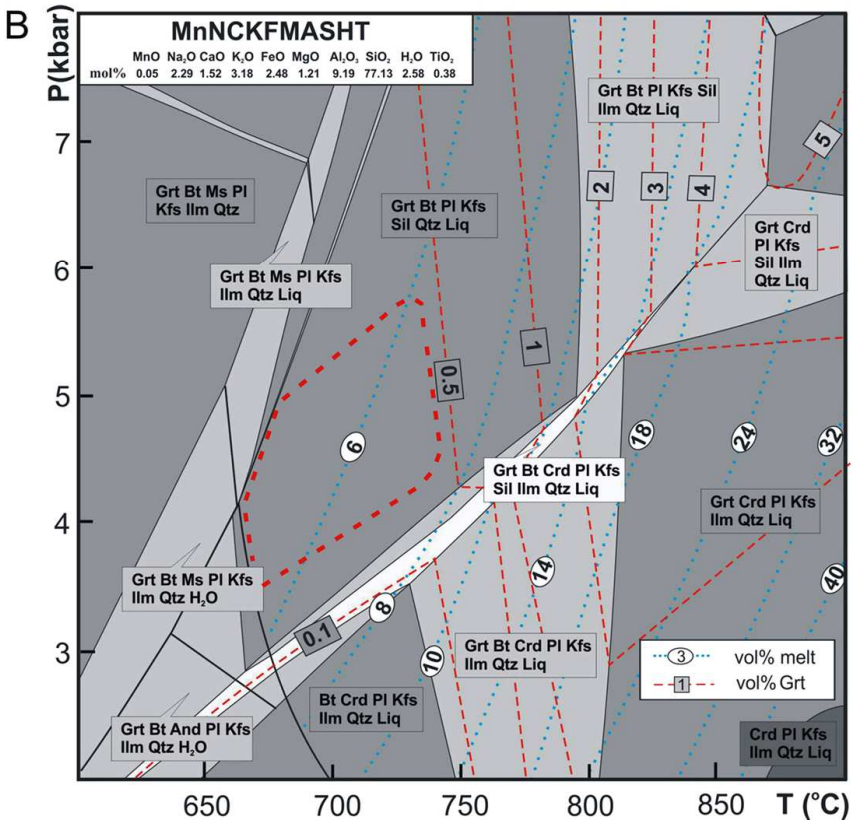
B
MnNCKFMASHT
MnO Na2O CaO K2O FeO MgO Al2O3 SiO2 H2O TiO2
mol% 0.05 2.29 1.52 3.18 2.48 1.21 9.19 77.13 2.58 0.38
P(kbar)
T (°C)
Grt Bt Ms Pl Kfs Ilm Qtz
Grt Bt Pl Kfs Sil Qtz Liq
Grt Bt Pl Kfs Sil Ilm Qtz Liq
Grt Crd Pl Kfs Sil Ilm Qtz Liq
Grt Bt Ms Pl Kfs Ilm Qtz Liq
Grt Bt Crd Pl Kfs Sil Ilm Qtz Liq
Grt Crd Pl Kfs Ilm Qtz Liq
Grt Bt Ms Pl Kfs Ilm Qtz H2O
Grt Bt Crd Pl Kfs Ilm Qtz Liq
Bt Crd Pl Kfs Ilm Qtz Liq
Grt Bt And Pl Kfs Ilm Qtz H2O
Crd Pl Kfs Ilm Qtz Liq
vol% melt
vol% Grt

Further constraints on the P-T conditions during melting may be obtained from compositional isopleths of the MI-bearing garnet core (X_{grs}=0.3-0.4 and X_{Mg}=0.12-0.14) and prograde biotite in the neosome (Ti=0.21-0.24 apfu/11 oxygens). Biotite X_{Mg} is not considered as a valid constraint in the modelling because it was the most likely mineral that may have been affected by retrograde net-transfer reactions. The corresponding isopleths modelled in the pseudosection constrain the conditions of equilibration in the studied metatexite at 670<T<750 °C and 3.5<P<5.5 kbar (Fig. 5.8A). As (i) the garnet in the metatexite shows a weak zoning pattern (Fig. 5.4) that is likely to represent a prograde compositional zoning (see above), (ii) considering even a slight re-homogenization at high temperatures, Ca diffusion in garnet is slower than most other major cations (Spear *et al.*, 1999; Vielzeuf *et al.*, 2007), and (iii) Ti content of biotite is not affected by retrograde net-transfer reactions (Kohn and Spear, 2000), I conclude that the inferred conditions of equilibration (especially in terms of temperature) can be interpreted as melting conditions. These P-T estimates are consistent with the data obtained by thermobarometry. The amounts of melt and garnet in this field (Fig. 5.8B) reach maximum values of 7 vol% and 0.5 vol%, respectively, in agreement with the field and petrographic observations. Calculated garnet mode indicates that after the beginning of melting, the amount of garnet slightly increases in the PT region of interest (Fig. 5.9), explaining the possibility for this peritectic garnet to entrap melt inclusions.

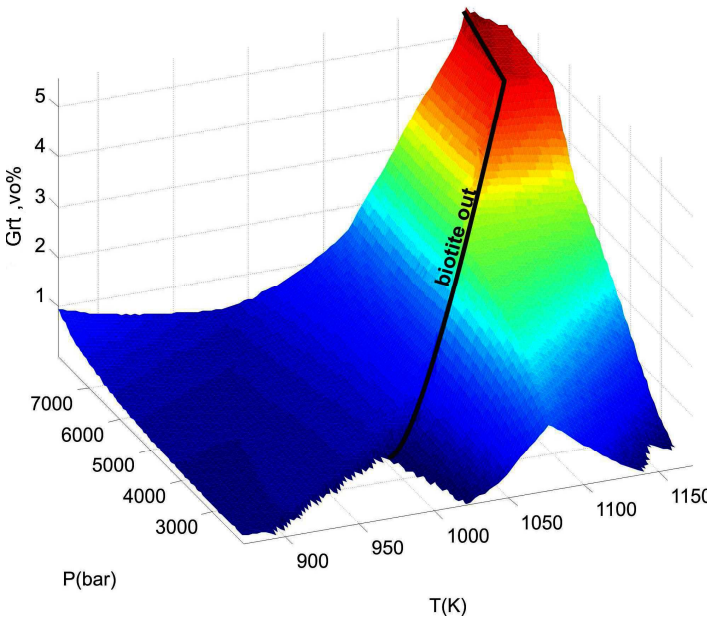

Figure 5.9: Change of the garnet mode (vol%) as a function of pressure (P) and temperature (T).

At P>4 kbar, ilmenite disappears between the melt-in and muscovite-out curves, whereas at lower pressure it is completely consumed just (~5 °C) before the H_2O-saturated solidus (Fig. 5.8A). Therefore, ilmenite might have participated as reactant in the garnet-forming reaction at low temperature (T≤700 °C).

Graphite reduces the a_{H_2O} in the fluid, displacing fluid-present melting equilibria to higher T, and fluid-absent melting reactions to lower T (e.g. Clemens, 1990). It is possible to quantify the minimum shift of the H_2O-saturated solidus to higher temperatures (Cesare *et al.*, 2003) by intersecting the isopleths of the maximum H_2O content of graphite-saturated COH fluids (Connolly and Cesare, 1993) and those of X_{H_2O} values of fluids coexisting with haplogranitic melts (e.g., Ebadi and Johannes, 1991). The fluid-present solidus shift is ~35°C at 2 kbar, ~20°C at 4 kbar, ~10°C at 5 kbar and is negligible for P>6 kbar (Fig. 5.10).

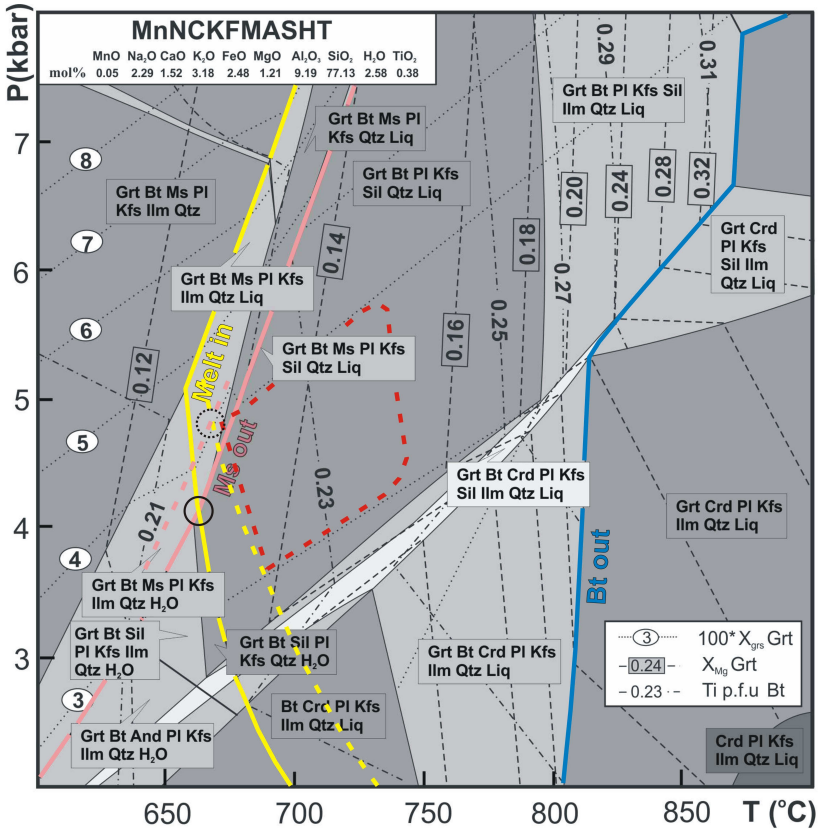

Figure 5.10: P-T pseudosection of Fig. 5.8A, modified to show the fluid-saturated solidus and muscovite-out curves (yellow and pink dashed curves respectively) coexisting with graphite. Black circles: intersection between the solidus and muscovite-out curves. The red dashed area represents the P-T interval inferred for melting.

The maximum a_{H_2O} of fluids internally generated in the studied rock is buffered by graphite to values >0.8 at the inferred P-T conditions (Connolly and Cesare 1993), resulting in a lowering by ~10-15 °C of the positions of the subsolidus dehydration reactions (e.g., Pattison and Tinkham, 2009). This shift for the muscovite-out curve at melting temperatures is reported in Fig. 5.10. Hence, considering the presence of graphite in the rock, the intersection of the fluid-saturated solidus and the muscovite-out curves (black circle in Fig. 5.10) moves towards higher P (>4.5 kbar).

5.6 Mechanisms of anatexis in metatexites and mylonitic migmatites

The microstructural criteria for the recognition of the former presence of melt have been recently reviewed by Vernon (2011). In the studied migmatites, the most convincing microstructures of the evidence of melting are: i) plagioclase and quartz films around quartz or garnet grains (Figs. 5.1J-L); ii) cuspate-shaped feldspars, surrounded by corroded grains (Fig. 5.1I); and iii) euhedral faces of some feldspars in leucosomes (Fig. 5.1D and Fig. 5.2C). The first two microstructures are thought to represent previous melt films and pools (pseudomorphs of melt-filled pores; Holness and Sawyer, 2008), whereas the latter testifies that crystal grew in contact with a melt (Marchildon and Brown, 2002). Melt pseudomorphs were not found in the mylonite, owing to the intense deformation that continued in the subsolidus state. However, it is important to realize that the occurrence of melt inclusions (see Chapter 6) represents another reliable microstructural criterion for the former presence of anatectic melt in the studied rocks (Cesare *et al.*, 2011).

Field, microstructural and chemical observations indicate that the quartzo-feldspathic metatexites were not affected by melt loss or infiltration, and thus their composition can be considered representative of the protolith. Their compositions overlap those of typical metagreywackes (see Vielzeuf and Montel, 1994; Gardien *et al.*, 1995; Corona-Chávez *et al.*, 2006). Conversely, the mylonite shows slightly higher SiO_2 and lower Al_2O_3, Fe_2O_3, MgO, TiO_2 and CaO concentrations than metatexites. These differences could be due to: i) slightly different metasedimentary protoliths; or ii) difficulties associated with the bulk analyses of heterogeneous rocks such as

migmatites. The occurrence of a highly heterogeneous metasedimentary crust in the Alpujarride Complex (made by phyllites, mica schists, psammitic schists, quartzite and greywacke; Platt *et al.,* 2003) may support the first hypothesis. In any case, the bulk compositions of both rocks are very close, and I can reasonably assume that they represent the same protolith affected by variable degree of melting and deformation. Despite the higher melting degree and the high strain deformation that characterizes the quartzo-feldspathic mylonites, the melt segregation was minimal, probably owing to the high ductility of the mylonitic zone that hampered the development of fractures (Tubia *et al.*, 1997).

Most of the changes in phase composition and modal contents from the metatexite to the mylonite are consistent with the described increase of temperature and melting degree, even if these rocks do not derive exactly from the same protolith. Ti and X_{Mg} in biotite increase from the metatexite to the mylonite, in agreement with the increase in temperature (Guidotti *et al.,* 1977; Patiño-Douce and Johnston, 1991; Johnson *et al.,* 2001). On the other hand, X_{grs} of the peritectic garnet should increase with increasing pressure (Montel and Vielzeuf, 1997) and, therefore, from the metatexite to the mylonite. However, this variation in the garnet chemistry has not been observed in the studied rocks (the mylonitic garnet has X_{grs} equal to, or slightly lower than, the garnet in the metatexite).

The mechanisms of melting of crustal rocks have been widely investigated by experimental petrology (recently reviewed in White *et al.*, 2011). Many of these experimental studies have been performed to constrain the melting reactions that metapelites and metagreywackes may cross upon heating at medium pressures (Petö 1976; Vielzeuf and Holloway, 1988; Patiño-Douce and Johnston 1991; Vielzeuf and Montel, 1994; Patiño-Douce and Beard 1995; Stevens *et al.*, 1997; Patiño-Douce and Harris 1998). These model **discontinuous** melting reactions, in order of increasing T at 5-8 kbar, are the following:

the fluid-saturated solidus:

$$Ms + Bt + Pl + Qtz + Kfs + fl \rightarrow melt \qquad (1)$$

the fluid-saturated melting of muscovite:

$$Ms + Bt + Pl + Qtz + fl \rightarrow Als + melt \quad (2)$$

the fluid-absent melting of muscovite:

$$Ms + Pl + Qtz \rightarrow Bt + Kfs + Als + melt \quad (3)$$

the fluid-absent melting of biotite:

$$Bt + Pl + Als + Qtz \rightarrow Grt/Crd + Kfs + melt \quad (4)$$

or

$$Bt + Pl + Qtz \rightarrow Opx + Grt + Kfs + melt \quad (5)$$

Reactions (1) and (2) require an H_2O-rich fluid phase initially present in the protolith and in general produce small amounts of H_2O-saturated melt (Vielzeuf and Holloway, 1988), unless "water-fluxed" melting occurs (Sawyer, 2010). In addition, the eutectic reaction (1) can only occur when K-feldspar is present at the solidus. Peritectic orthopyroxene is produced by reaction (5) in Al_2SiO_5-free rocks (Vielzeuf and Montel, 1994; Patiño-Douce and Beard 1995).

The petrogenetic grids and liquidus diagrams (e.g., Vielzeuf and Holloway, 1988; Spear and Kohn, 1996; Spear *et al.,* 1999; Vielzeuf and Schmidt, 2001) allow to consider also the **continuous** nature of the melting reactions. Thus, once muscovite is completely consumed by reaction (3), at $P \geq 4\text{-}4.5$ kbar and in peraluminous metasedimentary rocks, melting proceeds through the continuous fluid-absent melting reaction

$$Bt + Pl + Als + Qtz \rightarrow Grt + Kfs + melt \quad (6)$$

resulting in garnet growth together with melt production right after the complete breakdown of muscovite (reaction 3). The continuous fluid-absent melting reaction (6) proceeds until the discontinuous reaction (4) is reached. Conversely, and if I consider the previous discussion on the intersection of the fluid-saturated solidus and the muscovite-out reaction in graphite-bearing metasedimentary rocks, at $P \leq 4\text{-}4.5$ kbar the

rock dehydrates before melting, first by the muscovite dehydration reaction and then by continuous biotite dehydration. Melting starts at the fluid-saturated solidus (1) and evolves by the continuous fluid-absent melting reaction (6) until the discontinuous reaction (4). However, the direct experimental confirmation of the continuous reaction (6) at low temperature has not been possible owing to sluggish kinetics at T<750°C (Spear and Kohn, 1996).

The petrographic features of the metatexite (e.g., abundant Bt and Fib, the occurrence of very rare Ms with resorbed shape and often armoured by K-feldspar, MI in peritectic garnet) along with the inferred melting conditions (T=670-750 °C and P=3.5-5.5 kbar) and the topology of the pseudosection (Fig. 5.10) indicate two feasible scenarios about melt-producing reactions in the metatexite: a) melting occurs first by the discontinuous reaction (3) closely followed by the continuous reaction (6); or b) the first melting reaction encountered by the rock is the fluid-saturated solidus (1) closely followed by reaction (6). Biotite is involved as reactant in melting reactions at 700-750 °C and might be expected to exhibit textures of resorption. However, it is well known that at these near-solidus conditions minerals, and particularly biotite, may recrystallize as euhedral crystals (see Icenhower and London 1995; Stevens *et al.*, 1997). Therefore, the occurrence of biotite crystals with well-defined boundaries in contact with melt pseudomorphs (Fig. 5.1L) is not inconsistent with the involvement of biotite as a reactant during melting.

Experimental evidence indicates that the discontinuous Bt fluid-absent melting reaction (4) should be reached at T≥800-850 °C, for P=6-10 kbar (Vielzeuf and Holloway, 1988; Patiño-Douce and Johnston 1991; Gardien *et al.*, 1995). The observed mineral assemblage in the mylonitic migmatite (e.g., absence of muscovite, presence of Ti-rich prograde biotite, abundant sillimanite and MI in peritectic garnet) and the calculated melting temperature in excess of 750 °C (Fig. 5.7), all indicate that the continuous Bt melting reaction (6) was involved in the generation of melt in the mylonite, and that the terminal reaction (4) was not exceeded.

The inferred melting reactions produced leucosomes with peraluminous leucogranitic compositions in both metatexite and mylonite. During cooling, H_2O that exsolved from the crystallizing melts might have infiltrated the adjacent neosomes or be

consumed by back reactions (Kriegsman 2001; White and Powell, 2010), producing leucosomes with anhydrous or near-anhydrous chemical composition (Tab. S8). Hence, the composition of leucosomes can hardly provide any meaningful information about the fluid regime during the prograde melting. The occurrence of the melt-producing reactions (3, 4 and 6) in the studied migmatites would imply a H_2O-undersaturated environment during melting. Conversely, the occurrence of reaction (1) would imply that the onset of melting took place under fluid-saturated conditions for the metatexite. Nevertheless, the presence of graphite in the metatexite indicates that such fluid cannot have been pure H_2O, and that its mole fraction must have been >0.8 (Connolly and Cesare, 1993). The detailed study of the described MI in Grt will provide further clues on the nature of melting reactions and fluid regimes during the anatexis of these rocks.

Chapter 6
Melt inclusions in quartzo-feldspathic metatexites and mylonitic migmatites

6.1 Microstructural characterization

This research is primarily focused on the characterization of MI in two different types of migmatite from the same anatectic basement: Qtz-feldspathic metatexites located towards the base of the Ojen unit, and Qtz-feldspathic mylonites found near the top of the Ojen unit. These two rocks are chosen because they represent migmatites with different melting conditions. The size of MI in these rocks represents an analytical challenge as it is near the limits of spatial resolution of the conventional microanalytical techniques. Hence, the characterization of MI microstructures was performed by using optical microscope along with the new generation of FEG-based electron microscopes (see Chapter 3).

6.1.1 Occurrence and optical features

MI have been recognized within garnet in both types of migmatites. MI-bearing garnets have different microstructures according to the type of migmatite (see Chapter 5). In mylonitic migmatites, MI-bearing garnets are less abundant (~20% of the garnet population) than in metatexites (~90%). In general, MI are clustered, forming groups of tens of inclusions which are often characterized by a similar size. Clusters, locally displaying a spherical geometry, are preferentially located at the core of garnets in metatexites (Figs. 6.1A-B), whereas they do not have a preferential arrangement within anhedral garnets of the mylonite, where they occur both at the core and close to rim (Figs. 6.1C-D). MI may also have a spiral-like arrangement in some mylonitic garnets (Fig. 6.1E). No compositional discontinuities have been observed between MI-rich and MI-free portions of the garnets (see Chapter 5). MI do not form trends along linear discontinuities of the host crystal. In those cases where the garnet has been partially replaced by biotite + sillimanite, the cluster of MI may be in contact with the resorbed

boundary of the host (Fig. 6.1F). MI generally do not occur in the surroundings of mineral inclusions (i.e., biotite or quartz) or fractures in mylonitic garnet, similarly to what has been observed in Grt from anatectic enclaves by Acosta-Vigil *et al.*, (2007).

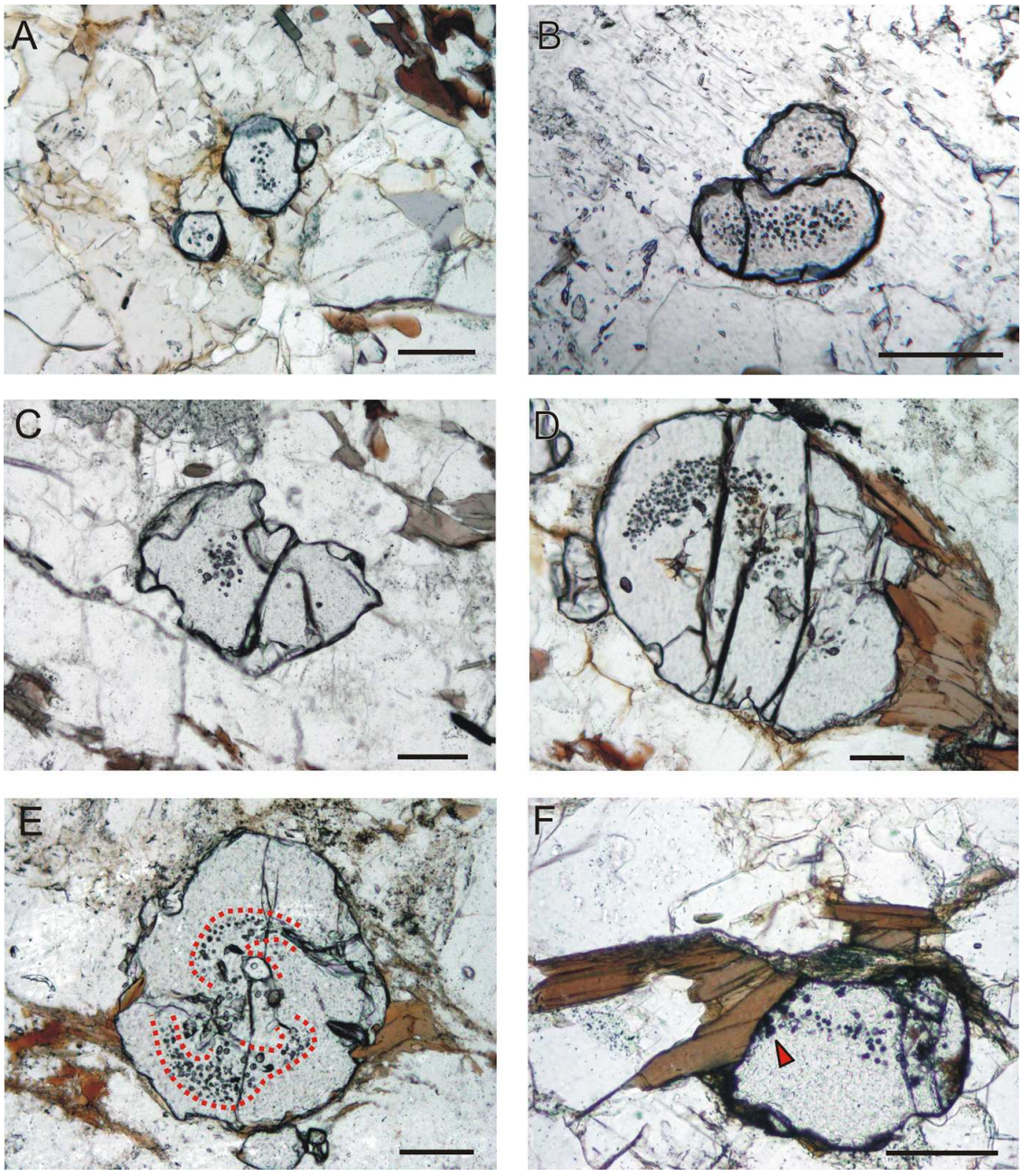

Figure 6.1: Photomicrographs of MI-bearing garnets, PPL. A-B) Small garnet crystals in metatexite with MI clusters at the core. C-E) Garnet in mylonitic migmatites, showing a different arrangement of MI clusters: at the core in C, close to the garnet rim in D and spiral-shaped (red dotted lines) in E. F) MI (red arrow) touching the rim of a garnet partially replaced by Bt+Fib in the metatexite. Scalebar: 100 µm.

In transmitted light under the optical microscope, most of MI appear totally or partially dark-brownish (Figs. 6.2A-B) and contain a polycrystalline aggregate of birefringent crystals under cross polarized light (Figs. 6.2C-D). Other MI are transparent in transmitted light and contain an homogeneous isotropic phase under crossed polarized light; in garnets from mylonites they may show a bubble (Fig. 6.2E). Raman spectroscopy indicated that these bubbles are empty and thus represent shrinkage bubbles. In the mylonites, some dark-brownish MI mantle fibrolite needles (Fig. 6.2F). The shape of both types of inclusion is isometric and their size does not exceed 15 µm (average size ~ 5 µm).

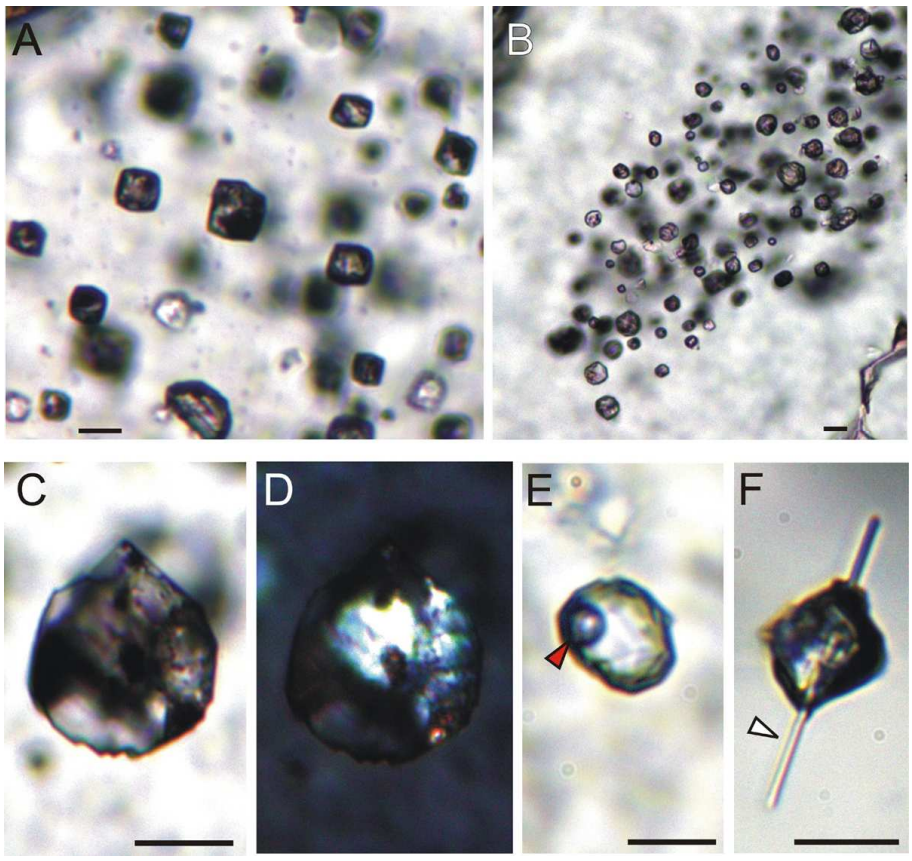

Figure 6.2: Photomicrographs of MI in garnet. A-B) Close-up of MI clusters in metatexite (A) and mylonite (B), both PPL. C-D) PPL and XPL images, respectively, of a crystallized inclusions in metatexite. E) Glassy MI in mylonite showing a shrinkage bubble (red arrow), PPL. F) PPL image of a crystallized inclusion with a sillimanite needle (white arrow), that is likely to have favoured the entrapment of melt. Scalebar: 5 µm.

6.1.2 Microstructures and phase assemblage

When MI are investigated with the FESEM and ESEM, they appear typically facetted, and often with a well-developed negative crystal shape (Figs. 6.3, 6.4 and 6.6).

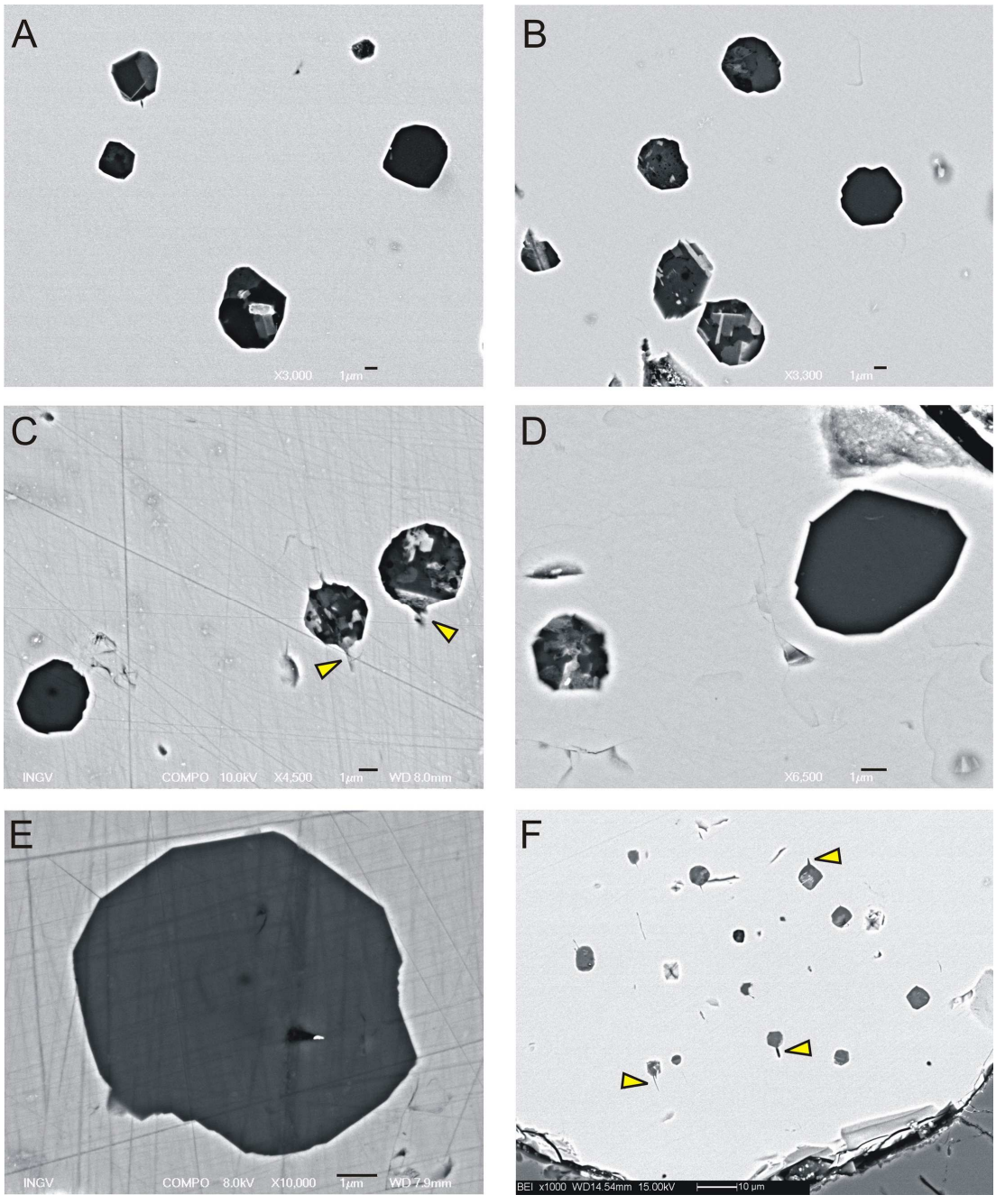

Figure 6.3: FESEM BSE images of coexisting preserved glassy and crystals-bearing MI in metatexite (A) and in mylonite (B-F). Yellow arrows: decrepitation cracks. Scalebar in A-E: 1 µm.

This shape is more properly developed in MI from metatexites. MI show a variable degree of crystallization, even in the same cluster (Figs. 6.3A-D), that ranges from totally crystallized MI, to partially crystallized MI, and down to crystals-absent MI (glassy MI). The relative abundance of these three microstructural types varies between metatexite and mylonite. In metatexites, partially crystallized MI are the most abundant (Fig. 6.6), and glassy MI are very rare (Fig. 6.3A). Conversely, partially crystallized MI are rare in the mylonites, where fully crystallized (Fig. 6.4) and glassy (Figs. 6.3B-E) MI are common. No systematic difference in diameter between the different types of inclusions is observed. Indeed, the size of glassy MI is often equal to (Figs. 6.3A-C), and sometimes even larger than (Figs. 6.3D-E), that of the partially or totally crystallized inclusions. Decrepitation tails may occur in crystallized inclusions hosted in garnets of mylonites (Figs. 6.3C and F).

Crystallized inclusions contain aggregates of quartz, biotite, muscovite, plagioclase and K-feldspar with equigranular, hypidiomorphic to allotriomorphic texture (Fig. 6.4). Crystal size ranges from hundreds of nm to a few µm. The two-dimensional observation of MI exposed on the garnet surface by SEM (Figs. 6.4) provides only apparent modal information that can be misleading. The SEM investigation of tens of MI highlights some differences in the mode of fully crystallized MI from the two studied migmatites. In the metatexites, MI generally contain quartz, biotite, muscovite, plagioclase and rare K-feldspar (Figs. 6.4A-B), whereas the assemblage quartz, biotite, muscovite, K-feldspar and minor plagioclase is common in garnets from mylonites (Figs. 6.4C-F); here, apatite can also be present (Figs. 6.4 C-D). The largest grains within crystallized MI generally consist of subhedral to euhedral micas, $\leq$2 µm in size, which often grew starting from the inclusion walls (Figs. 6.4A, C and D) and are likely to be the first phases to have crystallized. Feldspars form subhedral to anhedral crystals, whereas quartz occurs as an interstitial phase. Sometimes granophyric to microgranophyric intergrowths of quartz and feldspars are present (Figs. 6.4B and F), mostly in MI from mylonite. Owing to these microstructural features typical of plutonic rocks (although at 3-4 orders of magnitude smaller), that testify for the crystallization of a former silicate melt to the granitic assemblage quartz + feldspars

+ micas, and according to Cesare *et al.*, (2009), the cryptocrystalline aggregate found within fully crystallized MI has been named “nanogranite”.

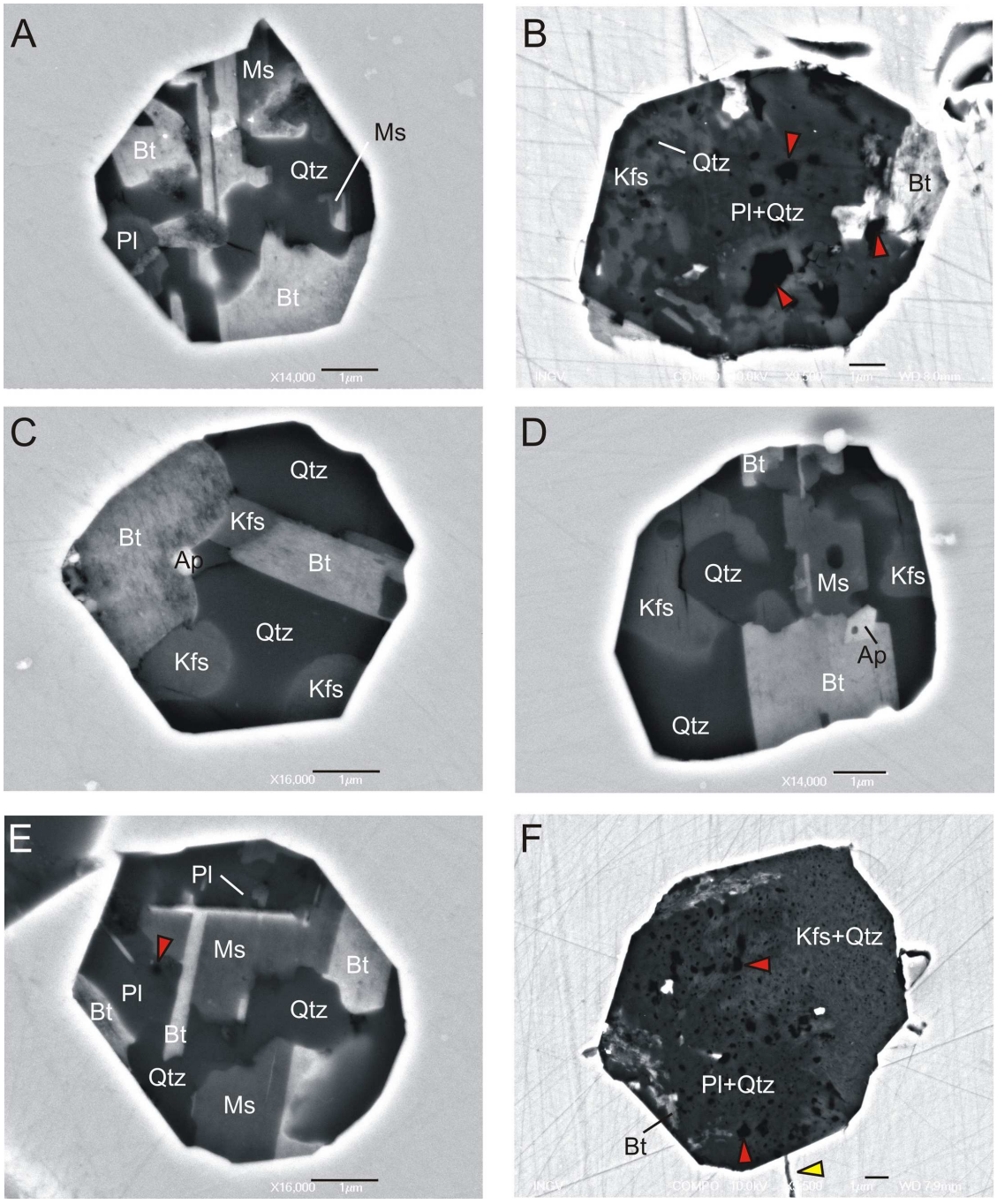

Figure 6.4: FESEM BSE images of nanogranite inclusions in metatexite (A-B) and mylonite (C-F). Red arrows: primary nanoporosity; yellow arrow: microfractures. X-ray maps of some MI are reported in the Supplementary Material (Fig. S1-S3). Scalebar: 1 µm.

Some nanogranites display a variable micro- to nano-porosity, that is greater in the samples from metatexites (Figs. 6.4B and F). Here, micro-Raman mapping of some crystallized MI located below the garnet surface documented the presence of micro- and nano-pores filled with liquid H_2O (Fig. 6.5), suggesting H_2O exsolution during crystallization of hydrous melts to nanogranites. The Raman spectrum also confirms the occurrence of biotite and muscovite into nanogranites (Fig. 6.5A).

Partially crystallized inclusions are indistinguishable from nanogranites at the optical microscope because of their small size. The presence of glass together with crystals is only revealed by SEM investigation.

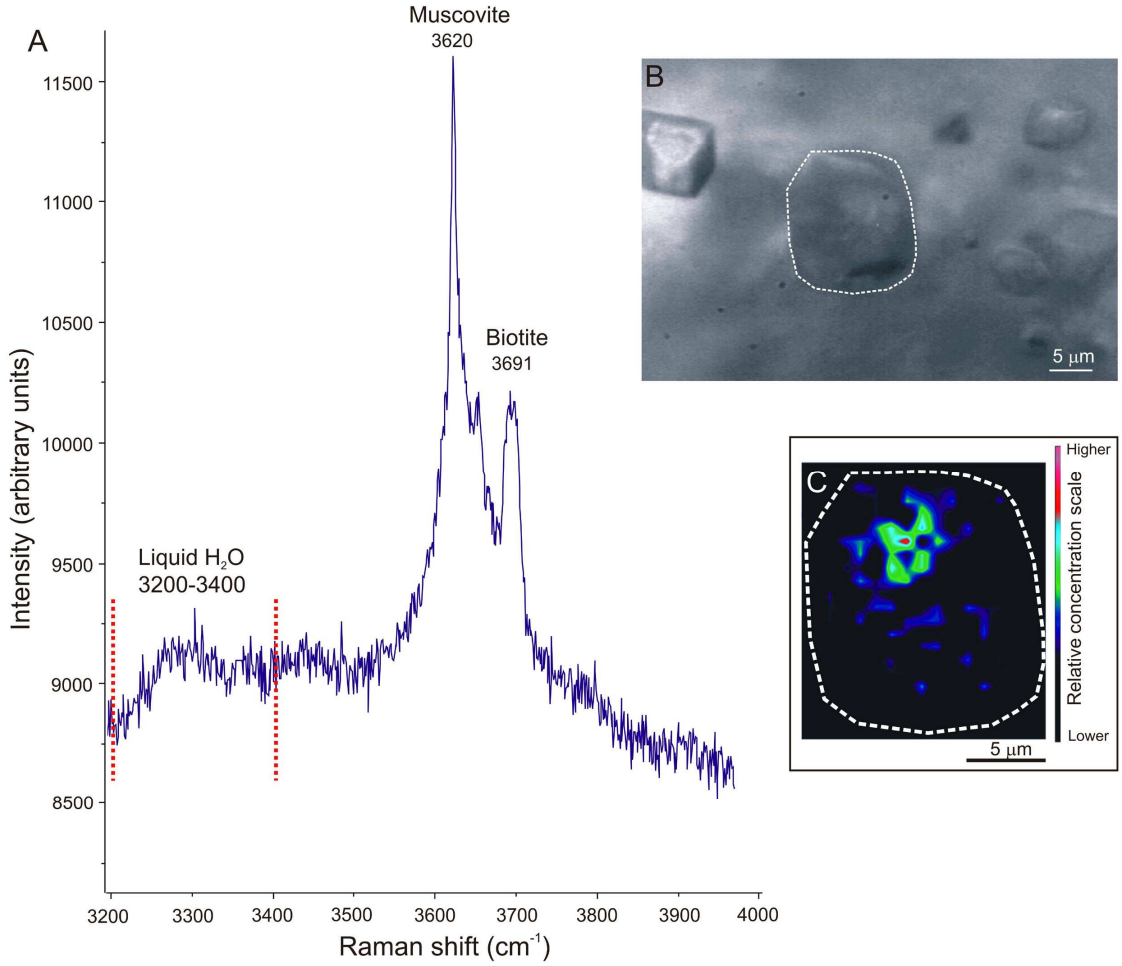

Figure 6.5: Raman mapping of liquid H_2O distribution within a crystallized melt inclusion (nanogranite). (A) Representative Raman spectrum obtained from mapping: the peaks at 3620 and 3691 cm^{-1} correspond to main OH stretching vibrations in muscovite and biotite, respectively. (B) Investigated inclusion below garnet surface, PPL. (C) Raman map in the 3200-3400 cm^{-1} stretching region (bounded by red dotted lines in A) of liquid H_2O. The inclusion contains both hydroxylated minerals and free H_2O in the pores.

Glass occupies different area percentages of the MI (Fig. 6.6), and commonly coexists with muscovite, biotite and quartz in the partially crystallized MI from the metatexite (Figs. 6.6A-D); more rarely, Na-rich plagioclase is the only phase present with glass (Fig. 6.6E). In the mylonite, rare partially crystallized MI generally contain only muscovite and/or biotite along with the glass (Fig. 6.6F).

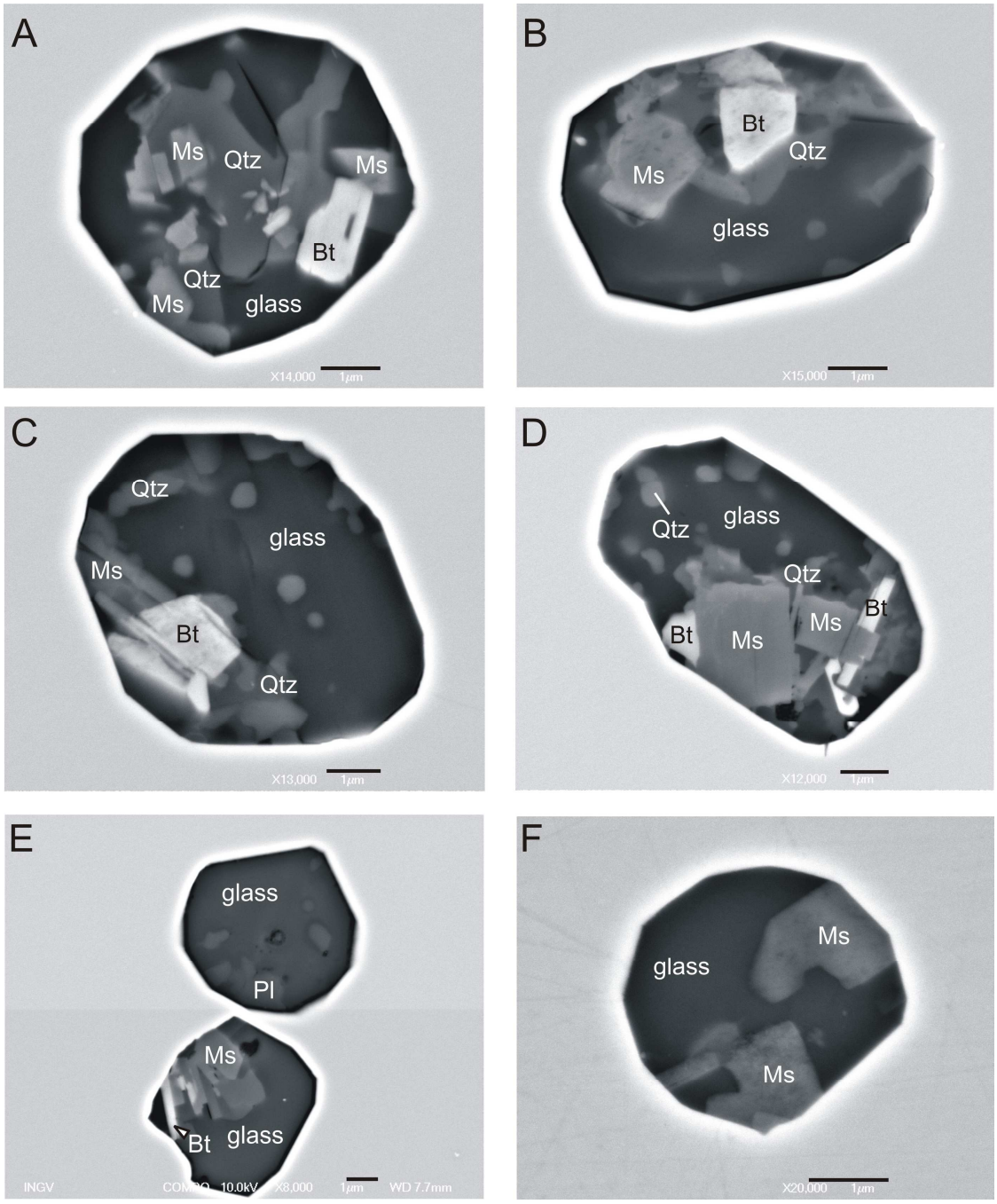

Figure 6.6: FESEM BSE images of partially crystallized MI in metatexite (A-E) and mylonite (F). Scalebar: 1 µm.

6.1.3 Microstructures after remelting experiments

The aim of the experimental remelting of MI is to reheat the inclusions to, or close to, the temperature at which they were trapped and, thus, to reverse the phase changes that occurred during cooling (crystallization and fluid exsolution in bubbles) until an homogeneous liquid is obtained. Once this is accomplished, the melt obtained after heating is quenched to glass so that it can be analyzed by EMP or other techniques.

Owing to the rarity of preserved glassy MI in metatexites, a key problem was to remelt the nanogranites and partially crystallized MI in order to make them analyzable and obtain a reliable estimation of MI chemistry. The first remelting experiments were performed at room pressure using the high-temperature heating stage, a routine technique in igneous petrology (Frezzotti, 2001; Bodnar and Student, 2006). Despite the use of different heating ramps (see Chapter 4) to re-homogenize the nanogranite and partially crystallized inclusions, remelted inclusions show always the occurrence of many decrepitation cracks and newly formed hercynite crystals along with glass (Fig. 6.7). Fractures may extend for several µm into the garnet host, and contain both glass and hercynite.

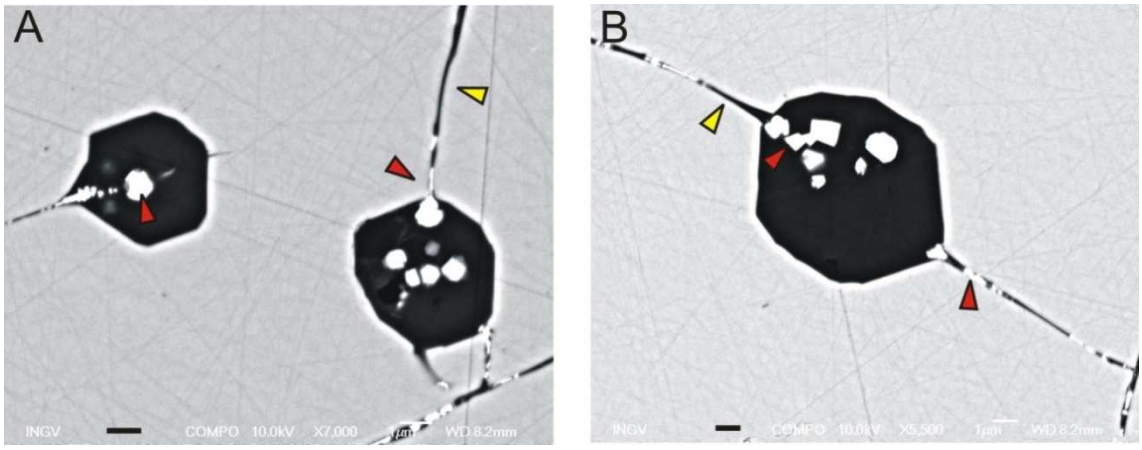

Figure 6.7: FESEM BSE images of remelted MI after experiments using the high-temperature heating stage. Red arrows: hercynite crystals; yellow arrows: decrepitation microfractures. Scalebar: 1 µm.

The Fe-Al-bearing spinel (never observed before heating) is likely a product of garnet-melt interaction due to overheating and inclusion decrepitation during the remelting experiments. These inclusions are therefore unsuitable for a geochemical study.

To overcome these problems, nanogranites and partially crystallized inclusions have been also remelted in a piston cylinder apparatus at 5 (±0.4) kbar, for 24h, both under dry and H_2O added conditions (see Chapter 4). Since the minimum remelting temperature obtained through the heating stage experiments is ~780 (±15) °C, the piston cylinder experiments were initially run at 800 (±5) °C but also at 750 and 700 (±5) °C, in order to constrain the minimum re-homogenization temperature and, thus, the temperature of entrapment of MI. I have found no microstructural differences in remelted MI obtained from dry and wet experiments. It has been observed that the smaller inclusions generally remelt at each run and that the number of remelted MI increases with increasing experimental temperature.

After the experimental run at 800 °C, the fully remelted MI (Fig. 6.8) are often characterized by the occurrence of ≤4 µm long decrepitation cracks and one or more bubbles, and hence they represent partially re-homogenized MI. The glass-to-bubble ratios are variable in the several MI of the same cluster (Fig. 6.8C). Remelted MI generally show irregular boundaries (Figs. 6.8C-F), and MI with a fully-developed negative crystal shape are rare (Fig. 6.8A). At 750 °C, remelted MI still display cracks and bubbles (Fig. 6.9); however, the percentage of MI with a well-developed negative crystal shape (Fig. 6.9B) increases with respect to the 800 ºC runs. Some bubbles hosted in MI remelted at 800 and 750 °C have been analyzed by Raman spectroscopy (see Chapter 3). These bubbles contain vapour CO_2 with a density of 0.14 g/cm^3 (Fig. 6.10 and Tab. 6.1). After the experimental remelting at 700 °C, MI reached a complete melt + vapour homogenization (hence they represent fully re-homogenized MI), without decrepitation and/or the occurrence of bubbles (Fig. 6.11). Here, MI still preserve the original negative crystal shape, suggesting that the host garnet did not dissolve into the melt during heating, and therefore that the trapping temperature was not significantly exceeded.

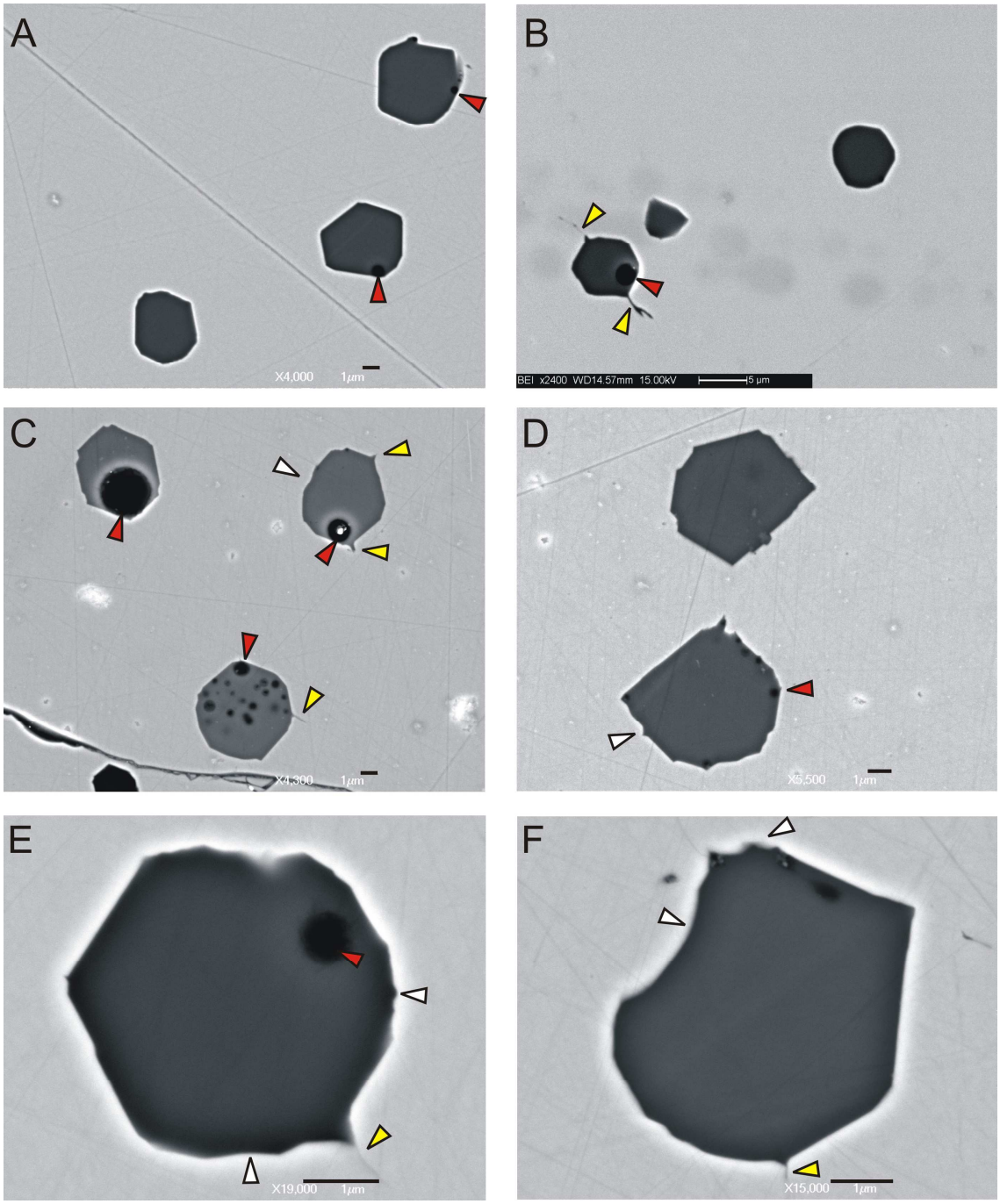

Figure 6.8: FESEM BSE images of MI re-homogenized through piston cylinder experiments at 800 °C and 5 kbar. Red arrows: bubbles; yellow arrows: decrepitation cracks; white arrows: irregular boundaries. Scalebar in A and C-F: 1 µm.

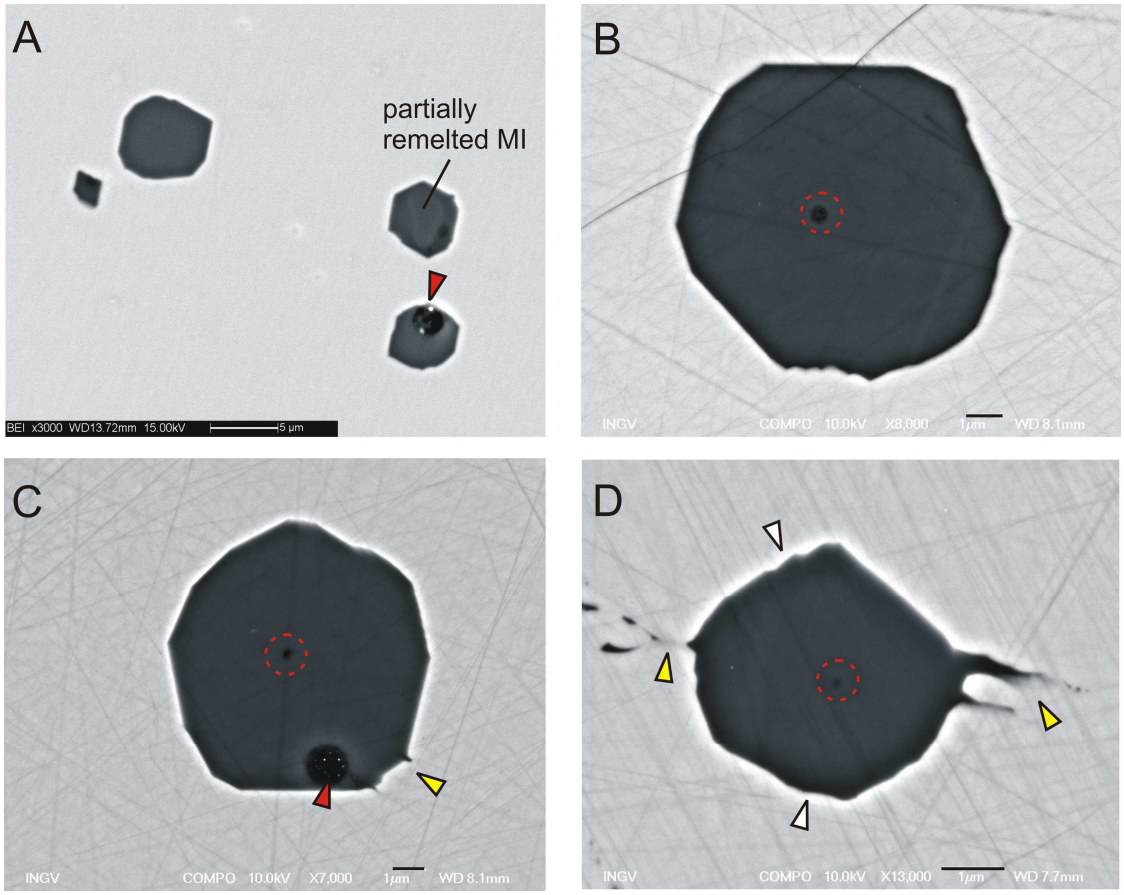

Figure 6.9: FESEM BSE images of re-homogenized MI after piston cylinder experiments at 750 °C and 5 kbar. Red arrows: bubbles; yellow arrows: decrepitation cracks; white arrows: irregular boundaries; red dashed circle: EMP pit. Scalebar in B-D: 1 µm.

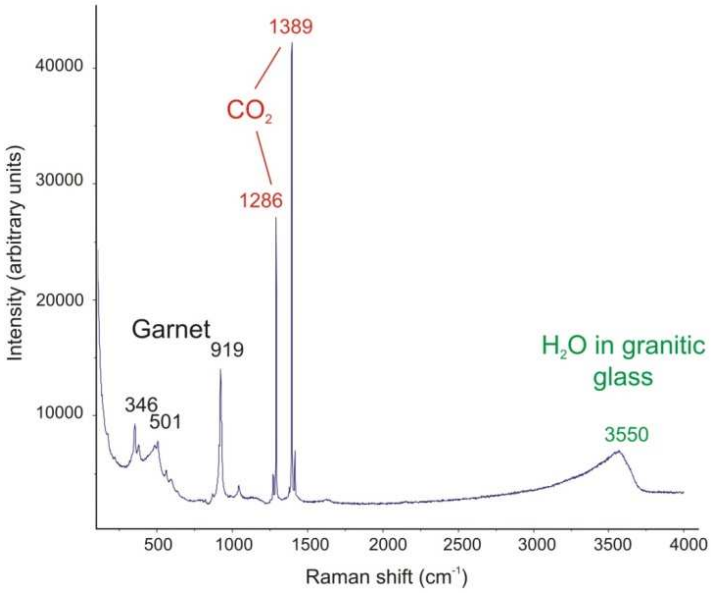

Figure 6.10: Representative Raman spectrum of a CO_2 bubble within a remelted MI, preserved below the inclusion surface. The asymmetric OH stretching band centered at 3550 cm^{-1} indicates that H_2O is present into the glass.

Table 6.1: Raman results of CO_2 density at room temperature in bubbles from melt inclusions remelted at 800 and 750 °C. ν+ and ν- represent the upper and lower bands respectively of Fermi diad. Δ: difference between the positions of the ν+ and ν- bands. ρ: density of CO_2. Numbers in parentheses refer to 1σ standard deviations.

No. analyses	4
ν+ (cm^{-1})	1389.47 (0.78)
ν- (cm^{-1})	1286.46 (0.79)
Δ (cm^{-1})	103.01 (0.00)
ρ (g/cm^3)	0.14 (0.00)

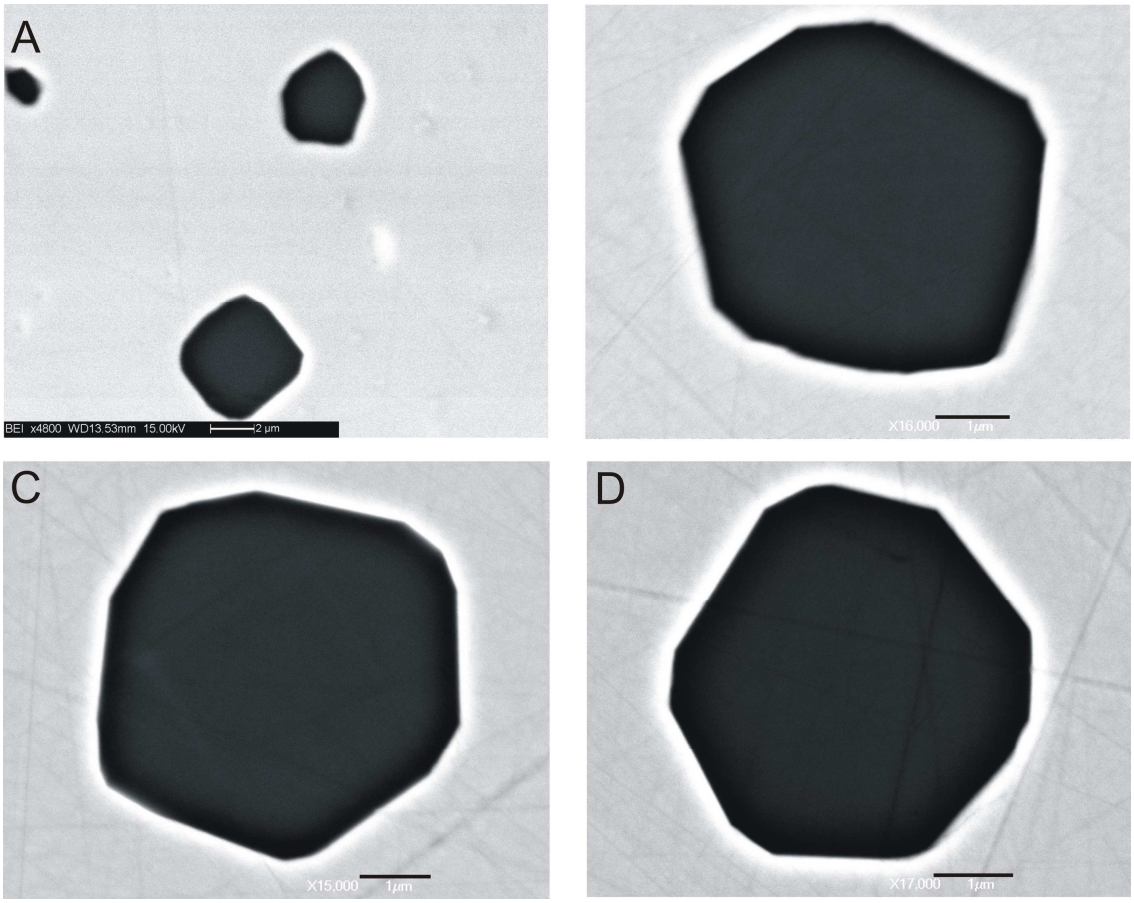

Figure 6.11: FESEM BSE images of fully re-homogenized MI after piston cylinder experiments at 700 °C and 5 kbar. Scalebar in B-D: 1 µm.

6.2 Composition of the melt inclusions

Chemical analyses have been undertaken on preserved glassy and fully re-homogenized inclusions, after a detailed optical investigation to verify their homogeneity and the absence of decrepitation cracks.

6.2.1 Glassy melt inclusions

Mean EMP data for glassy MI in metatexites (3 inclusions) and mylonites (39 inclusions) are reported in Tab. 6.2, and the complete dataset is presented in the Supplementary Material (Tabs. S9-S11). All the analyzed glassy MI contain a peraluminous leucogranitic melt. Glassy MI in metatexites have rather constant and moderately peraluminous compositions, with Na_2O/K_2O from 0.7 to 0.8 and Mg# from 0.06 to 0.14. Conversely, the composition of glassy MI in the mylonites is much more variable, richer in SiO_2, FeO, MgO and P_2O_5, lower in CaO, and moderately to strongly peraluminous. In particular, these inclusions are highly variable in Na_2O and K_2O, such that I have classified them into two groups: type I, with $Na_2O/K_2O < 0.5$, and type II, with $Na_2O/K_2O > 0.6$. Type I and II glassy MI have been found together only in two garnets out of a total investigated of ~20. Also, the two different types can occur both in garnets from leucosomes and neosomes.

In terms of CIPW normative values, the analyzed glassy MI have variable Qtz, Ab and Or contents. The An content is low, ≤1.25 in MI from metatexites and ≤0.85 in MI from mylonites. All the analyzed melts are corundum-normative. When plotted in a Qtz-Ab-Or ternary diagram, the data from type I and type II glassy MI of mylonites define two different clusters (Fig. 6.12). The compositions of the glassy MI from metatexite overlap those of type II glassy MI from mylonite. All MI plot in the Qtz field, close to the 5 kbar cotectic curve and at some distance from the eutectic melt compositions of the haplogranite system.

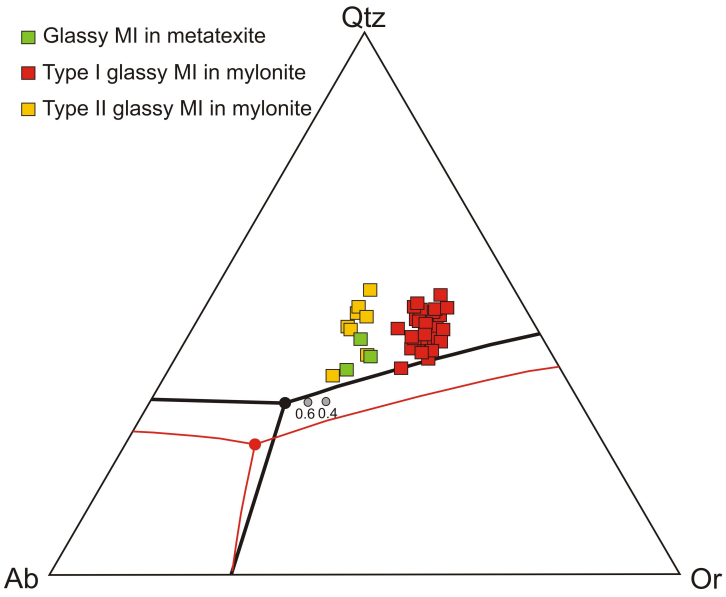

Figure 6.12: Normative CIPW compositions of the preserved glassy MI in the Qtz-Ab-Or diagram. Black dot and lines refer to the eutectic point and cotectic lines for the subaluminous haplogranite system at 5 kbar and a_{H_2O}=1; grey dots: eutectic points at a_{H_2O}=0.6 and 0.4 (Becker *et al.*, 1998). Red dot and lines: eutectic point and cotectic lines for the subaluminous haplogranite system at 10 kbar and a_{H_2O}=1 (Johannes and Holtz 1996). In the peraluminous system, the cotectic curves move slightly towards more Q-rich compositions (Holtz *et al.*, 1992).

Table 6.2: Mean EMP analyses of preserved glassy MI. Numbers in parentheses refer to 1-sigma standard deviations.

Sample	Metatexite	Mylonite	
No. analyses	3	Type I (30)	Type II (8)
SiO_2	69.69 (1.76)	76.33 (1.48)	75.97 (2.20)
TiO_2	0.08 (0.14)	0.05 (0.08)	0.07 (0.07)
Al_2O_3	11.78 (0.32)	11.35 (0.53)	11.30 (0.73)
FeO*	1.20 (0.11)	1.60 (0.050)	1.34 (0.34)
MnO	0.09 (0.09)	0.06 (0.06)	0.08 (0.08)
MgO	0.07 (0.03)	0.17 (0.11)	0.15 (0.15)
CaO	0.39 (0.19)	0.07 (0.04)	0.14 (0.17)
Na_2O	3.09 (0.24)	1.96 (0.35)	3.05 (0.51)
K_2O	4.19 (0.23)	5.76 (0.36)	3.98 (0.33)
P_2O_5	0.18 (0.27)	0.23 (0.23)†	0.29 (0.29)‡
Total	90.75 (1.61)	97.54 (1.60)	96.30 (1.08)
Na_2O/K_2O	0.74 (0.09)	0.34 (0.06)	0.77 (0.11)
ASI	1.15 (0.09)	1.19 (0.10)	1.19 (0.12)
#Mg	0.09 (0.04)	0.14 (0.06)	0.13 (0.11)
CIPW norm			
Qtz	34.23 (2.86)	41.20 (2.68)	41.56 (5.06)
Crn	1.87 (0.63)	1.86 0.89)	1.91 (1.02)
Or	24.77 (1.34)	34.02 (2.15)	23.50 (1.95)
Ab	26.11 (2.07)	16.56 (2.98)	25.84 (4.29)
An	0.83 (0.72)	0.13 (0.22)	0.18 (0.23)

*Total Fe as FeO
ASI = mol. $Al_2O_3/(CaO+Na_2O+K_2O)$
#Mg = mol. $MgO/(MgO+FeO)$
†Values based on 24 analyses
‡ Values based on 6 analyses

6.2.2 Remelted melt inclusions in metatexite

Mean EMP data for remelted MI in metatexites at different experimental conditions are reported in Tab. 6.3, and the complete dataset is presented in the Supplementary Material (Tabs. S12-S17). All the analyzed MI contain a peraluminous granitic melt, and the compositions of remelted MI from dry and wet experiments are indistinguishable.

Table 6.3: Mean EMP analyses of the re-homogenized MI in the metatexite. Numbers in parentheses refer to 1-sigma standard deviations.

Exp. temperature	800°C		750°C		700°C	
Exp. conditions	dry	wet	dry	wet	dry	wet
No. analyses	14	14	16	12	15	13
SiO_2	69.42 (2.01)	69.83 (1.42)	69.24 (2.18)	69.41 (2.43)	70.03 (2.36)	69.60 (1.86)
TiO_2	0.06 (0.07)	0.07 (0.07)	0.05 (0.07)	0.05 (0.06)	0.04 (0.07)	0.06 (0.07)
Al_2O_3	11.67 (1.15)	12.05 (0.73)	12.52 (0.99)	12.59 (0.47)	11.71 (0.89)	12.06 (0.49)
FeO*	2.43 (0.65)	2.43 (0.52)	2.20 (0.54)	2.29 (0.33)	1.71 (0.22)	1.74 (0.25)
MnO	0.17 (0.11)	0.20 (0.12)	0.27 (0.18)	0.21 (0.20)	0.17 (0.10)	0.16 (0.10)
MgO	0.18 (0.06)	0.21 (0.12)	0.24 (0.12)	0.26 (0.12)	0.12 (0.07)	0.12 (0.07)
CaO	0.47 (0.09)	0.48 (0.20)	0.43 (0.09)	0.52 (0.10)	0.45 (0.13)	0.45 (0.10)
Na_2O	2.43 (0.33)	2.75 (0.62)	2.75 (0.47)	2.63 (0.45)	2.79 (0.37)	2.85 (0.50)
K_2O	3.79 (0.59)	3.80 (0.45)	4.03 (0.33)	3.93 (0.61)	4.05 (0.41)	4.08 (0.30)
P_2O_5	0.30 (0.22) †	0.24 (0.07) ‡	0.22 (0.31)′	n.d.	0.26 (0.24)	0.22 (0.14)
Total	90.76 (3.09)	91.86 (2.05)	91.76 (2.22)	91.90 (2.72)	91.33 (2.26)	91.34 (2.12)
Na_2O/K_2O	0.64 (0.18)	0.74 (0.22)	0.68 (0.11)	0.67 (0.17)	0.70 (0.13)	0.70 (0.14)
ASI	1.31 (0.13)	1.28 (0.11)	1.30 (0.14)	1.34 (0.15)	1.20 (0.08)	1.22 (0.10)
#Mg	0.11 (0.02)	0.11 (0.05)	0.14 (0.05)	0.15 (0.06)	0.10 (0.06)	0.10 (0.05)
CIPW norm						
Qtz	37.70 (2.82)	35.94 (3.86)	34.57 (2.62)	35.50 (3.31)	36.12 (3.70)	35.31 (2.62)
Crn	2.98 (1.40)	2.65 (0.97)	2.90 (1.26)	3.06 (1.14)	2.36 (0.91)	2.64 (1.08)
Or	22.41 (3.51)	22.44 (2.67)	23.84 (1.94)	23.25 (3.59)	23.95 (2.40)	24.14 (1.77)
Ab	20.55 (2.81)	23.27 (5.27)	23.23 (4.00)	22.26 (3.78)	23.64 (3.09)	24.11 (4.19)
An	1.59 (0.90)	2.09 (1.33)	2.03 (0.70)	2.58 (0.49)	0.99 (1.20)	0.84 (0.58)

Total Fe as FeO
ASI = mol. $Al_2O_3/(CaO+Na_2O+K_2O)$
#Mg = mol. MgO/(MgO+FeO)
†Values based on 7 analyses
‡ Values based on 3 analyses
′ Values based on 2 analyses
n.d.: not detected.

The average composition of remelted inclusions at 800 and 750 °C generally differs from that of preserved glassy inclusions, showing higher FeO, MnO, MgO, CaO, ASI

and #Mg (Tabs. 6.2 and 6.3, Fig. 6.13). The average composition of MI re-homogenized at 700 °C is much more comparable to those of glassy inclusions, although remelted MI still show slightly higher values in the above compositional variables than glassy MI (Fig. 6.13D). However, similar FeO contents (1.72±0.51 wt%) have been reported in the literature for glassy inclusions trapped at ~700 °C within garnets of high-grade anatectic enclaves (Acosta-Vigil *et al.*, 2007).

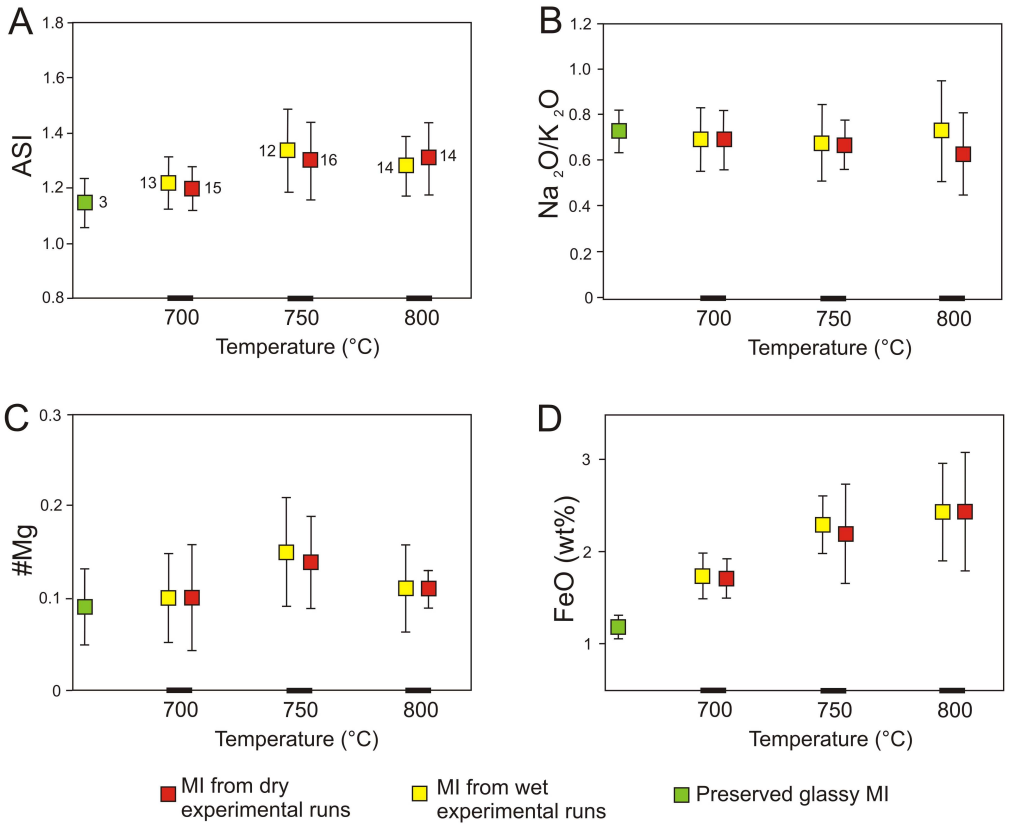

Figure 6.13: Plots of A) Aluminium saturation index (ASI), B) Na_2O/K_2O, C) #Mg and D) FeO of the experimental remelted MI *vs.* temperature. Preserved glassy MI are plotted for comparison. The number of analyses is indicated next to data boxes in (A). Vertical bars indicate the standard deviation (1σ) on average values.

When plotted in a Qtz-Ab-Or normative diagram (Fig. 6.14), the data from dry and wet runs overlap, but the scatter of the data clearly decreases with decreasing experimental temperature. Thus, at 700 °C the normative compositions of fully re-homogenized MI are strictly comparable with those of preserved glassy MI and plot close to the 5 kbar haplogranite eutectic at $a_{H_2O} < 0.5$ (Fig. 6.14C).

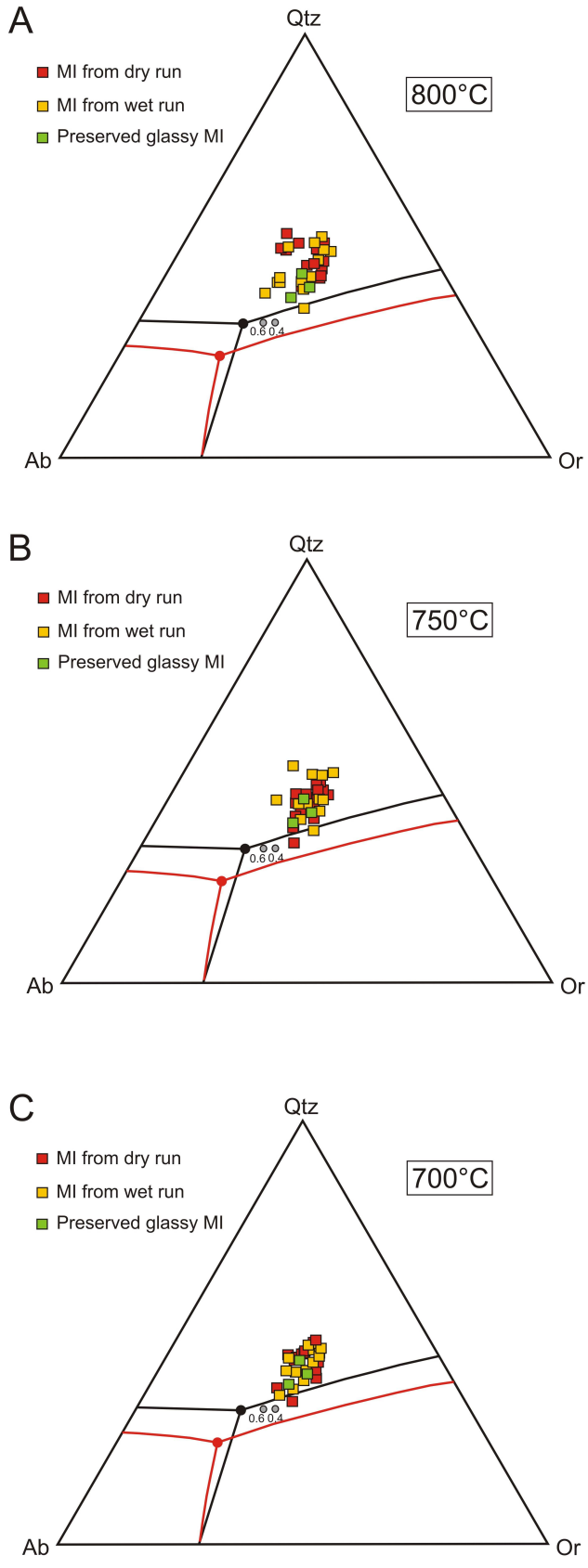

Figure 6.14: Normative composition of the analyzed inclusions after experimental remelting at A) 800 °C, B) 750 °C and C) 700 °C and 5 kbar. Preserved glassy MI are plotted for comparison. Black, grey and red symbols as in Figure 6.12

6.2.3 H_2O content of melt inclusions

Since H_2O is the main volatile in S-type felsic melts and has a great influence on the physical properties of magmas, its precise quantification is of paramount importance (Hess and Dingwell, 1996; Baker, 1998). Given the small size of the studied MI, the most promising method of H_2O analysis is the Raman spectroscopy (Thomas, 2000; Müller *et al.*,, 2006; Thomas *et al.*,, 2006). H_2O contents by Raman have been measured for the preserved glassy MI in mylonite and the fully re-homogenized MI at 700 °C in metatexite (Fig. 6.15)

The H_2O content of the glass in re-homogenized MI from metatexites ranges from 3.1 to 7.6 wt% (Fig. 6.15A). This variability is in accordance with the variable microprobe totals (Tab. 6.3). H_2O concentrations calculated by difference (100-microprobe totals), however, are sistematically higher than those provided by Raman spectroscopy. Most of the analyzed MI (~70%) by Raman show H_2O contents between 3.1 and 5.8 wt%, with no difference between remelted MI from dry and wet experiments.

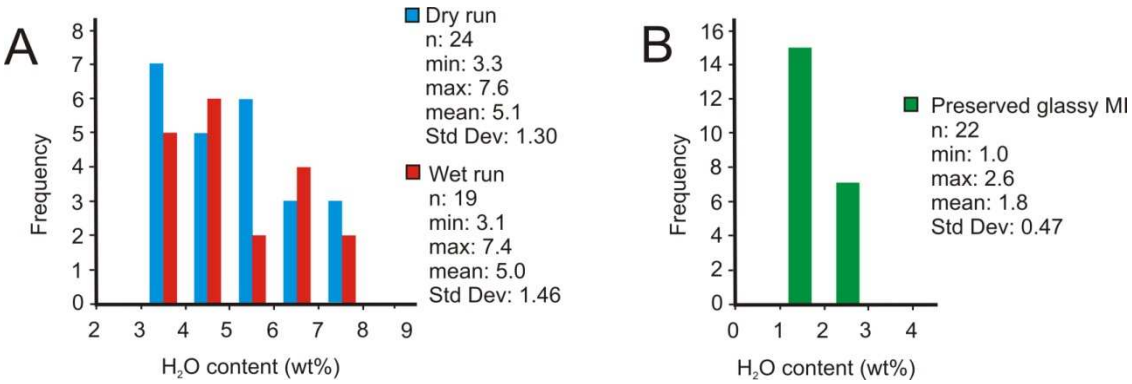

Figure 6.15: Histograms of the H_2O content for the A) experimental re-homogenized MI from metatexite, and B) preserved glassy MI from mylonite.

For the Raman analysis of glassy MI in mylonites, new and fresh MI must have been exposed on the garnet surface after the previous microstructural and compositional characterization. Hence, during Raman analyses it was not possible to distinguish between the type I and type II inclusions. However, microprobe totals of the two types of inclusions overlap within analytical uncertainty (Tab. 6.2), suggesting similar fluids

contents. Glassy MI in mylonites have much lower H_2O concentrations than MI in metatexites, in the range of 1.0-2.6 wt% (Fig. 6.15B). Raman spectroscopy did not even detect any H_2O in some (~30%) of the analyzed MI. Most of the H_2O-bearing MI (~70%) show H_2O contents between 1.0 and 1.9 wt%. These concentrations are again lower than those calculated by difference from the electron microprobe analyses (Tab. 6.2).

6.3 Pseudosection on melt inclusions

A P-T pseudosection was constructed using the measured bulk composition of the fully re-homogenized MI of metatexite, in order to constrain the field where pure melt is stable and, therefore, the conditions of MI entrapment (Fig. 6.16). The modelized chemical system is Na_2O-CaO-K_2O-FeO-MgO-Al_2O_3-SiO_2-H_2O (NCKFMASH), and the pseudosection was calculated using the software Perple_X and the internally consistent thermodynamic data set of Holland and Powell (1998, revised in 2003). Along with a melt phase, the minerals considered in the calculation are garnet, biotite, andalusite, sillimanite, kyanite, muscovite, quartz, plagioclase and K-feldspar. The following solution models were used: melt (White *et al.*, 2007), garnet (Holland & Powell, 2001), white mica (Coggon & Holland, 2002), plagioclase (Newton *et al.*, 1980), K-feldspar (Thompson & Hovis, 1979) and biotite (Tajčmanová *et al.*, 2009). The fluid was considered as pure H_2O (a_{H_2O}=1). The field for pure *liquid* starts at ~750 °C, 4 kbar (Fig. 6.16) and is bordered at low P (about 4 kbar) by the field Liq+H_2O, and to higher P by the field Liq+Grt+Qtz. The lack of H_2O-rich fluid inclusions coexisting with MI, and the absence of Qtz within MI, suggest that MI were trapped in such field. However, the temperature of 750 °C is higher than the lowest temperature at which nanogranites have been experimentally remelted. The fully re-homogenization of nanogranite inclusions without garnet dissolution at 700°C is a strong experimental evidence and indicates that only the melt should be stable at this temperature. Instead, the temperature of 700 ºC represents in the pseudosection the minimum temperature at which liquid coexists only with garnet (field Grt+liq in Fig. 6.16). Since the model for the melt phase used in these thermodynamic calculations was made *"to reflect more*

closely the total Fe + Mg and X_{Fe} = Fe/(Fe + Mg) in experimental melts" as outlined by White *et al.*, (2007), and given that experimental melts have lower FeO and MgO contents than the natural anatectic melts (e.g., Lavaure and Sawyer, 2011), I can only speculate that the above differences in temperature might be related with the melt model used in calculations and the uncertainties in the concentrations of FeO and MgO in the natural melts. Hence, the field Grt+liquid in the pseudosection could be a field in which only the liquid is stable until the minimum temperature of 700 °C.

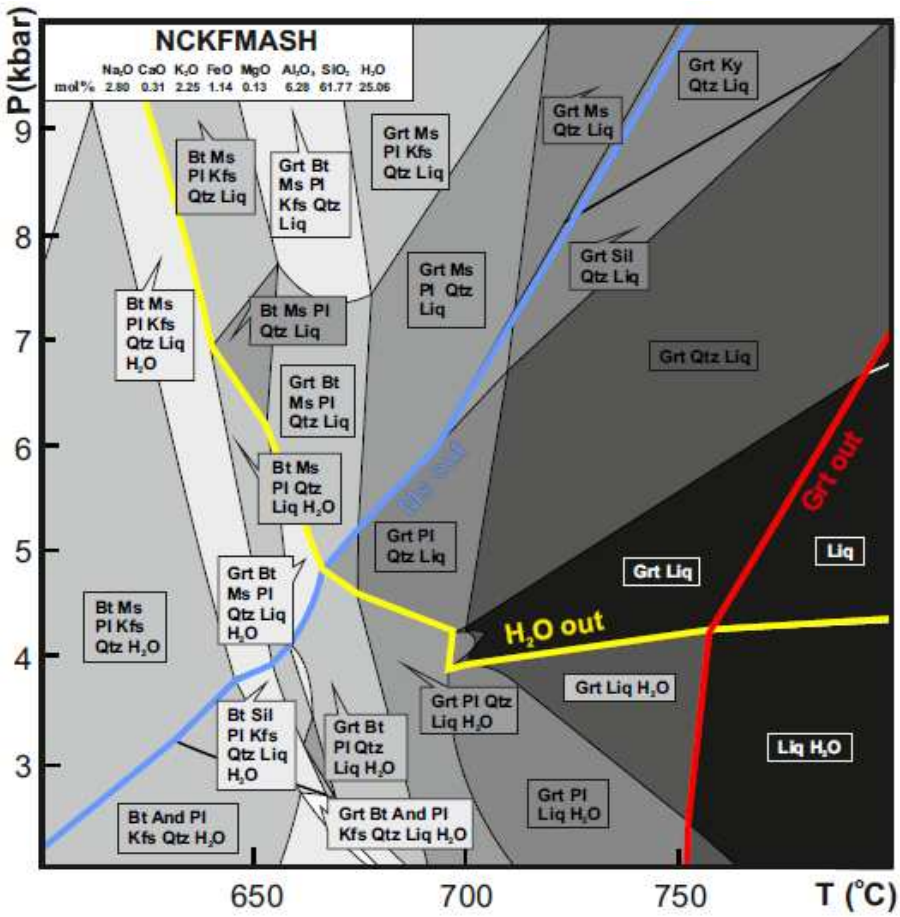

Figure 6.16: P-T pseudosection for the composition of the remelted nanogranite inclusions in the NCKFMASH system. Blue, yellow and red lines refer to the muscovite-, H_2O- and garnet-out curves, respectively.

6.4 Nature of the studied melt inclusions

In the studied quartzo-feldspathic metatexites and mylonites, MI have been found in peritectic garnet. The trapping of melt inclusions is promoted by rapid growth of the host phase that destabilizes the planar crystal-melt interface and creates embayments that may accommodate melt (Baker, 2008), or by fine grain-sized mineral located at the rims of the growing mineral, that acted as surfaces to which the melt could cling (Roedder, 1984). The observed spatial arrangement (Fig. 6.1) is a strong indicator of the primary nature of MI (i.e., they were trapped when garnet was growing, Roedder, 1984) and argues against a secondary origin (e.g., percolation of melt along fractures in the garnet). Hence, these MI represents small samples of the melt coexisting with the garnet during the anatexis of the studied rocks. This mode of occurrence (MI hosted in peritectic phases) is quite different from that of MI hosted by phenocrysts in lavas where the host mineral is crystallizing "from" the melt during cooling (Cesare *et al.*, 2011). In the former case, peritectic minerals and melt form at the same time during the prograde path, i.e. the peritectic garnet is growing "with" the melt.

The negative crystal shape typically found in the studied MI (Fig. 6.3, 6.4 and 6.6) is not a primary feature (Frezzotti, 2001), as confirmed by experiments on fluid inclusions formed in different minerals and artificial crystalline compounds (Maze *et al.*, 1981; Sisson *et al.*, 1993). These inclusion shapes result from reequilibration processes between the host mineral and the inclusions in order to reach the lowest energy configuration. Such a shape is likely to develop through the dissolution and reprecipitation of the host mineral on the inclusions walls, without modifying the inclusion volume and the melt composition (Frezzotti, 2001). Based on microstructural investigations, MI shape maturation predates the beginning of crystallization of the trapped melt, as the first phases to crystallize (micas) are in contact with already planar walls (Figs. 6.4 and 6.6).

Three type of inclusions were identified: nanogranites, partially crystallized inclusions and preserved glassy inclusions. The phase assemblage in crystal-bearing MI (quartz, plagioclase, K-feldspar, muscovite and biotite) indicates that the trapped melt likely had a granitic composition, as confirmed by the analyses of remelted MI. Nevertheless, SEM images only provide apparent modal information owing to the two-

dimensional view. In the partially crystallized MI, the glass represents the residual melt after the partial crystallization of the former trapped melt. One or two micas are generally present (Fig. 6.6), supporting the microstrutural inference that these are the first phases to crystallize. During the crystallization of melts to nanogranites in the garnets of metatexite, H_2O exsolved in micro- and nano-bubbles (Fig. 6.5), but it was also consumed by the crystallizing biotite and muscovite.

Decrepitation cracks can be present in crystal-bearing MI from the mylonite, but they are rare in those from the metatexite, suggesting that MI decrepitation was enhance by deformation that continued during the retrograde path (i.e., in the subsolidus state; see Chapter 5). Additionally, ΔP (the difference between the pressure inside the inclusions and that outside the host mineral) should have been larger in inclusions from the mylonite than in those from the metatexite, owing to the different trapping pressure (i.e. melting pressure). Hence, similar near-isothermal decompression paths would favour the decrepitation of MI in the mylonites over those in the metatexites, as the internal pressure of MI would remain close to that of entrapment (Lowenstern, 1995). Nevertheless, since preserved and decrepitaded MI have the same phase assemblage, it can be inferred that there were no external infiltrations.

The minimum re-homogenization temperature (700 °C) of nanogranites and partially crystallized MI from metatexites can be assumed to be the trapping temperature (Frezzotti, 2001), in partial agreement with the pseudosection modeling for melt inclusions (Fig. 6.16). In addition, when the MI were experimentally remelted at T corresponding to the trapping T, or very close to it, no dissolution of the host mineral took place (Fig. 6.11).

During experimental remelting at temperatures higher than the trapping temperature (750 and 800 °C), small amounts of the host garnet dissolved into the melt (Figs. 6.8 and 6.9) increasing the original FeO contents and ASI and #Mg values (Fig. 6.13 and Tab. 6.3). This increase in the remelting temperature also produced an increase in the internal pressure of the volatile-rich MI (Bodnar and Student, 2006), causing MI decrepitation and hence depressurization. MI depressurization during heating runs at 750 and 800 °C is indicated by the commonly observed opening of microfractures on MI walls (Figs. 6.8 and 6.9). Since the solubility of CO_2 in silicate melts is much lower

than that of H_2O (Tamic *et al.*, 2001), and given that the solubility of CO_2 in rhyolitic melts decreases with decreasing P and/or with increasing T (Moore, 2008; Fogel and Rutherford, 1990), MI depressurization resulted in vesiculation of CO_2 bubbles (Figs. 6.8, 6.9 and 6.10). The occurrence of variable bubble-melt ratios in different MI of the same cluster is a further evidence of bubble vesiculation induced by different extents of inclusion decrepitation and consequently depressurization (Lowenstern, 1995). In addition, the high bubble-melt ratios that are sometimes observed (Fig. 6.8C) suggest volatile loss during decrepitation (Lowenstern, 1995), resulting in the formation of empty bubbles and/or expansion of preexisting bubbles in order to arrange the volume lost by volatile leak (Severs *et al.*, 2007). All these observations, along with the absence of CO_2 bubbles in MI remelted at 700°C, indicate that some CO_2 is dissolved into the melt of fully re-homogenized MI and that the new experimental approach is therefore crucial when performed at temperature corresponding to, or very close to, the trapping temperature, because it maintains the primary fluid contents ($H_2O \pm CO_2$) in the originally trapped melt, that would otherwise be lost during most of the homogenization experiments at room pressure (Bodnar and Student, 2006).

Fully re-homogenized MI at 700 °C in the metatexite show peraluminous leucogranitic compositions similar to those of the coexisting glassy MI (Tabs. 6.2 and 6.3), suggesting that clusters contain inclusions of the same melt, despite the variable degree of crystallization revealed by microstructural investigation. However, FeO is slightly higher in the re-homogenized MI at 700 °C with respect to the glassy inclusions (Fig. 6.13D), even if garnet does not show clear evidences of dissolution (Fig. 6.11). I can only suggest that this might be due to small differences between entrapment and remelting conditions (i.e., MI might have re-equilibrated with the host garnet during the experiments at conditions slightly different than the trapping conditions). However, the main and most important purpose of this work and this new experimental approach to the study of MI, was to be able to bring partially or totally crystallized MI in migmatites to the original or quasi-original composition, i.e. to achieve the MI re-homogenization without cracking and volatile loss. In this sense, the obtained results clearly show that the newly developed method permits a detailed study of the geochemistry of the melt during the anatexis of the host migmatites. In view of the present results, experiments

with a nonlinear progression in run duration could represent the right continuation to improve this new experimental approach for the remelting of nanogranite inclusions.

Glassy MI in the mylonites show peraluminous leucogranitic compositions (Tab. 6.2) quite variable in their Na_2O/K_2O ratio. Type II MI ($Na_2O/K_2O>0.6$) are rare, whereas type I MI ($Na_2O/K_2O<0.5$) are much more abundant, in agreement with the modal abundance of Na- and K-bearing phases into nanogranites of the mylonites (Figs. 6.4C-F). Type II glassy inclusions from mylonites and MI from metatexites have similar Na_2O/K_2O values (Tabs. 6.2 and 6.3).

The diffusion of H_2O and H_2 out of the MI through the host garnet after MI entrapment and during experimental remelting may affect their primary H_2O contents (Frezzotti 2001; Danyushevsky *et al.,* 2002; Severs *et al.,* 2007). However, the low Fe content of the melt reduces the potential of oxidation of the inclusions and, therefore, the maximum amount of dissociate H_2O to permit the diffusion of H_2 (Danyushevsky *et al.,* 2002). Fe-oxides, which would form during H_2O dissociation and H_2 diffusion out of the MI (Danyushevsky *et al.,* 2002) were not observed in the studied inclusions. Moreover, diffusion of H_2O produces haloes of tiny fluid inclusions close to the MI walls (Berry *et al.,* 2008), but none of such microstructures are present in the studied samples. H_2O loss during remelting experiments is also excluded from the H_2O concentrations measured in fully re-homogenized MI from dry and wet runs at 700 °C (Fig. 6.15). From the above it is concluded that the measured H_2O concentrations can be considered representative of the pre-entrapped melt phase, since (i) there are not microstructural evidences of decrepitation in the analyzed inclusions, (ii) the complete re-homogenization of inclusions allowed the re-dissolution of the exsolved fluid into the melt phase, and (iii) the Raman investigation has shown the occurrence of empty shrinkage bubbles in glassy inclusions from the mylonite. MI in the metatexite display higher H_2O concentrations than those in the mylonite (Fig. 6.15).

Since the composition of nanogranites and glassy MI in the metatexite is comparable, their contrasting behaviour upon cooling is unexpected. Glassy inclusions are common in phenocrysts from volcanic rocks which undergo sudden cooling from soprasolidus temperatures. Based on the statistical study of the size of MI found in garnets from migmatitic granulites of the Kerala Khondalite Belt, Cesare *et al.,* (2009)

showed a difference between the mean diameter of the preserved glassy inclusions (smaller) and the crystallized nanogranites (larger), and proposed that crystal nucleation was inhibited in the smaller inclusions. Such pore size effect is well known in crystallization (Putnis *et al.*, 1995) and dissolution kinetics (Emmanuel *et al.*, 2010), and is related to the higher interfacial energy (and consequent lower stability) of the crystals in smaller pores with respect to those in larger ones (Holness & Sawyer, 2008). However, in the studied migmatites the apparent size of glassy MI is often equal to, and sometimes even larger than, that of the nanogranites (Fig. 6.3). This suggests that this range of dimensions (5-10 µm) may represent a threshold at which additional factors may significantly affect nucleation kinetics. One of the main compositional difference between MI in metatexites and mylonites is their H_2O content. High H_2O concentrations increase the diffusivities in MI (Lowenstern, 1995), and would have produced the partial or total crystallization of the majority of MI in metatexite. Conversely, the higher viscosity of the melt in MI from mylonites (due to low H_2O content) would have inhibited the crystallization, with the formation of many glassy MI. However, in some MI the microfracturing and decrepitation (Figs. 6.3 C and F) may trigger crystallization, as commonly recognized in aqueous solution-bearing fluid inclusions, where a pressure drop causes a drop in solubility that leads to the precipitation of daughter phases (Manning, 1994).

Chapter 7
Melt inclusions in other migmatites

This thesis focuses on MI in quartzo-feldspathic metatexites and mylonites, although MI are virtually present in all migmatites outcropping below the Ronda peridotite at Sierra Alpujata. In this chapter, I briefly report some interesting microstructural features of MI in other samples, not studied in detail in the previous chapters.

In the pelitic metatexite ALPA35-2 (a rock mainly composed of quartz, plagioclase, K-feldspar, biotite, sillimanite, cordierite, ilmenite, graphite and rare garnet) MI occur in ilmenite crystals (100-200 µm across) scattered in the melanosome matrix. MI (1.5-20 µm in diameter) are grouped with no preferred microstructural location and appear typically facetted, sometimes with a well-developed negative crystal shape (Fig. 7.1). MI are totally crystallized and contain quartz, plagioclase, biotite and rare apatite (Figs. 7.1B and C).

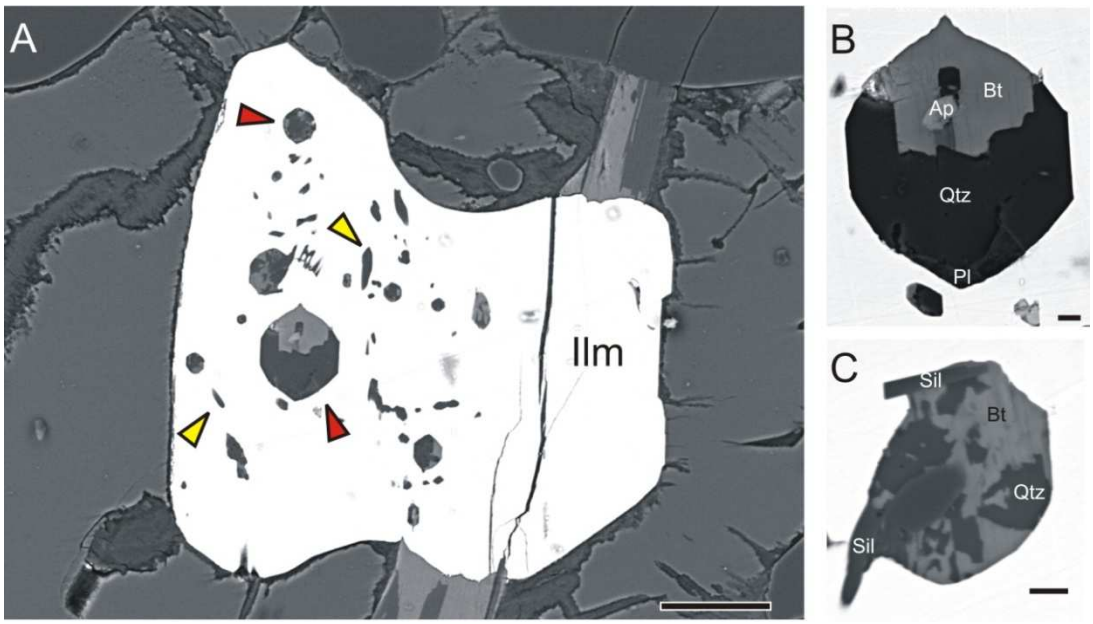

Figure 7.1: A) SEM BSE image of an ilmenite crystal in the pelitic metatexite ALPA35-2, containing primary MI (red arrows). Yellow arrow: sillimanite inclusions. Scalebar: 30 µm. B) and C) FESEM images of crystallized MI hosted in ilmenite. Scalebar: 2 µm.

Silllimanite crystals may be present in some MI with one of their terminations partially enclosed in the host ilmenite (Fig. 7.1C). This microstructural observation along with the occurrence of sillimanite inclusions into the same host (Fig. 7.1A) suggests that sillimanite was trapped together with a melt droplet by the growing (peritectic ?) ilmenite.

In the mylonitic kinzigite ALP14 (a rock mainly composed of quartz, K-feldspar, biotite, sillimanite, garnet, cordierite, graphite and rare plagioclase) outcropping at the contact with the peridotite, rutile needles are present within many of the partially crystallized and glassy MI (2-6 µm in diameter) hosted in peritectic garnet (Fig. 7.2A). The rutile crystals are partially enclosed in the host garnet (Figs. 7.2B and C), supporting the inference that rutile favoured the entrapment of melt.

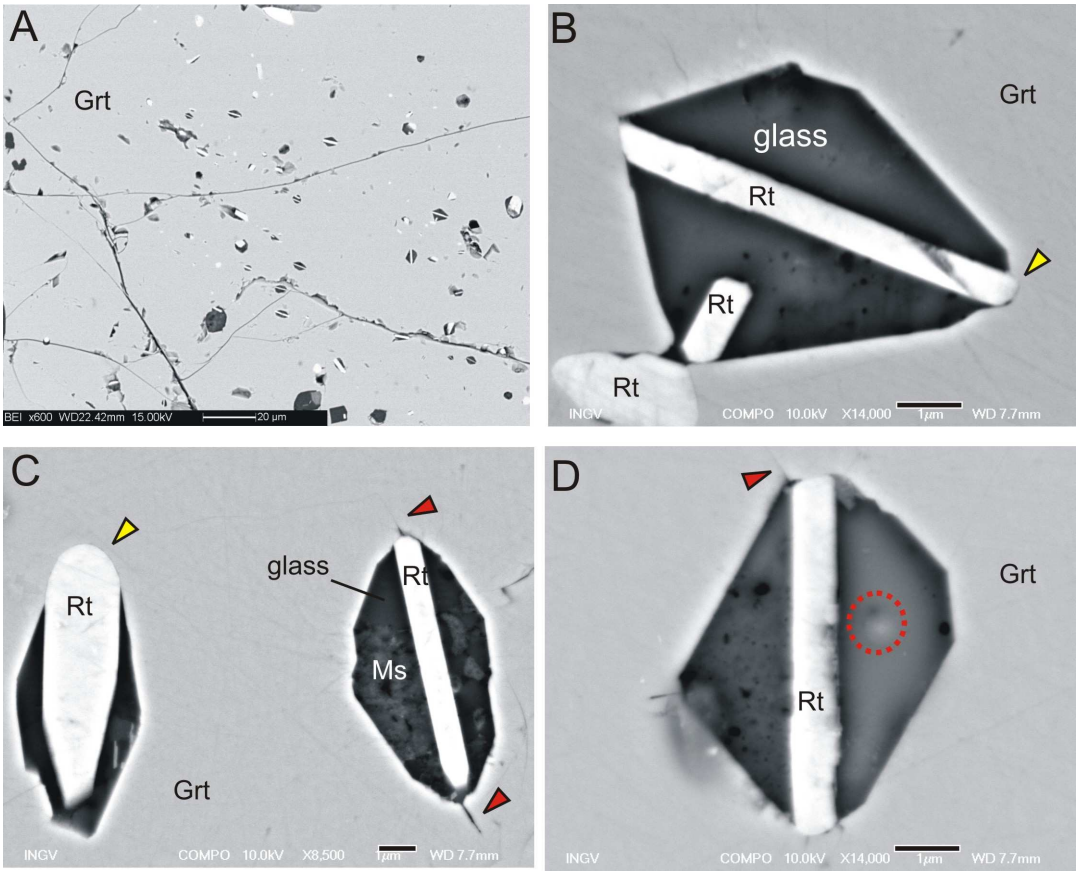

Figure 7.2: A-D) FESEM images of rutile-bearing MI hosted in garnet of the mylonitic kinzigite ALP14. Yellow arrows: termination of the rutile needle partially enclosed in the host garnet. Red arrows: decrepitation cracks. Red dashed circle: EMP pit. Scalebar in B-D: 1 µm.

The EMP analysis of the phase enclosed between the rutile needle and the host garnet in Fig. 7.2D provided a granitic composition with SiO_2=66.2 wt%, Al_2O_3=12.3 wt%, TiO_2=2.2 wt%, FeO=4.1 wt%, Na_2O=0.6 wt% and K_2O=6.7 wt%. Such a composition strongly suggests that this phase is a glass (i.e., the former melt). The high Ti and Fe contents suggest that the volume excited by the EMP beam is affected by the neighboring rutile and garnet. The occurrence of MI that contain, or cling to, a rutile crystal suggests that a fine grain sized protolith containing abundant “inert” accessory phases (graphite, rutile, apatite and zircon; see also Cesare, 2008; Henriquez and Darling, 2009) is more likely to favour the formation of MI during anatexis.

Chapter 8
Discussion

In this chapter, I will discuss the constraints that the new data presented in this work and obtained with modern methodologies place on the petrogenesis of the Ronda migmatites.

8.1 Constraints on the melting conditions and reactions

Compared with the conventional thermobarometry, an additional and likely more accurate estimate of the P-T conditions of melting in the metatexites is obtained by combining information from the pseudosections for the bulk rock (Fig. 5.9) and MI (Fig. 6.16). The combination of the two thermodynamic models provides an overlap of P-T fields (Fig. 8.1), indicating relatively low-T and low-P conditions for the anatexis (T=700-750 °C and P=4-5 kbar), in partial agreement with the conventional thermobarometry (Fig. 8.2). In addition, the lower limit of this temperature interval (~700 °C) is consistent with the temperature data obtained from the experimental re-homogenization of nanogranites and partially crystallized MI (Fig. 8.2).

A large proportion (~70%) of the analyzed MI in the metatexite show primary H_2O contents between 3 and 6 wt% (Fig. 6.15A), indicating an overall H_2O-undersaturated environment during melting in the metatexite at conditions of 700-750 °C and 4-5 kbar. In addition, the highest concentrations of H_2O measured in a few MI (~7-8 wt%, Fig. 6.15A) may indicate that at the very beginning partial melting was fluid-present, considering (i) the occurrence of CO_2 in MI (Fig. 6.10) and Gr in the rock, (ii) that graphite-saturated COH fluids at 4-5 kbar, 700-750°C are characterized by maximum X_{H_2O} ~0.80-0.85 (Connolly and Cesare, 1993) and iii) that the H_2O-saturation value for rhyolitic melts in equilibrium with H_2O-CO_2 fluids (with X_{H_2O} ~0.80) at 5 kbar is ~8 wt% (Tamic *et al.*, 2001).

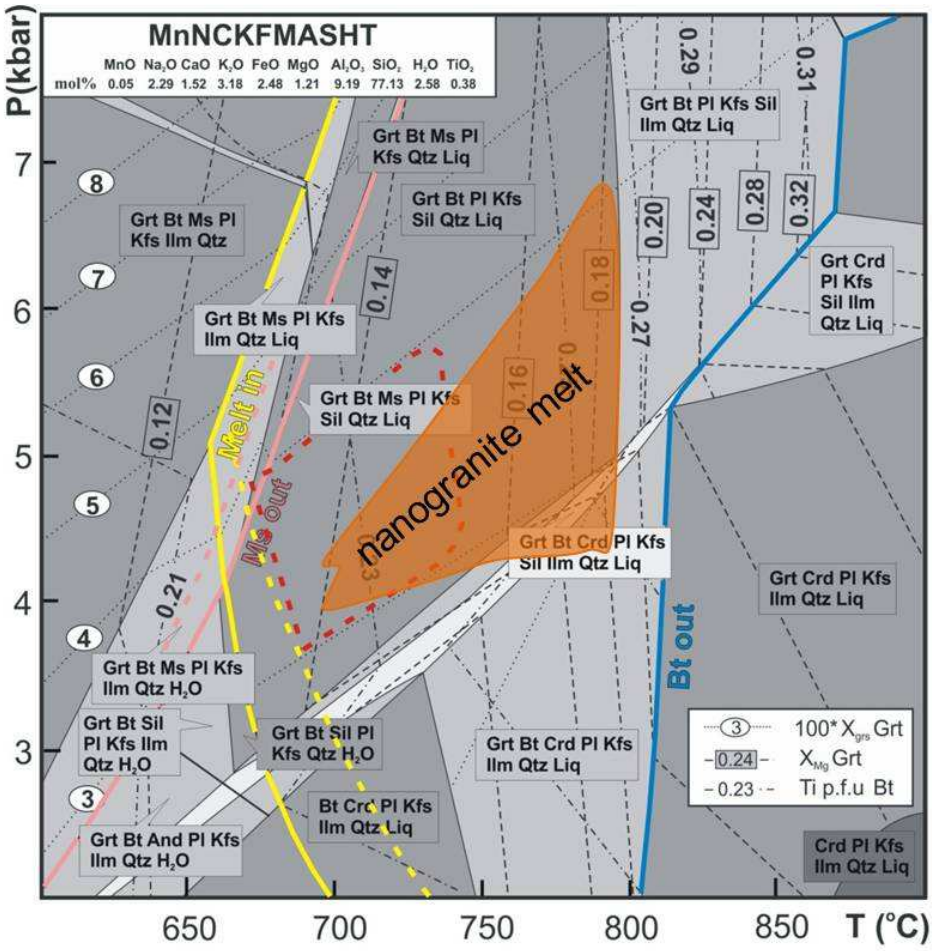

Figure 8.1: P-T pseudosection for the metatexite (Figure 5.9) with the addition of the field (labeled *nanogranite melt*) where the melt trapped in MI should be stable (see Figure 6.16 and discussion in Chapter 6).

Therefore, MI data along with petrographic observations (e.g., melt pseudomorphs in contact with biotite, plagioclase, quartz and garnet) favour the interpretation (b) proposed in Chapter 5, i.e. that most of the melt was produced by the continuous reaction (6) involving the Bt dehydration (Fig. 8.2). It is reasonable to envisage that under general H_2O-poor conditions, melting in the metatexite occurred initially and locally at the fluid-saturated solidus (reaction 1), owing to the presence of C-O-H fluids localized at the phase boundaries, and progressed by the continuous melting reaction (6). Regarding the role of Ms during anatexis, some microstructural observations (e.g., no melt pseudomorphs around the relict muscovite; see also Chapter 5) seem to reflect a prograde exhaustion of the muscovite before the fluid-saturated solidus (Fig. 8.2). Moreover, it should be taken into account that the solidus shift considered for $a_{H_2O}<1$ in

the fluid (see Chapter 5) is a minimum, because it was calculated for maximum X_{H_2O} values. Hence, the intersection of the fluid-saturated solidus and the muscovite-out curves (Figs. 8.1 and 8.2) may slightly move to higher pressure (P>5 kbar).
The melting reaction at the fluid-saturated solidus probably was:

$$Bt + Pl + Qtz + Kfs + fl \rightarrow melt \qquad (1')$$

The occurrence of MI at the core of the majority of garnets indicates that most of them started to grow above the solidus by the continuous reaction (6), right after the rock crossed the fluid-saturated solidus (reaction 1').

Pressure and temperature conditions in the mylonites are not well constrained as in the case of metatexites (Chapters 5 and 6). Nevertheless, the H_2O contents of the preserved glassy MI in the mylonite (up to 2.6 wt%; Fig. 6.15) along with the inferred P-T melting conditions (Fig. 8.2) indicate that anatexis in these rocks occurred under H_2O-undersaturated conditions by the continuous melting reaction (6), although part of the melt may have been initially generated by the Ms dehydration melting reaction (3).

Most of the primary H_2O contents (3-6 wt%) measured in the MI from metatexites differ to some extent from those predicted by experiments in the subaluminous granitic system. The liquidus curves determined for the granite system (Fig. 8.2) can be used to calculate the H_2O contents that are incorporated in granitic melts produced during the H_2O-undersaturated melting of quartzo-feldspathic rocks (Holtz *et al.*, 2001). At P-T conditions inferred for the melting in the metatexite and at H_2O-undersaturated conditions, these liquidus curves predict a H_2O content of ~6-7 wt% in the melts (Fig. 8.2). These discrepancies are probably due to some extent to the presence of excess Al_2O_3 in the natural systems that might modify the solidus and liquidus phase relationships along with the solubility curves, with respect to the subaluminous granitic system. Conversely, all the analyzed MI in the mylonite show much lower H_2O concentrations (1-2.6 wt%) than those predicted by Holtz *et al.* (2001) at the same P-T conditions (5-6 wt%). One explanation for these large differences may be that the melting temperature in the mylonites was higher than that inferred from the Ti-in-biotite geothermometer.

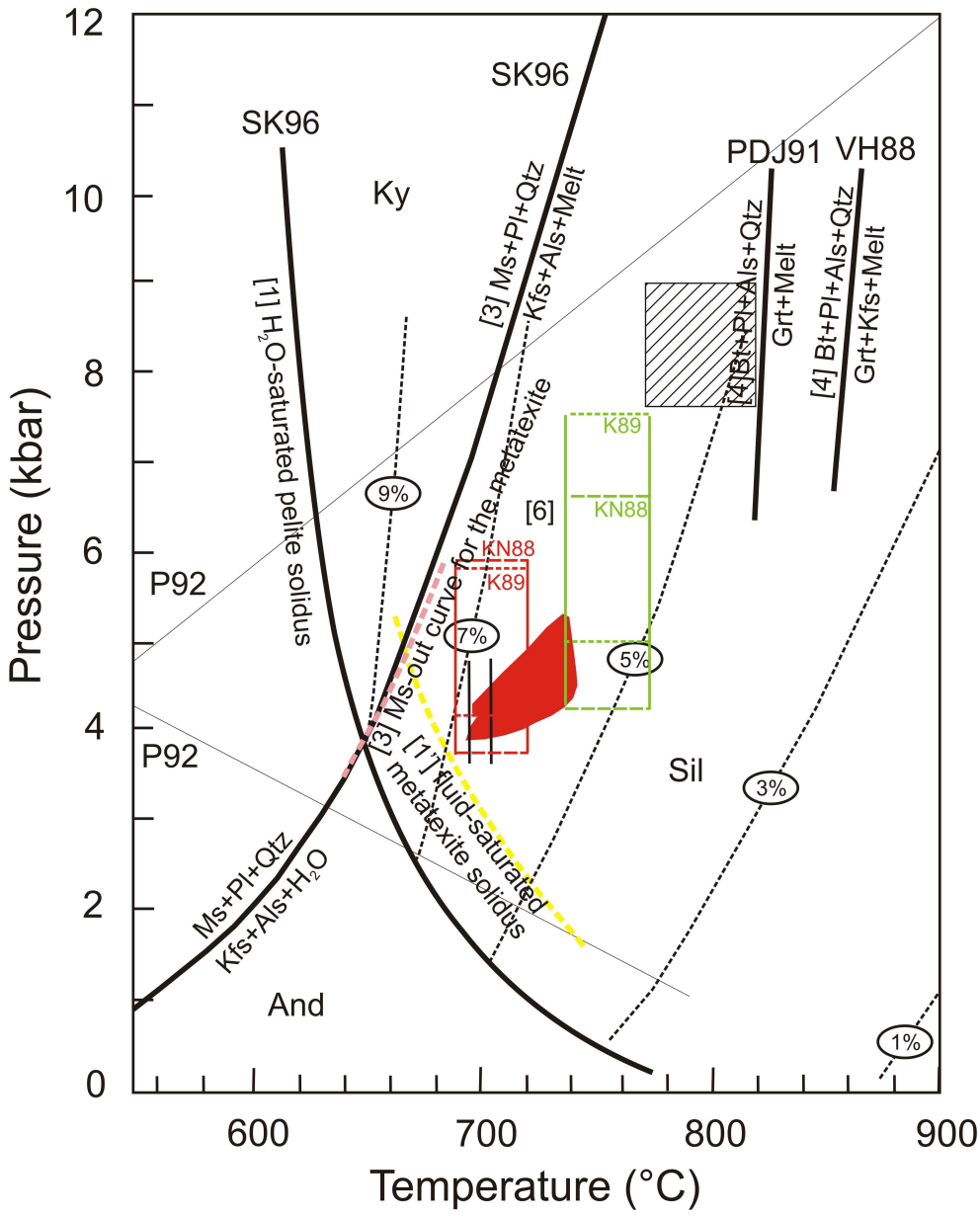

Figure 8.2: Petrogenetic grid showing the P-T conditions estimated for melting in the studied rocks and some melting reactions that metapelites and metagreywackes may cross upon heating. VH88 refers to Vielzeuf and Holloway (1988), PDJ91 to Patiño-Douce and Johnston (1991), P92 to Pattison (1992) and SK96 to Spear and Kohn (1996). Discontinuous reactions [1], [1'], [3] and [4], and continuous reaction [6] refer to those in the Chapters 5 and 8. Red area: melting conditions inferred for the metatexite from the combined models of Figure 8.1. Vertical solid lines are minimum and maximum thermometric estimates from Ti-in-biotite thermometer (see Chapter 5) for the prograde biotite in the metatexites (red) and mylonites (green). Vertical black lines indicate the minimum re-homogenization temperature (700±5 °C) for the nanogranites in the metatexite. Horizontal dashed lines are minimum and maximum pressure estimates for the metamorphic peak of the metatexites (red) and mylonites (green); KN88 refers to Koziol and Newton (1988), N89 to Koziol, (1989). Yellow and pink dashed curves as in Figure 5.9. Dashed square: peak conditions for the rutile-bearing mylonites outcropping at the contact with the peridotite (from Tubia *et al.*, 1997).The liquidus curves for the granitic eutectic or minimum melt composition at several H_2O concentrations (dotted black lines) are taken from Holtz *et al.* (2001).

Both the temperature and the pressure of equilibration of migmatites located underneath the peridotites increase towards the contact with the ultramafic rocks. Also, rutile-bearing mylonites located at the contact with the peridotites show P and T of equilibration higher than those of the studied mylonites (Fig. 8.2). Hence, migmatites and mylonites show an increase in the P and T of equilibration towards shallower levels of the crustal sequence (i.e., an inverted metamorphic sequence in T but also P) suggesting that metamorphism and partial melting were produced before the inversion of this sequence (i.e., when mylonites were at the bottom of the sequence).

8.2 Composition of the anatectic melts

The compositions of MI and leucosomes indicate that the inferred melting reactions produced peraluminous leucogranitic melts. An important point that needs to be addressed, however, is whether the melt trapped into MI is representative of the bulk anatectic melt in the system at the time of MI entrapment. The detailed studies on the geochemistry of MI in anatectic rocks are just at the beginning (Acosta-Vigil *et al.,* 2010; Cesare *et al.,* 2011; Ferrero *et al.,* 2012), and there is little information available on the significance of MI compositions yet. Acosta-Vigil *et al.* (2007 and 2010) reported the occurrence of disequilibrium phenomena in anatectic MI from El Hoyazo metapelitic enclaves, but also showed that i) disequilibrium affects only the concentrations of the trace elements compatible with respect to the mineral hosts, and ii) MI compositions do not represent exotic boundary layers but may correspond to composition of the bulk melt regarding the major elements and the incompatible trace elements. Likewise, the analyses of MI presented here correspond to regular leucogranitic compositions, similar to those of the analyzed glasses in the El Hoyazo anatectic enclaves or reported S-type leucogranites in the literature. Therefore, it is concluded that the major element compositions of MI presented in this study are likely to represent the bulk composition of the original anatectic melt at the time of MI entrapment.

Melt compositions during partial melting are potentially controlled by the kinetics of the interface reactions, the diffusive transport properties of the melt, and local equilibrium with neighbouring mineral phases (Brearley and Rubie, 1990; Acosta-Vigil *et al.*, 2006a and b). Phase dissolution experiments performed on haplogranitic melt at crustal anatectic conditions (Acosta-Vigil *et al.*, 2006b), showed that after a few days (~16) melt composition is controlled solely by component diffusion. Moreover, it has been experimentally shown (although at H_2O-saturated conditions) that diffusion-controlled anatexis of a quartzo-feldspathic protolith produces melts that form linear trends at relatively high angle with the cotectic line that separates the fields of Qtz and Or in a normative Qtz-Ab-Or diagram, due to the lower diffusivities of Si and Al than those of Na and K (Acosta-Vigil *et al.*, 2006a). Similar trends are defined by most of the analyzed MI in the metatexite and part of the MI in the mylonite, if I consider the compositions of MI trapped within the same garnet crystal (Fig. 8.3).

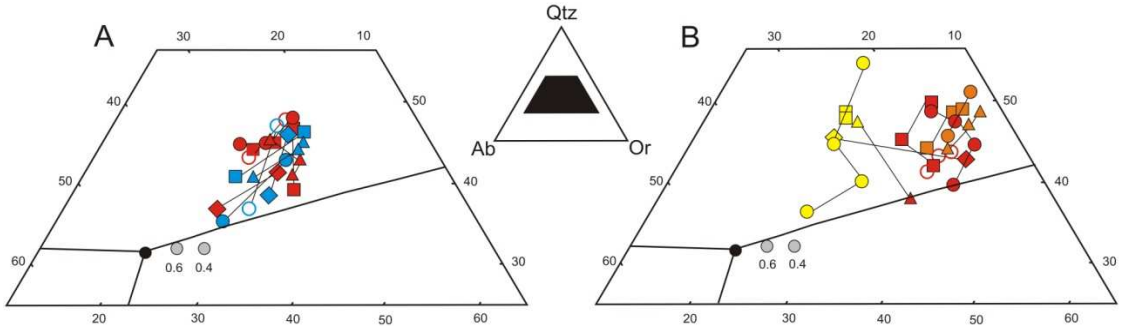

Figure 8.3: Normative CIPW compositions of MI from the metatexite (A) and mylonite (B). Light lines connect compositions of MI hosted in the same garnet. A) Red symbols: dry experiments; blue symbols: wet experiments. B) Yellow symbols: type II MI; red and orange symbols: type I MI. Black and grey symbols as in Figure 6.12.

This suggests that the composition of these melts at the time of MI entrapment was mainly controlled by the diffusion. This conclusion is in agreement with the time scale of the involved processes: the time interval between melt generation and its entrapment into growing peritectic phases has been estimated from tens of days to a few years (Acosta-Vigil *et al.*, 2010) and, therefore, the melt chemistry is likely to be mainly controlled by diffusion (see above). Preserved glassy MI in peritectic minerals from partially melted metapelitic enclaves (Cesare *et al.*, 2011) and regionally metamorphosed migmatitic granulites (Cesare *et al.*, 2009) show similar trends that are

at high angle to the cotectic line, suggesting that diffusion-controlled melting might be common during anatexis of the continental crust. Moreover, Holness *et al.* (2005) reported a diffusional control on the composition of melt films around the minerals of pyrometamorphic rocks. The spread of the MI data in the Qtz-Ab-Or diagram has two components. One component is parallel to the Qtz-feldspar direction, and has been explained as due to the control of melt composition by diffusion in the melt (see above). The other component is parallel the Ab-Or direction, and can be explained by the entrapment of melts at different times during the melting process (compare with Acosta-Vigil *et al.*, 2006a, see below). In fact, some of the studied MI trapped within the same garnet describe trends approximately parallel to the second component. Moreover, some scatter could be also due to local heterogeneities in the H_2O distribution that may affect diffusivities in the melt (Acosta-Vigil *et al.*, 2005). Key data for a better understanding of the extent of equilibrium and mechanisms of melting are represented by trace element concentrations in MI and the host minerals (e.g., Acosta-Vigil *et al.*, 2010). Unfortunately, these data are not yet available for the case of MI in the Ronda migmatites.

For the first time in the geologic literature, leucosomes and MI from the same migmatites have been analyzed and can be compared (Fig. 8.4). In the metatexite, two leucosomes have a peraluminous leucogranitic compositions and plot close to the Q-Or cotectic, suggesting that they may approach unmodified (i.e., primary) anatectic melts. A third leucosome, far from the cotectic line, likely represents a composition modified by accumulation or fractionation processes; this analysis corresponds to the outlier described in the Chapter 5 (Fig. 5.6). The composition of the only analyzed leucosome in the mylonite is very close to those of the metatexites, indicating again that it could represent a primary anatectic melt. There are two key observations when comparing MI and leucosomes. First, and in general, MI and leucosomes show different compositions. The compositions of MI are located along the Qtz-Or cotectic and spread towards the Qtz field. The compositions of leucosomes, however, are located at the Qtz-Or cotectic and far away from the eutectic. The second important observation is that the combination of both types of data (MI and leucosomes) show a very consistent pattern. The data concentrate in two areas: one is at the Qtz-Or cotectic but relatively close to

the H_2O-undersatruated eutectics (represented by MI in metatexites); the other is along the Qtz-Or cotectic as well, but further from the eutectic and towards the Qtz-Or side (represented by most MI in mylonites and analyzed leucosomes in metatexites and mylonites). Overall, this may indicate that although somewhat heterogeneous, MI can record the evolution of melt composition during the early stages of anatexis (see also Acosta-Vigil *et al.*, 2010), whereas leucosomes mostly reflect the composition of melt at, or closer to, the peak metamorphic conditions.

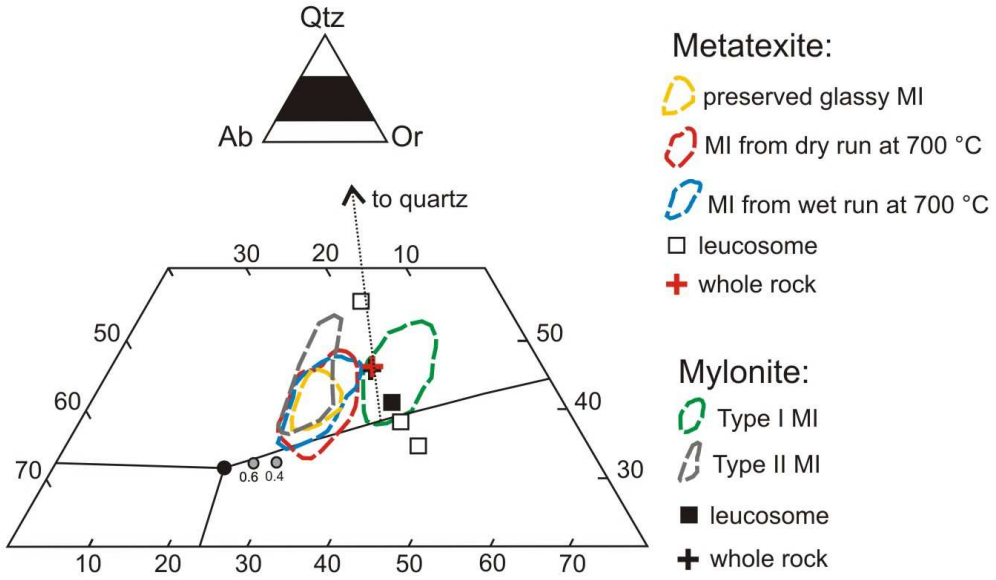

Figure 8.4: Normative compositions of the analyzed melts (MI and leucosomes) and whole migmatites, shown in the Qtz-Ab-Or diagram. Black arrow joins the whole rock compositions and the Qtz vertex. Black and grey symbols as in Figure 6.12.

The positive correlation between the normative orthoclase content of melts and the increasing temperature of formation can be explained by the progressive consumption of biotite with rising temperature that produces an increases in the K_2O content of the melt (Patiño-Douce and Johnston, 1991; Gardien *et al.*, 2000), but also by the evolution of melt composition predicted by the phase relationships in the haplogranite system (Fig. 8.4). Higher Na_2O/K_2O values in type II MI of the mylonite and in those of the metatexite may also reflect higher a_{H_2O} values at the onset of melting, because the increasing a_{H_2O} depresses the plagioclase + quartz solidus more strongly than it

depresses the stability of micas (Conrad *et al.*, 1988; Patiño-Douce and Harris, 1998), consuming plagioclase in greater proportion than biotite during melting.

In general, melt H_2O concentrations in MI are consistent with the increasing temperature of formation: MI from the metatexites, likely trapped at ~700 °C, show the highest amount of H_2O, whereas melts in the mylonite, generated at 750-770 °C, have lower H_2O contents. However, type I and type II MI in the mylonites have similar H_2O concentrations (see Chapter 6), despite the difference in composition and, supposedly, different temperature of formation.

Petrographic and geochemical data on leucogranitic dykes that intruded the overlying peridotites indicate high contents of volatiles for these anatectic melts (Acosta-Vigil *et al.*, 2001; Pereira *et al.*, 2003). During the study of the relationships between the leucogranites and the underlying Ronda migmatites, and to explain the coexistence of leucogranitic dykes enriched in B and leucosomes in migmatites depleted in B, Acosta-Vigil *et al.* (2001) suggested that B-rich aqueous fluids might have infiltrated through the shear-zone and have dissolved into the anatectic melt. Although the H_2O-present melting is often associated to crustal shear-zones (Brown, 2010), MI data strongly indicate H_2O-undersaturated conditions at the onset of melting in the mylonitic zone. Therefore, if migmatites and leucogranites are genetically related, the high concentrations of B in the latter cannot be explained by flux melting associated with B-rich fluids.

8.3 Viscosity of the anatectic melts

Viscosity is the most important physical property of anatectic melts that affects their segregation and ascent, crustal flow, and the tectonic processes within partially melted continental crust (Scaillet *et al.*, 1996; Petford *et al.*, 2000; Paterson *et al.*, 2001; Rosenberg and Handy, 2005). Using the analyzed major element compositions of MI, their H_2O concentrations (3.1-7.6 wt% in the metatexite and 1.0-2.6 wt% in the mylonite), the inferred maximum melting temperatures of 700 and 780°C in the migmatites, and the model proposed by Giordano *et al.* (2008), I have determined the viscosity of the melts trapped in MI. The anatectic melts produced in the earliest stages

of melting in the metatexite and mylonite have viscosities in the range $10^{4.8}$-$10^{7.1}$ and $10^{6.8}$-$10^{8.5}$ Pa·s, respectively. Such values are greater than those previously considered for granitic melts formed at the same P-T conditions under H_2O-undersaturated conditions (Holtz *et al.*, 2001; Nabelek *et al*., 2010). Overall, the viscosity of the melt produced at the onset of melting in the metatexite (T~700 °C) is about two or three orders of magnitude greater than the viscosity considered for the low-T granitic melts in models on melt segregation and on deformation of the partially melted crust ($10^{4.0}$-$10^{4.9}$ Pa·s; Scaillet *et al.*, 1996; Petford *et al.*, 2000; Paterson *et al.*, 2001). Hence, the study of MI is important also from the point of view of determining the strength of the partially melted crust and the time scale for melt extraction and ascent in anatectic areas. For instance, the data on MI at Ronda imply much greater rock strengths and much longer timescales for melt extraction and ascent, compared to the use of model melt compositions.

Chapter 9
Concluding remarks

The metasedimentary crust of the Ojen nappe, located below the Ronda peridotite slab, preserves evidence of partial melting at temperatures in the range ~700-800 °C. In the investigated quartzo-feldspathic migmatites the melting mainly occurred by the continuous reaction involving Bt dehydration, although towards the base of the crustal sequence melting likely started at the fluid-saturated solidus owing to the presence of H_2O-rich intergranular fluids. During the anatexis of these metasedimentary rocks, the growing peritectic garnet trapped droplets of melt (Fig. 9.1). Most of these MI are now partially to fully crystallized (nanogranites) and contain a granitic phase assemblage formed by quartz, feldspars and micas. The former presence of melt in the rocks is also recorded at the mesoscale by leucogranitic leucosomes and at the micro-scale by pseudomorphs after melt films (Fig. 9.1). Overall, crustal anatexis at Ronda produced peraluminous leuogranitic melts that are mainly H_2O-undersaturated, even at low melting degrees. The experimental re-homogenization and thermodynamic modelling on MI in peritectic garnet strongly confirm that the multivariant field Bt + Sil + Pl + Qtz + Grt + Kfs + melt starts at very low temperatures (≤700 °C) in the pressure range 3-6 kbar. Moreover, the pseudosections constructed employing the MI compositions may become an additional useful tool for the thermobarometry of anatectic rocks.

The present work, that represents the first combined study of melt inclusions and classical petrology on migmatites, shows that *in situ*, and otherwise impossible to retrieve, quantitative information on the earliest stages of crustal anatexis can be reliably gained from experimentally re-homogenized nanogranites and from preserved glassy melt inclusions in peritectic minerals from migmatites. Following the new experimental approach proposed in this study, the partially crystallized and nanogranite inclusions in peritectic garnets of migmatites from many orogenic belts worldwide (Chapter 1) can be successfully re-homogenized and then analyzed (i.e., we can now uncover the “message in the bottle”; see Clemens, 2009).

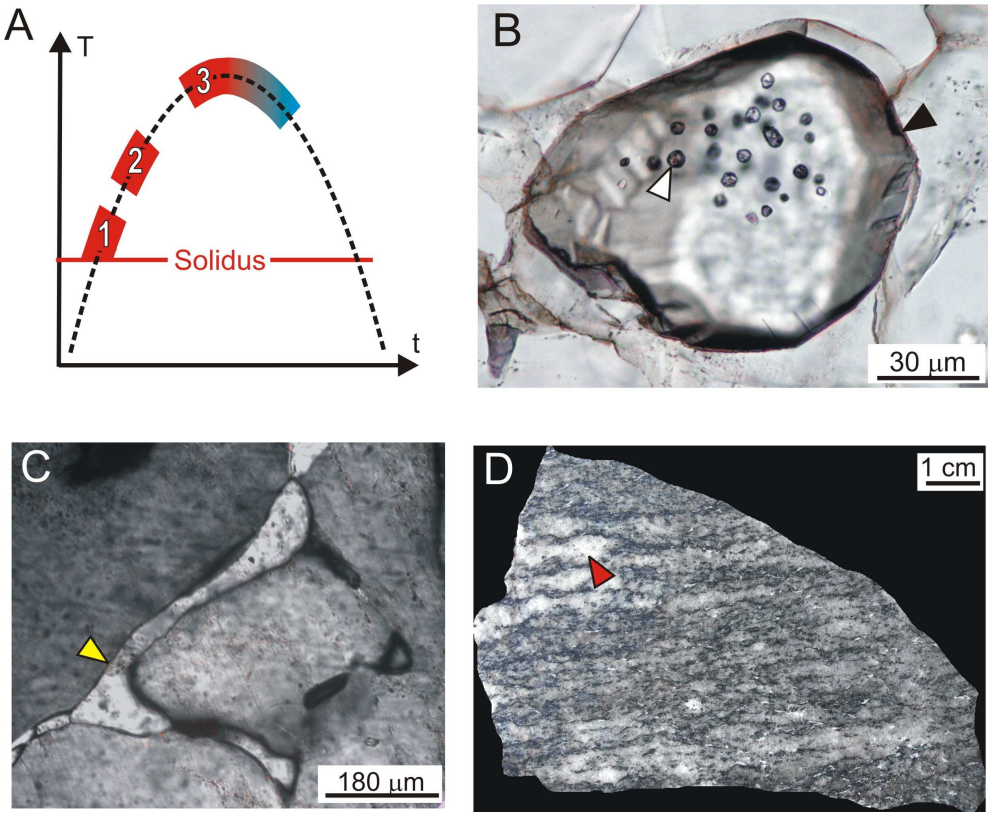

Figure 9.1: A) Schematic temperature (**T**) *vs.* time (**t**) model showing the main processes occurring during melt production (heating) and melt consumption (cooling) in the studied migmatites. B), C) and D) are images that refer to the metatexites. At, or soon after, the onset of melting (1), the growing peritectic garnet (B, black arrow) trapped droplets (B, white arrow) of anatectic melt produced by melting reaction. With the increase of temperature and melting degree (2), melt films (C, yellow arrow) formed along grain-boundaries. Then, melt migrated from grain-boundaries (3; see Brown *et al.*, 2011) and collected into leucosomes (D, red arrow). During the cooling path, many MI partially or totally crystallized and plagioclase pseudomorphs (C, yellow arrow) formed after grain-boundary melt film. Melt film pseudomorphism by single crystal is due to pore size barrier to nucleation (Holness and Sawyer, 2008) erasing any information on the original melt composition. Differentiation processes may modify the chemistry of some leucosomes during cooling. Although unmodified leucosomes may be present in the rock, they do not correspond to melts produced at the onset of melting. Note that this schematic T-t model is also suitable for regionally metamorphosed migmatites and granulites.

Hereafter, it will be possible to determine the fluid regime during initial stages of granite formation, rather than when the magma is separated from its source (see Clemens and Watkins, 2001), and the geochemical modelling on granite magmatism and continental crust differentation can now be constrained by directly measured natural primary melt compositions. The anatectic melts formed at low temperature (T≤750 °C) may not be so wet and flowing as previously considered. Hence, higher values for

viscosity of low-T granitic melts should be considered in models on melt segregation, but also on deformation of the partially melted crust, because the first melt fractions (< 7%; Rosenberg and Handy, 2005) deeply affect the weakening of the continental crust.

References

Acosta, A. (1998): Estudio de los fenómenos de fusión cortical y generación de granitoides asociados a las peridotitas de Ronda. Unpublished PhD thesis, Universidad de Granada, 305 pp.

Acosta-Vigil A., Buick I., Hermann J., Cesare B., Rubatto D., London D. and Morgan G.B. VI (2010): Mechanisms of crustal anatexis: a geochemical study of partially melted metapelitic enclaves and host dacite, SE Spain. Journal of Petrology, 51, 785-821.

Acosta-Vigil A., Cesare B., London D. and Morgan G.B. VI (2007): Microstructures and composition of melt inclusions in a crustal anatectic environment, represented by metapelitic enclaves within El Hoyazo dacites, SE Spain. Chemical Geology, 235, 450-465.

Acosta-Vigil A., London D. and Morgan G. B. VI (2005): Contrasting interactions of sodium and potassium with H_2O in haplogranitic liquids and glasses at 200 MPa from hydration-diffusion experiments. Contributions to Mineralogy and Petrology, 149, 276-287.

Acosta-Vigil A., London D. and Morgan G. B. VI (2006a): Experiments on the kinetics of partial melting of a leucogranite at 200 MPa H_2O and 690–800 °C: compositional variability of melts during the onset of H_2O-saturated crustal anatexis. Contributions to Mineralogy and Petrology, 151, 539-557.

Acosta-Vigil A., London D., Morgan G. B. VI and Dewers T. A. (2006b): Dissolution of quartz, albite, and orthoclase in H_2O-saturated haplogranitic melts at 800 °C and 200 MPa: diffusive transport properties of granitic melts at crustal anatectic conditions. Journal of Petrology, 47, 231-254.

Acosta-Vigil A., Pereira M. D., Shaw D. M. and London D. (2001): Contrasting behavior of boron during crustal anatexis. Lithos 56, 15-31.

Acosta-Vigil A., Rubatto D., Bartoli O., Meli S., Cesare B. and Azor, A. (2011): Dating crustal melting and high-grade metamorphism in the crustal rocks underlying the Ronda peridotites (Betic Cordilleras, S Spain). Seventh Hutton Symposium on Granites and Related Rocks, Abstracts Book, 2-3.

Anderson A.T., Davis A.M., Lu F. (2000): Evolution of Bishop Tuff rhyolitic magma based on melt and magnetite inclusions and zoned phenocrysts. Journal of Petrology, 41, 449-473

Baker D. R. (1998): Granitic melt viscosity and dike formation. Journal of Structural Geology, 20, 1395-1404.

Baker D. R. (2008). The fidelity of melt inclusions as records of melt composition. Contributions to Mineralogy and Petrology, 156, 377-395.

Becker A., Holtz F. and Johannes W. (1998): Liquidus temperatures and phase compositions in the system Qz-Ab-Or at 5 kbar and very low water activities. Contributions to Mineralogy and Petrology, 130, 213-224.

Behrens H. and Jantos N., (2001): The effect of anhydrous composition on water solubility in granitic melts. American Mineralogist, 86, 14-20.

Berry A. J., Danyushevsky L. D., O'Neill H. St C., Newville M. and Sutton S. R. (2008): Oxidation state of iron in komatiitic melt inclusions indicates hot Archaean mantle. Nature, 455, 960-963.

Bodnar R.J. and Student J.J. (2006): Melt inclusions in plutonic rocks: petrography and microthermometry. *in*, Webster, J.D., eds, Melt Inclusionsin Plutonic Rocks, Mineralogical Association of Canada, Montreal, Short Course 36, 1-26.

Brearley A. J. and Rubie D. C. (1990): Effects of H_2O on the disequilibrium breakdown of muscovite + quartz. Journal of Petrology, 31, 925-956.

Brown M. (2002): Prograde and retrograde processes in migmatites revisited. Journal of Metamorphic Geology, 20, 25-40.

Brown M. (2004): Melt extraction from lower continental crust. Transactions of the Royal Society of Edinburgh: Earth Sciences, 95, 35-48.

Brown M. (2007): Crustal melting and melt extraction, ascent and emplacement in orogens: mechanisms and consequences. Journal of the Geological Society, 164, 709-730.

Brown M. (2010): Melting of the continental crust during orogenesis: the thermal, rheological, and compositional consequences of melt transport from lower to upper continental crust. Canadian Journal of earth Sciences, 47, 655-694.

Brown M., Korhonen F. J. and Siddoway C. S. (2011): Organizing melt flow through the crust. Elements 7/4, 261-266.

Cenki B., Kriegsman L. M. and Braun I. (2002): Melt-producing and melt-consuming reactions in anatectic granulites: P–T evolution of the Achankovil cordierite gneisses, South India. Journal of Metamorphic Geology, 20, 543-561.

Cesare B. (2008): Crustal melting: working with enclaves. *in* Sawyer E.W. and Brown M., eds., Working with Migmatites. Mineralogical Association of Canada, Short Course 38, 37-55.

Cesare B., Acosta-Vigil A., Ferrero S. and Bartoli O. (2011): Melt inclusions in migmatites and granulites. *in* Forster M.A. and Fitz Gerald J. D., eds., Journal of the Virtual Explorer, 38, paper 2. Doi: 10.3809/jvir-tex.2011.00268.

Cesare B., Ferrero S., Salvioli-Mariani E., Pedron D. and Cavallo, A. (2009): Nanogranite and glassy inclusions: the anatectic melt in migmatites and granulites. Geology, 37, 627-630.

Cesare B., Maineri C., Baron Toaldo A., Pedron D. and Acosta-Vigil A. (2007): Immiscibility between carbonic fluids and granitic melts during crustal anatexis: a

fluid and melt inclusion study in the enclaves of the Neogene Volcanic Province of SE Spain. Chemical Geology, 237, 433-449.

Cesare B., Marchesi C., Hermann J. and Gomez-Pugnaire M. T. (2003): Primary melt inclusions in andalusite from anatectic graphitic metapelites: implications for the position of the Al_2SiO_5 triple point. Geology, 31, 573-576.

Cesare B., Salvioli Mariani E. and Venturelli G., (1997) Crustal anatexis and melt extraction during deformation in the restitic xenoliths at El Joyazo (SE Spain). Mineralogical Magazine, 61, 15–27.

Clemens J. D. (1990): The granulite-granite connexion *in* Vielzeuf D., and Vidal P., eds., Granulites and crustal differentiation: Dordrecht, Kluwer Academic Publishers, 25–36.

Clemens J. D. (2003): S-type granitic magmas-petrogenetic issues, models and evidence. Earth Science Reviews, 61, 1-18.

Clemens J. D. (2006): Melting of the continental crust: fluid regimes, melting reactions, and source-rock fertility, *in* Brown M., and Rushmer T., eds., Evolution and differentiation of the continental crust: Cambridge, UK, Cambridge University Press, 296–331.

Clemens J.D. (2009): The message in the bottle: ‘‘Melt’’ inclusions in migmatitic garnets. Geology, 37, 671-672.

Clemens J.D., Birch W. D. and Dudley R. A. (2011): S-type ignimbrites with polybaric crystallisation histories: the Tolmie Igneous Complex, Central Victoria, Australia. Contributions to Mineralogy and Petrology, 162, 1315-1337.

Clemens J. D. and Vielzeuf D. (1987): Constraints on melting and magma production in the crust. Earth and Planetary Science Letters, 86, 287-306.

Clemens J. D. and Watkins J. M. (2001): The fluid regime of high-temperature metamorphism during granitoid magma genesis. Contributions to Mineralogy and Petrology, 140, 600-606.

Collins W.J. and Hobbs B.E. (2001): What caused the Early Silurian change from mafic to silicic (S-type) magmatism in the eastern Lachlan fold belt? Australian Journal of Earth Sciences, 47, 25-41.

Connolly J. A. D. (1990): Multivariable phase diagrams: an algorithm based on generalized thermodynamics. American Journal of Science, 290, 666–718.

Connolly J.A.D. (2009): The geodynamic equation of state: what and how. Geochemistry, Geophysics, Geosystems, 10, Q10014.

Connolly J. A. D. and Cesare, B. (1993). C-O-H-S fluid composition and oxygen fugacity in graphitic metapelites. Journal of Metamorphic Geology 11, 379-388.

Coggon R. and Holland T. J. B. (2002): Mixing properties of phengitic micas and revised garnet-phengite thermobarometers. Journal of Metamorphic Geology, 20, 683-696.

Conrad W. K., Nicholls I. A. and Wall V. J. (1988): Water-saturated and -undersaturated melting of metaluminous and peraluminous crustal compositions at 10 kb: evidence for the origin of silicic magmas in the Taupo Volcanic Zone, New Zealand, and other occurrences. Journal of Petrology 29, 765-803.

Corona-Chávez P., Poli S. and Bigioggero B. (2006): Syn-deformational migmatites and magmatic-arc metamorphism in the Xolapa Complex, southern Mexico. Journal of Metamorphic Geology, 24, 169-191.

Cuevas J., Esteban J.J. and Tubía, J.M. (2006): Tectonic implications of the granite dyke swarm in the Ronda peridotites (Betic Cordilleras, Southern Spain). Journal of the Geological Society, 163, 631-640.

Danyushevsky L. V., McNeill A. W. and Sobolev A. V. (2002): Experimental and petrological studies of melt inclusions in phenocrysts from mantle-derived magmas: an overview of techniques, advantages and complications. Chemical Geology 183, 5-24.

Devineau K, Pichavant M and Villiéras F (2005): Melting kinetics of granite powder aggregates at 1175 °C, 1 atm. European Journal Mineralogy, 17, 387-398.

Dewey J.F., Helmann M.L., Turco E., Hutton D.H.W. and Knott S.D. (1989): Kinematics of the western Mediterranean. *In* Coward M.P., Dietrich, D. and Park, R.G., eds., Alpine Tectonics. Special Publications, vol. 45. Geological Society, London, 265-283.

Di Martino C., Forni F., Frezzotti M.L., Palmeri R., Webster J. D., Ayuso R. A., Lucchi F. and Tranne C. A. (2011): Formation of cordierite-bearing lavas during anatexis in the lower crust beneath Lipari Island (Aeolian arc, Italy). Contributions to Mineralogy and Petrology, 162, 1011-1030.

Di Vincenzo G., Andriessen P. A. M. and Ghezzo C. (1996): Evidence of Two Different Components in a Hercynian Peraluminous Cordierite-bearing Granite: the San Basilio Intrusion (Central Sardinia, Italy). Journal of Petrology, 37/5, 1175-1206.

Ebadi A. and Johannes W. (1991): Beginning of melting and composition of first melts in the system Qz-Ab-Or-H_2O-CO_2.Contributions to Mineralogy and Petrology, 106, 286-295.

Esteban J.J., Cuevas J., Tubia J.M., Sergeev S. and Larionov A. (2011): A revised Aquitanian age for the emplacement of Ronda peridotites (Betic Cordilleras, southern Spain). Geological Magazine, 148, 183-187.

Emmanuel S., Ague J.J. and Walderhaug O. (2010): Interfacial energy effects and the evolution of pore size distributions during quartz precipitation in sandstone. Geochimica et Cosmochimica Acta, 74, 3539-3552.

Fall A., Tattitch B. and Bodnar R.J. (2011): Combined microthermometric and Raman spectroscopic technique to determine the salinity of H2O–CO2–NaCl fluid inclusions based on clathrate melting. Geochimica et Cosmochimica Acta 75 (4), 951-964.

Fedele L., Bodnar R.J., DeVivo B. and Tracy R. (2003): Melt inclusion geochemistry and computer modeling of trachyte petrogenesis at Ponza, Italy. Chemical Geology., 194, 81-104

Ferrero S., Bartoli O., Cesare B., Salvioli-Mariani E., Acosta-Vigil A., Cavallo A., Groppo C., Battiston S. (2012): Microstructures of melt inclusions in anatectic metasedimentary rocks. Journal of Metamorphic Geology. doi:10.1111/j.1525-1314.2011.00968.x

Ferrero S., Bodnar R. J. Cesare B. and Viti C. (2011): Re-equilibration of primary fluid inclusions in peritectic garnet from metapelitic enclaves, El Hoyazo, Spain. Lithos, 124, 117-131.

Ferry J. M. and Spear F. S. (1978): Experimental calibration of the partitioning of Fe and Mg between biotite and garnet. Contributions to Mineralogy and Petrololy, 66, 113-117.

Fogel R.A. and Rutherford M. J. (1990): The solubility of carbon dioxide in rhyolitic melts: a quantitative FTIR study. American Mineralogist, 75, 1311-1326.

Frezzotti M.L. (1992): Magmatic immiscibility and fluid phase evolution in the Mount Genis granite (southeastern Sardinia, Italy). Geochimical and Cosmochimical Acta, 56, 21-33.

Frezzotti M.L. (2001): Silicate melt inclusions in magmatic rocks: applications to petrology. Lithos, 55, 273-299.

García-Casco A., Torres-Roldán R.L., Millán G., Monié P. and Haissen, F. (2001): High-grade metamorphism and hydrous melting of metapelites in the Pinos terrane (W. Cuba): Evidence for crustal thickening and extension in the northern Caribbean collisional belt. Journal of Metamorphic Geology, 19, 699-715.

Gardien V., Thompson A. B., Grujic D. and Ulmer P. (1995): Experimental melting of biotite + plagioclase + quartz ± muscovite assemblage and implications for crustal melting. Journal of Geophysical Research, 100/B8, 15581-15591.

Gardien V., Thompson A. B. and Ulmer P. (2000): Melting of biotite + plagioclase + quartz gneisses: the role of H_2O in the stability of amphibole. Journal of Petrology, 41/5, 651-666.

Giordano D., Russell J. K. and Dingwell D. B. (2008): Viscosity of magmatic liquids: a model. Earth and Planetary Science Letters 271, 123-134.

Groppo C., Rolfo F. and Lombardo B. (2009): P–T evolution across the Main Central Thrust Zone (eastern Nepal): hidden discontinuities revealed by petrology. Journal of Petrology, 50, 1149-1180.

Groppo C., Rubatto D., Rolfo F. and Lombardo B. (2010): Early Oligocene partial melting in the Mian Central Thrust Zone (Arun valley, eastern Nepal Himalaya). Lithos, 118, 287-301.

Guernina S. and Sawyer E. W. (2003): Large-scale melt-depletion in granulite terranes: an example from the Archean Ashuanipi Subprovince of Quebec. Journal of Metamorphic Geology, 21, 181-201.

Guidotti C. V., Cheney J. T. and Guggenheim S. (1977): Distribution of titanium between coexisting muscovite and biotite in pelitic schists from northwestern Maine. American Mineralogist, 62, 438-448.

Hacker R., Kelemen P. B. and Behn M. D. (2011): Differentiation of the continental crust by relamination. Earth and Planetary Science Letters, 307, 501-516.

Hawkesworth C. J. and Kemp A. I. S. (2006): Evolution of the continental crust. Nature, 443/19, 811-817.

Henriquez J.L. and Darling R.S. (2009): Zircon-clinging inferred anatectic melt inclusions in Adirondack Garnet. Northeastern Section (45th Annual) and Southeastern Section (59th Annual) Joint Meeting, (abstract).

Henry D. J., Guidotti C. V., and Thomson J.A. (2005): The Ti-saturation surface for low-to-medium pressure metapelitic biotite: Implications for Geothermometry and Ti-substitution Mechanisms. American Mineralogist, 90, 316-328.

Hess K-U. and Dingwell D.B. (1996): Viscosities of hydrous leucogranitic melts: a non-Arrhenian model. American Mineralogist, 81, 1297-1300.

Holland T. J. B. and Powell R. (1998): An internally consistent thermodynamic data set for phases of petrologic interest. Journal of Metamorphic Geology, 16, 309-343.

Holland T. J. B. and Powell R. (2001): Calculation of phase relations involving haplogranitic melts using an internally consistent thermodynamic dataset. Journal of Petrology, 42, 673-683.

Holland T. J. B. and Powell R. (2003): Activity-composition relations for phases in petrological calculations: an asymmetric multicomponent formulation. Contributions to Mineralogy and Petrology, 145, 492-501.

Holness M. B., Cesare B. and Sawyer E.W. (2011): Melted rocks under the microscope: microstructures and their interpretation. Elements, 7/4, 245–250.

Holness M.B., Dane K., Sides R., Richardson C. and Caddick M. (2005): Melting and melt segregation in the aureole of the Glenmore Plug, Ardnamurchan. Journal of Metamorphic Geology, 23:29-43.

Holness M. B. and Sawyer E.W. (2008): On the pseudomorphing of melt-filled pores during the crystallization of migmatites. Journal of Petrology, 49, 1343-1363.

Holtz F. and Johannes W. (1991): Genesis of peraluminous granites I. Experimental investigations of melt compositions at 3 and 5 kb and various H_2O activities. Journal of Petrology, 32, 935-958.

Holtz F., Johannes W., Tamic N. and Behrens H. (2001): Maximum and minimum water contents of granitic melts generated in the crust: a reevaluation and implications. Lithos, 56, 1-14.

Icenhower J and London D. (1995): An experimental study of element partitioning among biotite, muscovite and coexisting peraluminou silicic melt at 200 MPa (H_2O). American Mineralogist, 80, 1229-1251.

Indares A., White R.W. and Powell, R. (2008): Phase equilibria modeling of kyanite bearing anatectic paragneiss from the central Grenville Province. Journal of Metamorphic Geology 26, 815-836.

Jamieson R. A., Unsworth M. J., Harris N. B. W., Rosenberg C. L. and Schulmann K. (2011): Crustal melting and the flow of mountains. Elements, 7/4, 253-260.

Johannes W. and Holtz, F., (1996): Petrogenesis and experimental petrology of granitic rocks: Berlin, Springer, 335 p.

Johnson T.E., Hudson N.F.C. and Droop G.T.R. (2001): Partial melting in the Inzie haed gneisses: The role of water and a petrogenetic grid in KFMASH applicable to anatectic pelitic migmatites. Journal of Metamorphic Geology, 19, 99-108.

Kohn M.J. and Spear F. (2000): Retrograde net transfer reaction insurance for pressure-temperature estimates. Geology, 28, 1127-1130.

Koziol A. M. (1989): Recalibration of the garnet–plagioclase–Al2SiO5–quartz (GASP) geobarometer and applications to natural parageneses. EOS Trans. American Geophysical Union, 70, 493.

Koziol A. M. and Newton R. C. (1988): Redetermination of the anorthite breakdown reaction and improvement of the plagioclase-garnet-Al2SiO5-quartz barometer. American Mineralogist, 73, 216-223.

Kretz R. (1983): Symbols for rock-forming minerals. American Mineralogist, 68, 277-279.

Kriegsman L. M. (2001): Partial melting, partial melt extraction and partial back reaction in anatectic migmatites. Lithos 56, 75-96.

Kühn A., Stüwe K. and Trouw R. A. J. (2004): Metamorphic evolution of the Ribeira Belt: evidence from outcrops in the Rio de Janeiro area, Brazil. Journal of Petrology, 45/11, 2303-2323.

Lavaure S. and Sawyer E.W. (2011): Source of biotite in the Wuluma Pluton: replacement of ferromagnesian phases and disaggregation of enclaves and schlieren. Lithos, 125, 757–780.

Le Breton N. and Thompson A. B. (1988): Fluid-absent (dehydration) melting of biotite in metapelites in the early stages of crustal anatexis. Contributions to Mineralogy and Petrology, 99, 226-237.

Loomis T.P. (1972): Contact Metamorphism of pelitic rock by the Ronda Ultramafic intrusion, Southern Spain. Geological Society of America Bulletin 83, 2449-2473.

Lowenstern J. (1995): Applications of silicate-melt inclusions to the study of magmatic volatiles. i*n* Thompson, J.F.H., eds., Magmas, Fluids and Ore Deposits, Mineralogical Association of Canada, Victoria, Short Course, 23, 71-99.

Manning C.E. (1994): The solubility of quartz in H_2O in the lower crust and upper mantle. Geochimica et Cosmochimica Acta, 58, 4831-4839.

Marchildon, N. and Brown, M., (2002): Grain-scale melt distribution in two contact aureole rocks:implications for controls on melt localization and deformation. Journal of Metamorphic Geology, 20,381-396.

Maze W.B., Bergman S.C. and Sisson V.B. (1981): Direct observations of the formation of fluid primary inclusions. Geological Society of America, 13, 506.

Métrich N. and Wallace P.J. (2008): Volatile abundances in basaltic magmas and their degassing paths tracked by melt inclusions. *in* Putirka K.D. and Tepley F.J., Minerals, Inclusions and Volcanic Processes. Reviews in Mineralogy and Geochemystry, 69, 363-402.

Montel J. M. and Vielzeuf D. (1997): Partial melting of metagreywackes, Part II. Compositions of minerals and melts. Contributions to Mineralogy and Petrology,128, 176-196.

Moore G. (2008): Interpreting H_2O and CO_2 contents in melt inclusions; constraints from solubility experiments and modeling. *In* Putirka K. D. and Tepley F. J., III eds., Minerals, Inclusions and Volcanic Processes. Mineralogical Society of America and Geochemical Society, Reviews in Mineralogy and Geochemistry 69, 333-362.

Morgan G.B. and London D. (1996): Optimizing the electron microprobe analysis of hydrous alkali aluminosilicate glasses. American Mineralogist, 81, 1176-1185.

Morgan G.B. and London D. (2005): Effect of current density on the electron microprobe analysis of alkali aluminosilicate glasses. American Mineralogist, 90, 1131-1138.

Müller A., Thomas R., Wiedenbeck M., Seltmann R. and Breiter K. (2006): Water content of granitic melts from Cornwall and Erzgebirge: a Raman spectroscopy study of melt inclusions. European Journal of Mineralogy, 18, 429-440.

Nabelek P.I., Whittington A.G. and Sirbescu M-L C. (2010): The role of H_2O in rapid emplacement and crystallization of granite pegmatites: resolving the paradox of large crystals in highly undercooled melts. Contributions to Mineralogy and Petrology, 160, 313-325.

Navarro-Vilá F. and Tubía J.M. (1983): Essai d'une nouvelle differentiation des Nappes Alpujarrides dans le secteur occidental des Cordille`res Be´tiques (Andalousie, Espagne). Comptes Rendues de l'Acade´mie des Sciences, 296, 111-114.

Newton R. C., Charlu T. V. and Kleppa O. J., (1980): Thermochemistry of high structural state plagioclases. Geochimica et Cosmochimica Acta, 44, 933-941.

Obata M. (1980): The Ronda peridotite: garnet-, spinel-, and plagioclase lherzolite facies and the P-T trajectories of a high temperature mantle intrusion. Journal of Petrology, 21, 533-572.

Paterson M. S. (2001): A granular flow theory for the deformation of partially molten rock. Tectonophysics 335, 51-61.

Patiño Douce A. E. and Beard J. S. (1995): Dehydration-melting of biotite gneiss and quartz amphibolites from 3 to 15 kbar. Journal of Petrology, 36/3, 707-738.

Patiño Douce A. E. and Harris N. (1998): Experimental constraints on Himalayan anatexis. Journal of Petrology, 39/4, 689-710.

Patiño Douce A. E. and Johnston A. D. (1991): Phase equilibria and melt productivity in the politic system: implications for the origin of peraluminous granitoids and aluminous granulites. Contributions to Mineralogy and Petrology, 107, 202-218.

Patiño Douce A. E., Johnston A. D. and Rice, J.M. (1993): Octahedral excess mixing properties in biotite; a working model with applications to geobarometry and geothermometry. American Mineralogist, 78, 113-131.

Pattison D. R. M. (1992): Stability of andalusite and sillimanite and the Al_2SiO_5 triple point, constraints from the Ballachulish aureole, Scotland. Journal of Geology 100, 423-446.

Pattison D. R. M. and Tinkham D. K. (2009): Interplay between equilibrium and kinetics in prograde metamorphism of pelites: an example from the Nelson aureole, British Columbia. Journal of Metamorphic Geology, 27, 249-279.

Petford N., Cruden A. R., McCaffrey K. J. W. and Vigneresse J.-L. (2000): Granite magma formation, transport and emplacement in the Earth's crust. Nature 408, 669-673.

Perchuk L. L., and Lavrent'eva I. V. (1983): Experimental investigation of exchange equilibria in the system cordierite–garnet–biotite. *in* Saxena, S.K., eds., Kinetics and Equilibrium in Mineral Reactions, APG Series, Springer, 199-240.

Pereira M. D., Shaw D. and Acosta-Vigil A. (2003): Mobile trace elements and fluid-dominated processes in the Ronda peridotite, southern Spain. The Canadian Mineralogist, 41, 617-625.

Peto P. (1976): An experimental investigation of melting relationships involving muscovite and paragonite in the silica-saturated portion of the system K_2O-Na_2O-Al_2O_3-SiO_2-H_2O to 15 kbar total pressure. In: Progress in Experimental Petrology, 3rd Report. London: NERC, pp. 41-45.

Pickering J. M. and Johnston A. D. (1998): Fluid-absent melting behavior of a two-mica metapleite: experimental constraints on the origin of Black Hills granite. Journal of Petrology, 39/10, 1787-1804.

Platt J.P, Argles T. W., Carter A., Kelley S. P., Whitehouse M. J. and Lonergan L. (2003): Exhumation of the Ronda peridotite and its crustal envelope: constraints from thermal modelling of a P–T–time array. Journal of the Geological Society, 160, 655-676.

Platt J.P. and Whitehouse M.J. (1999): Early Miocene high-temperature metamorphism and rapid exhumation in the Betic Cordillera (Spain): Evidence from U-Pb zircon ages. Earth and Planetary Science Letters, 171, 591-605.

Powell R. and Holland T.J.B. (1999). Relating formulations of the thermodynamics of mineral solid solutions; activity modeling of pyroxenes, amphiboles and micas. American Mineralogist, 84, 1-14.

Powell R. and Holland T. (2010): Using equilibrium thermodynamics to understand metamorphism and metamorphic rocks. Elements, 6, 309-314.

Priem H.N.A., Boelrijk N.A.I.M., Hebeda E.H., Oen I.S., Verdurmen E.A.T. and Verschure, R.H. (1979): Isotopic dating of the emplacement of the ultramafic masses in the Serranía de Ronda, Southern Spain. Contributions to Mineralogy and Petrology, 70, 103-109.

Putnis A., Prieto M. and Fernandez-Diaz L. (1995): Fluid supersaturation and crystallization in porous media. Geological Magazine, 132, 1-13.

Roedder E. (1984): Fluid inclusions. Mineralogical Society of America, Reviews in Mineralogy, 12, 644 pp.

Rosenberg C. L. and Handy M. R. (2005): Experimental deformation of partially melted granite revisited: implications for the continental crust. Journal of Metamorphic Geology, 23, 19-28.

Salvioli-Mariani E., Mattioli M., Renzulli A. and Serri G. (2002): Silicate melt inclusions in the cumulate minerals of gabbroic nodules from Stromboli Volcano (Aeolian Islands, Italy): main components of the fluid phase and crystallization temperatures. Mineralogical Magazine, 66 (6), 969-984.

Sánchez-Rodríguez, L. (1998): Pre-Alpine and Alpine evolution of the Ronda Ultramafic Complex and its country-rocks (Betic chain, southern Spain): U–Pb SHRIMP zircon and fission-track dating. Published PhD Thesis, ETH Zürich, 170p.

Sawyer E. W. (2008): Atlas of migmatites: Quebec, Mineralogical Association of Canada, The Canadian Mineralogist Special Publication 9, 386 p.

Sawyer E. W. (2010): Migmatites formed by water-fluxed partial melting of a leucogranodiorite protolith: microstructures in the residual rocks and source of the fluid. Lithos, 116, 273-286.

Sawyer E. W., Cesare B. and Brown M. (2011): When the continental crust melts. Elements, 7/4, 229-233.

Scaillet B., Holtz F., Pichavant M. and M. Schmidt (1996): Viscosity of Himalayan leucogranites: implications for mechanisms of granitic magma ascent. Journal of Geophysical Research, 101/B12, 27691-27699.

Severs M. J., Azbej T., Thomas J. B., Mandeville C. W. and Bodnar R. J. (2007): Experimental determination of H_2O loss from melt inclusions during laboratory heating: Evidence from Raman spectroscopy. Chemical Geology, 237, 358-371.

Shabeer K.P., Satish-Kumar M., Armstrong R. and Buick I.S. (2005): Constraints on the timing of Pan-African granulite-facies metamorphism in the Kerala Khondalite

Belt of southern India: SHRIMP mineral ages and Nd isotopic systematics. Journal of Geology, 113, 95-106.

Sisson V.B., Lovelace R.B., Maze W.B. and Bergman, S.C. (1993): Direct observation of primary fluid inclusion formation. Geology, 21, 751-754.

Skirius C.M., Peterson J.W. and Anderson A.T. (1990): Homogenizing rhyolitic glass inclusions from the Bishop Tuff. American Mineralogist, 75, 1381-1398

Sobolev A.V., Hofmann A.W., Jochum K.P., Kuzmin D.V. and Stoll B. (2011): A young source for the Hawaiian plume. Nature, 476, 434-437.

Solar G. S. and Brown M. (2001): Petrogenesis of migmatites in Maine, USA: possible source of peraluminous leucogranite in plutons? Journal of Petrology, 42/4, 789-823.

Soto J.I. and Platt J.P. (1999): Petrological and structural evolution of highgrade metamorphic rocks from the floor of the Alboran Sea basin, western Mediterranean: Journal of Petrology, 40, 21–60.

Spear F. and Kohn M. J. (1996): Trace element zoning in garnet as a monitor of crustal melting. Geology, 24/12, 1099-1102.

Spear F., Kohn M. J. and Cheney J. T. (1999): *P-T* paths from anatectic pelites. Contributions to Mineralogy and Petrology, 134, 17-32.

Stevens G., Clemens J. D. and Droop G. T. R. (1997): Melt production during granulite-facies anatexis: experimental data from “primitive” metasedimentary protoliths. Contributions to Mineralogy and Petrology, 128, 352-370.

Stevens G., Villaros A. and Moyen J.F. (2007) Selective peritectic garnet entrainment as the origin of geochemical diversity in S-type granites. Geology, 35, 9-12.

Student J.J. and Bodnar R.J. (1999): Synthetic Fluid Inclusions XIV: Coexisting Silicate Melt and Aqueous Fluid Inclusions in the Haplogranite–H2O–NaCl–KCl System. Journal of Petrology, 40, 1509-1525.

Student J.J. and Bodnar R.J. (2004): Silicate melt inclusions in porphyry copper deposits: identification and homogenization behavior. Canadian Mineralogist, 42, 1583-1599

Tajčmanová L. Connolly J.A.D. and Cesare, B., (2009): A thermodynamic model for titanium and ferric iron solution in biotite. Journal of Metamorphic Geology, 27, 153-165.

Tajčmanová L., Konopásek J. and Schulmann K. (2006): Thermal evolution of the orogenic lower crust during exhumation within a thickened Moldanubian root of the Variscan belt of Central Europe. Journal of Metamorphic Geology, 24, 119-134.

Tamic N., Behrens H. and Holtz F. (2001): The solubility of H_2O and CO_2 in rhyolitic melts in equilibrium with a mixed CO_2-H_2O fluid phase. Chemical Geology, 174, 333-347.

Thomas R. (2000): Determination of water contents of granite melt inclusions by confocal Raman microprobe spectroscopy. American Mineralogist, 85, 868-872.

Thomas J.B., Bodnar R.J., Shimizu N. and Chesner C.A. (2003): Melt Inclusions in Zircon. Reviews in Mineralogy and Geochemistry, 53, 63-87.

Thomas R., Kamenetsky D. and Davidson, P. (2006): Laser Raman spectroscopic measurements of the water in unexposed glass inclusions. American Mineralogist, 91, 467-470.

Thompson A. B. (1982): Dehydration melting of pelitic rocks and the generation of H2O-undersaturated granitic liquids. American Journal of Science, 282, 1567-1595.

Thompson, J. B. and Hovis, G. L. (1979) Entropy of mixing in Sanidine. American Mineralogist, 64, 57–65.

Tinkham, D.K., Zuluaga, C.A. and Stowell, H.H. (2001): Metapelite phase equilibria modeling in MnNCKFMASH: The effect of variable Al2O3 and MgO/(MgO + FeO) on mineral stability. Geological Materials Research, 3, 1-42.

Tracy R. J., (1982): Compositional zoning and inclusions in metamorphic minerals. *in* Ferry, J. M., eds., Characterization of metamorphism through mineral equilibria, Reviews in Mineralogy, 10, Mineralogical Society of America, Washington D.C., 355-397.

Tubıá, J.M. (1988): Estructura de los Alpuja´rrides occidentales: cinema´tica y condiciones de emplazamiento de las peridotitas de Ronda. Publicaciones especiales del Boletı´n Geolo´gico y Minero 99, 1-124.

Tubıá, J.M. and Cuevas J., (1986): High-temperature emplacement of the Los Reales peridotite nappe (Betic Cordillera, Spain). Journal of Structural Geology 8, 473-482.

Tubía J. M., Cuevas J. and Gil-Ibarguchi J.I. (1997): Sequential development of the metamorphic aureole beneath the Ronda peridotites and its bearing on the tectonic evolution of the Betic Cordillera. Tectonophysics, 279, 227–-52.

Tubía, J.M. and Gil Ibarguchi J.I. (1991): Eclogites of the Ojen nappe: a record of subduction in the Alpujarride complex (Betic Cordilleras, southern Spain). Journal of the Geological Society, London 148, 801-804.

Vanderhaeghe O. (2001): Melt segregation, pervasive melt migration and magma mobility in the continental crust: The structural record from pores to orogens: Physics and Chemistry of the Earth, Part A: Solid Earth and Geodesy, 26, 213-223.

Vernon R.H. (2011): Microstructures of melt-bearing regional metamorphic rocks. *in* Van Reenen D.D., Kramers J.D., McCourt S. and Perchuk L.L., eds., Origin and Evolution of Precambrian High-Grade Gneiss Terranes, with Special Emphasis on the Limpopo Complex of Southern Africa, Geological Society of America Memoir, 207, 1-11.

Vielzeuf D., Baronnet A., Perchuk A. L., Laporte D. and Baker M. B. (2007): Calcium diffusivity in alumino-silicate garnets: an experimental and ATEM study. Contributions to Mineralogy and Petrology, 154, 153-170.

Vielzeuf D., Clemens J.C., Pin C., and Moinet, E. (1990) Granites, granulites and crustal differentiation, *in* Vielzeuf D., and Vidal P., eds., Granulites and crustal differentiation: Dordrecht, Kluwer Academic Publishers, 59–85.

Vielzeuf D. and Holloway J. R. (1988): Experimental determination of the fluid-absent melting relations in the politic system. Contributions to Mineralogy and Petrology, 98, 257-276.

Vielzeuf D. and Montel J. M. (1994): Partial melting of metagreywackes. Part I. Fluid-absent experiments and phase relationships. Contributions to Mineralogy and Petrology, 117, 375-393.

Vielzeuf D. and Schmidt M. W. (2001): Melting relations in hydrous systems revisited: application to metapelites, metagreywackes and metabasalts. Contributions to Mineralogy and Petrology, 141, 251-267.

Villaros A., Stevens G. and Buick I. S. (2009): Tracking S-type granite from source to emplacement: clues from garnet in the Cape Granite Suite. Lithos, 112, 217-235.

Waters D.J. (2001): The significance of prograde and retrograde quartz-bearing intergrowth microstructures in partially-melted granulite-facies rocks. Lithos, 56, 97-110.

Webster J. D. (2006): Melt Inclusions in Plutonic Rocks. Mineralogical Association of Canada, Short Course 36, 237 p.

White R.W., Powell R. and Halpin A. (2004): Spatially-focussed melt formation in aluminous metapelites from Broken Hill, Australia. Journal of Metamorphic Geology, 22, 825-845.

White R. W. and Powell R. (2010): Retrograde melt-residue interaction and the formation of near-anhydrous leucosomes in migmatites. Journal of Metamorphic Geology, 28, 579-597.

White R. W., Powell R. and Holland T. J. B. (2001): Calculation of partial melting equilibria in the system Na2O-CaO-K2OFeO-MgO-Al2O3-SiO2-H2O (NCKFMASH). Journal of Metamorphic Geology, 19, 139-153.

White R. W., Powell R. and Holland T. J. B. (2007): Progress relating to calculation of partial melting equilibria for metapelites. Journal of Metamorphic Geology, 25, 511-527.

White R. W., Stevens G. and Johnson T. E. (2011): Is the crucible reproducible? Reconciling melting experiments with thermodynamic calculations. Elements, 7/4, 241-246.

Zindler A., Staudigel H., Hart S.R., Endres R., and Goldstein S. (1983): Nd and Sm isotopic study of a mafic layer from Ronda ultramafic complex: Nature,. 304, 226.

Acknowledgements

… concedetemi un po' di italiano dato che mi sono ridotto a scrivere i ringraziamenti alla notte dell'ultimo giorno disponibile. Sarò laconico. Desidero ringraziare i mie tutori, Antonio Acosta-Vigil, Bernardo Cesare e Sandro Meli per avermi dato la possibilità, anche finanziaria, di portare avanti questa ricerca sotto la loro supervisione. Grazie a Maria Luce Frezzotti, Stefano Poli, Emma Salvioli-Mariani e Lucie Tajcmanova per il loro aiuto e le numerose discussioni. Grazie a Bob Bodnar per avermi accolto nel suo laboratorio e grazie a tutti i ragazzi del Virginia Tech (Rosario, Daniel, Yuri, Matt, Pilar, Angela, Rita, Gulcan, Hector, Elizabeth, Ryan). Inoltre desidero ringraziare Rosario Esposito e Silvio Ferrero per tutte le (infinite ?) discussioni sulle nostre (amate ?) inclusioni.

Voglio ringraziare anche i numerosi tecnici che mi hanno assistito in questi anni nelle lunghe giornate di laboratorio: Andrea Cavallo, Andrea Risplendente, Charles Farley, Steve McCartney, Luca Peruzzo, Raul Carampin.

Un ringraziamento veramente speciale alle mie "colleghe", Luciana e Antonella, grazie per le nostre pause caffè, per gli aperitivi mai fatti, per sopportare il mio "pensare ad alta voce", grazie per questi tre anni di "convivenza".

Grazie agli amici del Crinale.it

Grazie a Claudia e Bimbo per esserci sempre, soprattutto in periodi come questi.

Dedicato a Cristian.

SUPPLEMENTARY MATERIAL

1) EMP analyses of minerals

Position	Ms included in K-feldspar						Ms in neosome				
Na_2O	0.56	0.53	0.53	0.41	0.47	0.51	0.67	0.51	0.47	0.47	0.59
MgO	0.46	0.28	0.82	0.31	0.65	0.67	0.48	0.57	0.42	0.65	0.56
Al_2O_3	35.92	36.77	35.06	36.62	35.28	35.13	36.33	35.52	35.87	35.28	35.32
SiO_2	46.94	47.23	46.26	46.45	47.36	47.44	46.50	46.79	45.61	47.36	46.84
K_2O	10.59	10.45	10.41	10.43	10.34	10.39	10.23	10.24	10.65	10.34	10.10
CaO	0.01	0.00	0.01	0.03	0.01	0.01	0.00	0.00	0.00	0.01	0.01
TiO_2	0.22	0.17	0.29	0.09	0.18	0.32	0.34	0.09	0.03	0.18	0.16
Cr_2O_3	0.02	0.00	0.04	0.00	0.00	0.00	0.00	0.00	0.00	0.00	0.02
Mno	0.01	0.00	0.01	0.00	0.00	0.00	0.00	0.01	0.00	0.00	0.06
FeO	0.95	0.74	1.84	0.96	1.22	1.13	1.05	1.07	1.19	1.22	1.02
BaO	0.10	0.03	0.04	0.19	0.03	0.08	0.14	0.00	0.15	0.03	0.04
F	0.00	0.00	0.00	0.00	0.00	0.00	0.00	0.00	0.00	0.00	0.00
Cl	0.00	0.01	0.01	0.01	0.02	0.00	0.00	0.01	0.01	0.02	0.01
Tot.	95.79	96.23	95.33	95.49	95.56	95.68	95.74	94.82	94.40	95.56	94.74
O=F,Cl	0.00	0.00	0.00	0.00	0.00	0.00	0.00	0.00	0.00	0.00	0.00
Tot.	95.79	96.23	95.33	95.49	95.55	95.68	95.74	94.82	94.40	95.55	94.73
Si	6.199	6.186	6.170	6.149	6.260	6.265	6.142	6.227	6.133	6.260	6.239
Ti	0.022	0.017	0.029	0.009	0.018	0.032	0.034	0.009	0.003	0.018	0.016
Al	5.591	5.676	5.511	5.713	5.496	5.468	5.655	5.571	5.685	5.496	5.544
Cr	0.002	0.000	0.004	0.000	0.000	0.000	0.000	0.000	0.000	0.000	0.002
Fe^{2+}	0.105	0.082	0.205	0.107	0.135	0.125	0.116	0.119	0.134	0.135	0.114
Mn	0.002	0.000	0.002	0.000	0.000	0.000	0.000	0.002	0.000	0.000	0.007
Mg	0.091	0.056	0.164	0.061	0.129	0.132	0.094	0.113	0.084	0.129	0.111
Ca	0.001	0.000	0.001	0.004	0.002	0.002	0.000	0.000	0.000	0.002	0.002
Na	0.144	0.136	0.138	0.105	0.120	0.131	0.172	0.132	0.122	0.120	0.154
K	1.784	1.746	1.771	1.761	1.744	1.751	1.724	1.739	1.827	1.744	1.716
Ba	0.005	0.001	0.002	0.010	0.001	0.004	0.007	0.000	0.008	0.001	0.002
F	0.000	0.000	0.000	0.000	0.000	0.000	0.000	0.000	0.000	0.000	0.000
Cl	0.000	0.003	0.002	0.002	0.004	0.001	0.000	0.003	0.002	0.004	0.003

Table S1: Microprobe analyses of **muscovite** in **metatexite**. All Fe considered as Fe^{2+}. Normalized to 22 oxygens.

Position	Bt in neosome								Bt included in K-feldspar			Bt in leucosome					Bt in contact with garnet				
Na_2O	0.20	0.08	0.19	0.21	0.21	0.20	0.15	0.24	0.19	0.10	0.15	0.17	0.18	0.19	0.21	0.17	0.15	0.15	0.11	0.22	0.14
MgO	6.59	6.54	6.41	6.47	6.24	6.46	6.38	6.23	6.33	6.49	6.34	6.00	6.45	6.16	6.29	6.17	6.39	6.75	6.19	6.15	5.97
Al_2O_3	19.29	19.50	19.50	19.96	19.87	19.36	19.88	20.42	18.98	18.92	19.52	19.44	19.81	19.90	20.47	20.31	20.23	21.11	20.32	20.78	20.55
SiO_2	35.27	34.83	34.97	35.26	35.18	35.39	34.89	35.45	35.51	35.41	35.75	34.58	35.42	34.43	35.35	35.46	34.88	35.68	34.92	34.80	34.84
K_2O	9.25	9.46	9.42	9.26	9.27	9.52	9.51	9.52	9.16	9.59	9.36	9.04	9.28	9.30	9.38	9.50	9.34	9.10	9.06	9.58	8.95
CaO	0.02	0.00	0.00	0.04	0.05	0.01	0.01	0.00	0.02	0.03	0.03	0.01	0.06	0.03	0.00	0.00	0.01	0.04	0.10	0.00	0.00
TiO_2	4.17	3.89	4.04	4.22	4.04	4.03	4.29	3.73	3.88	4.28	4.21	3.68	3.63	3.72	3.45	3.67	2.59	2.10	2.44	2.54	2.77
Cr_2O_3	0.07	0.01	0.10	0.11	0.01	0.04	0.03	0.03	0.00	0.00	0.00	0.06	0.03	0.05	0.02	0.04	0.00	0.02	0.02	0.00	0.08
Mno	0.16	0.18	0.15	0.21	0.18	0.19	0.18	0.21	0.15	0.19	0.12	0.13	0.17	0.19	0.21	0.26	0.21	0.15	0.17	0.29	0.27
FeO	21.73	21.98	22.04	22.16	21.84	21.53	21.68	22.30	21.29	21.76	21.38	21.92	21.95	22.08	22.75	22.49	23.01	22.68	22.22	22.54	21.85
BaO	0.12	0.01	0.01	0.03	0.07	0.09	0.02	0.00	0.18	0.05	0.09	0.00	0.00	0.00	0.12	0.04	0.00	0.02	0.08	0.00	0.21
F	0.27	0.25	0.38	0.39	0.26	0.38	0.28	0.42	0.22	0.30	0.29	0.28	0.25	0.26	0.34	0.41	0.34	0.24	0.28	0.33	0.24
Cl	0.07	0.06	0.06	0.07	0.07	0.06	0.07	0.11	0.07	0.05	0.08	0.06	0.04	0.07	0.09	0.10	0.08	0.05	0.07	0.10	0.10
Tot.	97.22	96.80	97.25	98.39	97.28	97.25	97.37	98.67	95.98	97.17	97.33	95.37	97.27	96.37	98.68	98.61	97.22	98.09	95.98	97.34	95.97
O=F,Cl	-0.13	-0.12	-0.17	-0.18	-0.12	-0.17	-0.13	-0.20	-0.11	-0.14	-0.14	-0.13	-0.12	-0.13	-0.16	-0.19	-0.16	-0.11	-0.13	-0.16	-0.12
Tot.	97.09	96.68	97.08	98.21	97.15	97.07	97.24	98.47	95.87	97.03	97.19	95.24	97.15	96.25	98.51	98.42	97.06	97.98	95.84	97.17	95.85
Si	5.322	5.290	5.285	5.260	5.303	5.338	5.259	5.275	5.414	5.353	5.369	5.322	5.335	5.256	5.272	5.286	5.289	5.324	5.337	5.267	5.320
Ti	0.473	0.444	0.459	0.474	0.458	0.457	0.486	0.418	0.445	0.487	0.476	0.426	0.411	0.427	0.387	0.412	0.295	0.236	0.281	0.289	0.318
Al	3.431	3.490	3.474	3.509	3.530	3.441	3.532	3.581	3.410	3.371	3.455	3.526	3.517	3.580	3.598	3.568	3.616	3.712	3.660	3.707	3.699
Cr	0.008	0.002	0.012	0.013	0.001	0.004	0.003	0.003	0.000	0.000	0.000	0.007	0.004	0.006	0.002	0.004	0.000	0.003	0.003	0.000	0.009
Fe^{2+}	2.742	2.792	2.786	2.764	2.753	2.716	2.733	2.775	2.714	2.751	2.685	2.821	2.765	2.819	2.837	2.804	2.918	2.830	2.840	2.853	2.790
Mn	0.021	0.023	0.019	0.027	0.023	0.024	0.023	0.027	0.019	0.024	0.015	0.017	0.022	0.024	0.027	0.032	0.027	0.018	0.022	0.038	0.034
Mg	1.483	1.481	1.444	1.439	1.402	1.452	1.434	1.382	1.439	1.463	1.419	1.377	1.448	1.402	1.398	1.371	1.445	1.501	1.410	1.388	1.359
Ca	0.003	0.000	0.000	0.006	0.008	0.002	0.002	0.001	0.004	0.004	0.005	0.002	0.009	0.005	0.000	0.000	0.002	0.006	0.017	0.000	0.000
Na	0.059	0.024	0.055	0.062	0.060	0.057	0.044	0.069	0.057	0.030	0.045	0.051	0.051	0.055	0.060	0.050	0.043	0.043	0.032	0.064	0.043
K	1.781	1.833	1.816	1.762	1.783	1.832	1.829	1.807	1.782	1.850	1.793	1.775	1.783	1.811	1.785	1.807	1.807	1.732	1.767	1.850	1.744
Ba	0.007	0.001	0.000	0.002	0.004	0.005	0.001	0.000	0.011	0.003	0.005	0.000	0.000	0.000	0.007	0.002	0.000	0.001	0.005	0.000	0.013
F	0.033	0.121	0.180	0.184	0.122	0.182	0.034	0.199	0.026	0.145	0.140	0.034	0.120	0.127	0.040	0.193	0.040	0.113	0.134	0.160	0.029
Cl	0.017	0.016	0.015	0.018	0.017	0.015	0.017	0.028	0.017	0.013	0.020	0.015	0.011	0.017	0.024	0.025	0.020	0.014	0.017	0.026	0.025
Sito A	1.843	1.857	1.872	1.830	1.851	1.891	1.875	1.877	1.843	1.884	1.843	1.828	1.844	1.871	1.844	1.856	1.852	1.781	1.815	1.914	1.787
X_{Mg}	0.35	0.35	0.34	0.34	0.34	0.35	0.34	0.33	0.35	0.35	0.35	0.33	0.34	0.33	0.33	0.33	0.33	0.35	0.33	0.33	0.33

Table S2: Representative microprobe analyses of **biotite** in **metatexite**. All Fe considered as Fe^{2+}. Normalized to 22 oxygens

Position	Bt in neosome								Bt in leucosome			Bt included in Kfs		Bt included in Grt		Bt in contact with garnet					
Na_2O	0.07	0.12	0.17	0.12	0.10	0.07	0.08	0.11	0.11	0.11	0.13	0.14	0.18	0.30	0.25	0.10	0.11	0.07	0.06	0.10	0.12
MgO	9.06	9.42	9.24	10.20	10.14	8.09	9.26	9.07	10.32	10.28	9.25	9.68	8.63	10.56	10.28	10.83	10.21	10.46	11.52	10.18	9.64
Al_2O_3	17.23	16.64	17.19	17.59	17.15	18.12	18.33	17.24	17.45	17.34	18.62	17.74	17.47	18.25	18.37	18.55	18.76	17.50	18.19	17.43	17.18
SiO_2	35.80	36.44	36.13	36.21	36.01	36.42	36.39	36.31	36.89	36.04	35.81	36.31	36.41	36.22	36.05	35.84	36.48	36.83	37.16	36.63	36.40
K_2O	9.26	9.64	9.72	9.60	9.55	9.64	9.64	9.44	9.19	9.02	9.70	9.45	9.37	9.51	9.14	9.41	9.36	9.58	9.14	9.23	9.49
CaO	0.05	0.01	0.00	0.03	0.03	0.00	0.00	0.06	0.00	0.01	0.00	0.03	0.05	0.00	0.01	0.01	0.00	0.02	0.01	0.02	0.02
TiO_2	5.61	6.00	5.61	4.80	5.20	6.26	5.13	4.63	4.88	4.27	4.74	5.09	5.99	5.57	5.90	2.25	4.14	3.74	1.89	4.42	4.93
Cr_2O_3	0.07	0.03	0.05	0.04	0.11	0.09	0.09	0.08	0.06	0.00	0.04	0.03	0.11	0.00	0.02	0.05	0.06	0.01	0.04	0.10	0.06
Mno	0.06	0.01	0.09	0.01	0.08	0.03	0.01	0.03	0.04	0.04	0.03	0.08	0.02	0.01	0.03	0.07	0.03	0.04	0.00	0.03	0.01
FeO	18.81	19.54	19.60	18.76	19.14	19.13	18.70	20.20	18.67	18.34	19.05	18.07	19.47	17.22	17.40	19.39	18.68	19.52	18.39	19.33	19.41
BaO	0.02	0.03	0.14	0.00	0.10	0.01	0.02	0.10	0.00	0.10	0.08	0.00	0.08	0.10	0.06	0.00	0.00	0.10	0.04	0.08	0.03
F	0.98	0.91	0.90	1.04	1.00	0.73	0.90	1.02	1.11	1.39	0.93	1.05	0.86	1.03	0.98	1.49	1.10	1.06	1.36	1.12	0.85
Cl	0.36	0.36	0.51	0.51	0.41	0.45	0.39	0.56	0.41	0.40	0.33	0.38	0.40	0.39	0.46	0.19	0.32	0.35	0.24	0.46	0.39
Tot.	97.38	99.16	99.35	98.90	99.02	99.04	98.95	98.85	99.14	97.34	98.71	98.06	99.05	99.15	98.95	98.19	99.26	99.29	98.04	99.12	98.53
O=F,Cl	-0.49	-0.46	-0.50	-0.55	-0.51	-0.41	-0.47	-0.56	-0.56	-0.68	-0.47	-0.53	-0.45	-0.52	-0.52	-0.67	-0.54	-0.53	-0.63	-0.57	-0.44
Tot.	96.89	98.69	98.86	98.35	98.50	98.63	98.48	98.29	98.58	96.66	98.24	97.53	98.59	98.63	98.43	97.51	98.72	98.76	97.42	98.55	98.09
Si	5.330	5.352	5.311	5.310	5.293	5.333	5.321	5.364	5.369	5.346	5.268	5.344	5.342	5.257	5.238	5.293	5.301	5.387	5.443	5.358	5.369
Ti	0.628	0.663	0.620	0.529	0.575	0.690	0.564	0.515	0.534	0.476	0.524	0.564	0.661	0.608	0.645	0.250	0.453	0.411	0.208	0.486	0.547
Al	3.023	2.880	2.978	3.040	2.971	3.127	3.159	3.002	2.993	3.032	3.228	3.077	3.021	3.122	3.146	3.229	3.213	3.017	3.140	3.005	2.987
Cr	0.008	0.004	0.006	0.004	0.013	0.010	0.011	0.009	0.007	0.000	0.004	0.004	0.013	0.000	0.002	0.006	0.006	0.001	0.005	0.012	0.008
Fe^{2+}	2.342	2.400	2.409	2.301	2.353	2.343	2.287	2.496	2.272	2.275	2.344	2.224	2.389	2.090	2.114	2.395	2.270	2.388	2.253	2.365	2.394
Mn	0.008	0.002	0.011	0.001	0.010	0.004	0.002	0.004	0.005	0.005	0.004	0.009	0.003	0.001	0.004	0.009	0.004	0.005	0.000	0.004	0.001
Mg	2.011	2.063	2.025	2.230	2.222	1.766	2.018	1.998	2.239	2.273	2.029	2.124	1.888	2.285	2.227	2.384	2.212	2.281	2.516	2.220	2.120
Ca	0.008	0.001	0.000	0.004	0.005	0.000	0.000	0.009	0.000	0.001	0.000	0.005	0.007	0.000	0.002	0.002	0.001	0.003	0.002	0.003	0.003
Na	0.021	0.033	0.048	0.035	0.028	0.021	0.023	0.031	0.032	0.031	0.037	0.041	0.052	0.084	0.070	0.027	0.032	0.021	0.017	0.028	0.034
K	1.759	1.806	1.823	1.796	1.791	1.801	1.798	1.779	1.706	1.707	1.820	1.774	1.754	1.761	1.694	1.773	1.735	1.788	1.708	1.722	1.786
Ba	0.001	0.002	0.008	0.000	0.006	0.001	0.001	0.006	0.000	0.006	0.005	0.000	0.005	0.005	0.003	0.000	0.000	0.006	0.002	0.005	0.002
F	0.115	0.422	0.419	0.121	0.464	0.336	0.415	0.119	0.128	0.652	0.433	0.122	0.398	0.118	0.450	0.174	0.506	0.490	0.630	0.130	0.395
Cl	0.091	0.090	0.128	0.126	0.102	0.111	0.098	0.141	0.102	0.101	0.082	0.095	0.100	0.095	0.113	0.048	0.079	0.087	0.060	0.113	0.097
Sito A	1.788	1.841	1.871	1.835	1.824	1.822	1.822	1.820	1.739	1.740	1.857	1.820	1.813	1.844	1.766	1.802	1.768	1.811	1.727	1.753	1.823
X_{Mg}	0.462	0.462	0.457	0.492	0.486	0.430	0.469	0.445	0.496	0.500	0.464	0.488	0.441	0.522	0.513	0.499	0.493	0.489	0.528	0.484	0.470

Table S3: Representative microprobe analyses of **biotite** in **mylonite**. All Fe considered as Fe^{2+}. Normalized to 22 oxygens.

Position	MI-brg	MI-brg	MI-brg	MI-brg	MI-brg	MI-free	MI-free	MI-free	MI-brg	MI-brg	MI-brg	MI-brg	MI-free	MI-free	MI-free	MI-brg	MI-brg	MI-free	MI-free
	c	c	c	c	c	c	c	c	r	r	r	r	r	r	r	r/b	r/b	r/b	r/b
Na_2O	0.00	0.05	0.00	0.00	0.01	0.00	0.00	0.00	0.00	0.00	0.01	0.02	0.00	0.00	0.00	0.00	0.01	0.02	0.00
MgO	2.81	2.61	3.18	3.20	2.81	3.09	3.13	2.78	2.62	2.25	2.44	2.54	2.47	2.58	2.66	2.29	2.05	2.36	2.40
Al_2O_3	20.95	21.64	21.16	21.28	20.77	20.70	21.46	20.80	21.00	21.31	21.07	20.96	21.35	20.75	20.83	20.83	20.65	20.93	21.13
SiO_2	36.60	37.48	36.83	36.88	36.55	36.66	36.84	36.52	36.34	36.71	36.45	37.00	36.79	36.78	36.84	37.41	37.22	37.05	37.32
CaO	1.00	0.96	0.91	0.98	1.26	0.90	0.90	0.88	1.02	1.03	0.95	0.88	0.92	0.91	0.84	1.02	0.87	0.93	0.94
TiO_2	0.02	0.04	0.00	0.03	0.04	0.02	0.01	0.03	0.01	0.01	0.00	0.00	0.00	0.02	0.03	0.01	0.01	0.01	0.04
Mno	3.58	3.96	3.29	3.16	3.48	3.16	3.04	4.13	4.11	4.97	5.15	4.43	4.72	4.49	4.67	4.37	4.43	4.32	4.52
FeO	34.99	34.92	35.14	34.89	35.28	35.37	34.72	34.52	33.98	34.20	33.90	34.64	33.91	34.43	34.44	34.97	35.01	34.42	34.37
Tot	99.96	101.66	100.50	100.43	100.20	99.90	100.08	99.66	99.09	100.49	99.96	100.47	100.17	99.96	100.32	100.91	100.26	100.06	100.73
Si	2.971	2.983	2.967	2.968	2.966	2.977	2.970	2.975	2.972	2.969	2.965	2.989	2.976	2.988	2.984	3.010	3.018	3.002	3.001
Ti	0.001	0.003	0.000	0.002	0.002	0.001	0.001	0.002	0.000	0.001	0.000	0.000	0.000	0.001	0.002	0.001	0.001	0.001	0.002
Al	2.005	2.029	2.009	2.019	1.987	1.981	2.039	1.997	2.024	2.031	2.020	1.996	2.036	1.987	1.988	1.976	1.973	1.999	2.003
Fe^{2+}	2.376	2.324	2.367	2.348	2.394	2.402	2.340	2.351	2.324	2.313	2.306	2.341	2.294	2.339	2.332	2.354	2.374	2.332	2.312
Mn	0.246	0.267	0.224	0.215	0.239	0.217	0.207	0.285	0.285	0.341	0.355	0.303	0.323	0.309	0.321	0.298	0.304	0.297	0.308
Mg	0.340	0.310	0.381	0.384	0.340	0.374	0.376	0.338	0.320	0.271	0.296	0.306	0.298	0.313	0.321	0.275	0.248	0.285	0.288
Ca	0.087	0.082	0.078	0.085	0.109	0.078	0.078	0.076	0.089	0.089	0.083	0.076	0.080	0.079	0.073	0.088	0.076	0.081	0.081
Na	0.000	0.007	0.000	0.000	0.002	0.000	0.000	0.000	0.001	0.000	0.002	0.002	0.000	0.000	0.000	0.000	0.001	0.003	0.000
Alm	0.78	0.78	0.78	0.77	0.78	0.78	0.78	0.77	0.77	0.77	0.76	0.77	0.77	0.77	0.77	0.78	0.79	0.78	0.77
Prp	0.11	0.10	0.12	0.13	0.11	0.12	0.13	0.11	0.11	0.09	0.10	0.10	0.10	0.10	0.11	0.09	0.08	0.10	0.10
Sps	0.08	0.09	0.07	0.07	0.08	0.07	0.07	0.09	0.09	0.11	0.12	0.10	0.11	0.10	0.11	0.10	0.10	0.10	0.10
Grs	0.03	0.03	0.03	0.03	0.04	0.03	0.03	0.03	0.03	0.03	0.03	0.03	0.03	0.03	0.02	0.03	0.03	0.03	0.03
X_{Fe}	0.87	0.88	0.86	0.86	0.88	0.87	0.86	0.87	0.88	0.89	0.89	0.88	0.88	0.88	0.88	0.90	0.91	0.89	0.89
X_{Mg}	0.13	0.12	0.14	0.14	0.12	0.13	0.14	0.13	0.12	0.11	0.11	0.12	0.12	0.12	0.12	0.10	0.09	0.11	0.11

Table S4: Representative microprobe analyses of **garnet** in **metatexite**. All Fe considered as Fe^{2+}. Normalized to 12 oxygens. MI-brg: MI-bearing garnet; MI-free: garnet free of MI. c: core; r: rim; r/b: rim in contact with biotite.

Position	Grt in leucosome										Grt in neosome							
	MI-brg	MI-brg	MI-brg	MI-brg	MI-brg	MI-brg	MI-free	MI-free	MI-free	MI-free	MI-brg	MI-brg	MI-brg	MI-brg	MI-brg	MI-free	MI-free	MI-free
	c	c	c	c	c	c	c	c	c	c	c	c	c	c	c	c	c	c
Na_2O	0.00	0.00	0.00	0.03	0.00	0.00	0.00	0.00	0.00	0.04	0.00	0.01	0.00	0.00	0.00	0.00	0.00	0.00
MgO	5.32	6.05	5.56	5.64	5.57	5.74	5.77	5.74	5.92	5.79	5.75	5.68	5.41	5.83	5.79	5.48	5.43	5.58
Al_2O_3	21.48	21.68	21.41	21.37	21.52	21.43	21.76	21.59	21.69	21.13	21.76	21.81	21.60	21.58	21.52	21.57	21.54	21.41
SiO_2	37.50	37.83	37.80	37.42	37.46	37.64	36.91	37.09	37.46	37.39	37.25	37.34	37.31	37.52	37.35	37.60	37.33	37.23
CaO	0.79	0.94	0.80	0.78	0.79	0.77	0.71	0.77	0.73	0.83	0.74	0.67	0.67	0.67	0.74	0.96	0.72	0.81
TiO_2	0.05	0.02	0.01	0.00	0.05	0.01	0.03	0.02	0.03	0.03	0.04	0.00	0.02	0.03	0.06	0.03	0.01	0.02
Mno	1.05	1.18	1.11	1.10	1.15	1.12	1.07	1.09	1.13	1.10	0.95	0.94	0.96	0.95	0.90	0.83	0.89	0.84
FeO	34.93	33.28	33.63	34.04	34.26	33.95	33.56	33.81	33.59	33.32	34.38	33.99	34.55	34.28	33.87	34.19	34.62	33.85
Tot	101.12	100.98	100.31	100.38	100.80	100.65	99.81	100.13	100.56	99.64	100.88	100.43	100.52	100.85	100.23	100.67	100.53	99.74
Si	2.962	2.969	2.991	2.968	2.961	2.974	2.940	2.948	2.958	2.980	2.941	2.955	2.959	2.960	2.961	2.971	2.960	2.967
Ti	0.003	0.001	0.000	0.000	0.003	0.001	0.002	0.001	0.002	0.002	0.003	0.000	0.001	0.002	0.003	0.002	0.001	0.001
Al	2.000	2.006	1.996	1.998	2.005	1.995	2.043	2.023	2.019	1.985	2.025	2.034	2.019	2.007	2.011	2.009	2.013	2.012
Fe^{2+}	2.307	2.185	2.225	2.258	2.265	2.243	2.235	2.248	2.218	2.221	2.271	2.249	2.292	2.262	2.246	2.259	2.296	2.256
Mn	0.070	0.078	0.075	0.074	0.077	0.075	0.072	0.074	0.076	0.074	0.064	0.063	0.065	0.064	0.061	0.056	0.060	0.057
Mg	0.626	0.708	0.656	0.666	0.656	0.676	0.685	0.680	0.697	0.689	0.677	0.670	0.640	0.685	0.684	0.645	0.642	0.662
Ca	0.067	0.079	0.068	0.066	0.067	0.065	0.061	0.066	0.062	0.071	0.063	0.056	0.057	0.056	0.063	0.082	0.061	0.069
Na	0.001	0.000	0.000	0.004	0.000	0.000	0.000	0.000	0.000	0.006	0.000	0.002	0.000	0.000	0.000	0.000	0.000	0.000
Alm	0.75	0.72	0.74	0.74	0.74	0.73	0.73	0.73	0.73	0.73	0.74	0.74	0.75	0.74	0.74	0.74	0.75	0.74
Prp	0.20	0.23	0.22	0.22	0.21	0.22	0.22	0.22	0.23	0.23	0.22	0.22	0.21	0.22	0.22	0.21	0.21	0.22
Sps	0.02	0.03	0.02	0.02	0.03	0.02	0.02	0.02	0.02	0.02	0.02	0.02	0.02	0.02	0.02	0.02	0.02	0.02
Grs	0.02	0.03	0.02	0.02	0.02	0.02	0.02	0.02	0.02	0.02	0.02	0.02	0.02	0.02	0.02	0.03	0.02	0.02
X_{Fe}	0.79	0.76	0.77	0.77	0.78	0.77	0.77	0.77	0.76	0.76	0.77	0.77	0.78	0.77	0.77	0.78	0.78	0.77
X_{Mg}	0.21	0.24	0.23	0.23	0.22	0.23	0.23	0.23	0.24	0.24	0.23	0.23	0.22	0.23	0.23	0.22	0.22	0.23

Table S5: Representative microprobe analyses of **garnet** in **mylonite**. All Fe considered as Fe^{2+}. Normalized to 12 oxygens. MI-brg: MI-bearing garnet; MI-free: garnet free of MI. c: core; r: rim; r/b: rim in contact with biotite

Position	Grt in leucosome				Grt in neosome						Grt in leucosome				Grt in neosome		
	MI-brg	MI-brg	MI-free	MI-free	MI-brg	MI-brg	MI-brg	MI-brg	MI-brg	MI-brg	MI-brg	MI-brg	MI-brg	MI-brg	MI-brg	MI-brg	MI-free
	r	r	r	r	r	r	r	r	r	r	r/b	r/b	r/b	r/b	r/b	r/b	r/b
Na_2O	0.00	0.00	0.00	0.01	0.00	0.00	0.00	0.00	0.00	0.00	0.01	0.00	0.00	0.01	0.00	0.03	0.01
MgO	6.11	5.79	5.81	5.91	5.16	5.69	5.58	5.61	5.67	5.72	3.94	4.31	4.54	4.89	4.97	4.97	4.91
Al_2O_3	21.50	21.45	21.61	21.58	21.25	21.57	21.57	21.58	21.75	21.66	21.50	21.43	21.75	21.74	21.51	21.54	21.72
SiO_2	37.40	37.30	37.20	37.40	36.92	37.55	37.45	37.58	37.46	37.19	37.32	37.62	37.53	37.30	37.32	37.17	37.60
CaO	0.78	0.70	0.72	0.71	0.76	0.71	0.75	0.67	0.69	0.71	0.74	0.68	0.75	0.72	0.74	0.66	0.72
TiO_2	0.00	0.05	0.00	0.00	0.03	0.02	0.00	0.00	0.04	0.03	0.02	0.04	0.07	0.04	0.03	0.02	0.04
Mno	1.09	1.15	1.07	1.21	0.94	1.00	0.89	0.90	0.93	0.87	1.47	1.35	1.37	1.16	0.99	0.95	0.94
FeO	33.09	33.93	33.43	33.38	34.38	34.10	33.95	34.26	33.79	33.78	35.52	35.30	35.55	34.61	34.61	34.82	35.19
Tot	99.96	100.37	99.84	100.20	99.44	100.64	100.16	100.61	100.33	99.97	100.52	100.72	101.56	100.47	100.17	100.15	101.13
Si	2.965	2.958	2.959	2.963	2.964	2.967	2.971	2.971	2.964	2.955	2.980	2.990	2.961	2.963	2.972	2.964	2.969
Ti	0.000	0.003	0.000	0.000	0.002	0.001	0.000	0.000	0.002	0.002	0.001	0.002	0.004	0.002	0.002	0.001	0.002
Al	2.009	2.005	2.025	2.015	2.010	2.009	2.016	2.010	2.028	2.029	2.023	2.007	2.022	2.035	2.019	2.024	2.021
Fe^{2+}	2.194	2.250	2.223	2.212	2.308	2.253	2.252	2.264	2.236	2.245	2.371	2.346	2.346	2.299	2.305	2.321	2.323
Mn	0.073	0.077	0.072	0.081	0.064	0.067	0.060	0.060	0.062	0.059	0.099	0.091	0.091	0.078	0.067	0.064	0.063
Mg	0.722	0.684	0.689	0.697	0.617	0.671	0.659	0.662	0.669	0.678	0.469	0.511	0.534	0.579	0.590	0.591	0.578
Ca	0.066	0.060	0.062	0.060	0.065	0.060	0.063	0.057	0.059	0.060	0.063	0.058	0.063	0.062	0.063	0.057	0.061
Na	0.000	0.000	0.000	0.002	0.000	0.000	0.000	0.000	0.000	0.000	0.001	0.000	0.000	0.002	0.000	0.004	0.001
Alm	0.72	0.73	0.73	0.73	0.76	0.74	0.74	0.74	0.74	0.74	0.79	0.78	0.77	0.76	0.76	0.77	0.77
Prp	0.24	0.22	0.23	0.23	0.20	0.22	0.22	0.22	0.22	0.22	0.16	0.17	0.18	0.19	0.20	0.19	0.19
Sps	0.02	0.03	0.02	0.03	0.02	0.02	0.02	0.02	0.02	0.02	0.03	0.03	0.03	0.03	0.02	0.02	0.02
Grs	0.02	0.02	0.02	0.02	0.02	0.02	0.02	0.02	0.02	0.02	0.02	0.02	0.02	0.02	0.02	0.02	0.02
X_{Fe}	0.75	0.77	0.76	0.76	0.79	0.77	0.77	0.77	0.77	0.77	0.83	0.82	0.81	0.80	0.80	0.80	0.80
X_{Mg}	0.25	0.23	0.24	0.24	0.21	0.23	0.23	0.23	0.23	0.23	0.17	0.18	0.19	0.20	0.20	0.20	0.20

Table S5: continued.

Position	Feldspars in leucosome																	
	Plagioclase										K-feldspar							
Na_2O	8.38	8.64	8.56	8.50	8.70	8.38	8.65	8.71	8.76	8.94	1.98	2.36	2.07	1.99	2.15	2.39	2.14	2.01
MgO	0.00	0.00	0.00	0.00	0.01	0.01	0.00	0.02	0.00	0.00	0.01	0.00	0.00	0.01	0.00	0.01	0.01	0.01
Al_2O_3	23.88	24.24	24.15	23.88	23.81	24.00	23.72	24.08	23.62	23.19	18.80	18.65	18.80	18.79	18.79	19.00	18.76	18.90
SiO_2	62.04	62.11	62.08	62.20	62.70	62.30	62.69	62.25	63.16	62.96	64.67	65.68	65.49	65.16	65.19	65.58	65.99	65.83
K_2O	0.25	0.33	0.32	0.46	0.45	0.44	0.39	0.34	0.40	0.38	13.84	13.22	13.63	13.81	13.60	13.36	13.53	13.73
CaO	4.92	5.23	5.11	5.11	5.00	5.09	4.73	5.08	4.71	4.50	0.08	0.09	0.06	0.07	0.06	0.07	0.08	0.06
TiO_2	0.00	0.00	0.00	0.04	0.00	0.00	0.00	0.02	0.01	0.00	0.05	0.00	0.00	0.00	0.00	0.01	0.06	0.03
MnO	0.00	0.00	0.00	0.02	0.00	0.01	0.02	0.00	0.00	0.03	0.02	0.04	0.00	0.00	0.00	0.01	0.04	0.02
FeO	0.00	0.02	0.00	0.00	0.04	0.02	0.03	0.00	0.03	0.03	0.00	0.02	0.07	0.00	0.00	0.00	0.05	0.04
Tot.	99.47	100.58	100.22	100.22	100.72	100.24	100.22	100.50	100.70	100.04	99.44	100.07	100.12	99.84	99.79	100.43	100.65	100.63
Si	2.760	2.741	2.746	2.754	2.762	2.755	2.770	2.748	2.778	2.787	2.982	2.999	2.993	2.989	2.990	2.986	2.998	2.993
Ti	0.000	0.000	0.000	0.001	0.000	0.000	0.000	0.001	0.000	0.000	0.002	0.000	0.000	0.000	0.000	0.000	0.002	0.001
Al	1.252	1.261	1.259	1.246	1.236	1.251	1.235	1.253	1.224	1.210	1.022	1.004	1.013	1.016	1.016	1.020	1.004	1.013
Fe^{2+}	0.000	0.001	0.000	0.000	0.002	0.001	0.001	0.000	0.001	0.001	0.000	0.001	0.003	0.000	0.000	0.000	0.002	0.001
Mn	0.000	0.000	0.000	0.001	0.000	0.000	0.001	0.000	0.000	0.001	0.001	0.002	0.000	0.000	0.000	0.000	0.001	0.001
Mg	0.000	0.000	0.000	0.000	0.001	0.001	0.000	0.001	0.000	0.000	0.001	0.000	0.000	0.001	0.000	0.001	0.001	0.001
Ca	0.234	0.247	0.242	0.242	0.236	0.241	0.224	0.240	0.222	0.213	0.004	0.004	0.003	0.004	0.003	0.003	0.004	0.003
Na	0.723	0.739	0.734	0.730	0.743	0.718	0.741	0.745	0.747	0.767	0.177	0.209	0.183	0.177	0.191	0.211	0.188	0.177
K	0.014	0.019	0.018	0.026	0.025	0.025	0.022	0.019	0.023	0.022	0.814	0.770	0.795	0.808	0.796	0.776	0.784	0.796
Ab	74	74	74	73	74	73	75	74	75	77	18	21	19	18	19	21	19	18
An	24	25	24	24	24	25	23	24	22	21	0	0	0	0	0	0	0	0
Or	1	2	2	3	2	2	2	2	2	2	82	78	81	82	80	78	80	82

Table S6: Representative microprobe analyses of **feldspar** in **metatexite**. All Fe considered as Fe^{2+}.

Position	Feldspars in neosome																	
	Plagioclase							Plagioclase included in K-feldspar				K-feldspar						
Na_2O	7.68	7.90	7.90	7.89	7.57	8.04	7.70	7.88	7.83	7.60	8.00	1.96	2.23	1.91	2.09	2.44	2.20	2.19
MgO	0.01	0.00	0.01	0.00	0.01	0.00	0.01	0.02	0.01	0.02	0.00	0.02	0.01	0.00	0.00	0.01	0.01	0.00
Al_2O_3	25.20	25.20	25.06	25.57	25.40	24.83	25.13	24.39	25.05	25.25	24.80	18.53	18.65	18.94	18.73	18.79	18.99	18.77
SiO_2	60.53	60.23	60.88	60.22	59.74	59.92	59.98	60.46	60.12	59.56	61.00	65.10	65.63	64.89	65.93	65.84	65.87	66.03
K_2O	0.32	0.28	0.36	0.26	0.32	0.25	0.26	0.33	0.31	0.27	0.32	13.88	13.41	13.86	13.68	13.29	13.42	13.65
CaO	6.55	6.40	6.08	6.52	6.79	6.33	6.50	6.37	6.49	6.57	6.05	0.05	0.07	0.10	0.06	0.07	0.09	0.05
TiO_2	0.00	0.05	0.01	0.02	0.05	0.00	0.03	0.02	0.03	0.03	0.00	0.00	0.04	0.01	0.07	0.00	0.00	0.00
MnO	0.00	0.00	0.00	0.04	0.02	0.00	0.09	0.02	0.02	0.04	0.00	0.00	0.00	0.02	0.00	0.00	0.00	0.02
FeO	0.00	0.05	0.13	0.39	0.06	0.00	0.00	0.02	0.05	0.07	0.06	0.00	0.01	0.02	0.05	0.01	0.08	0.03
Tot.	100.28	100.11	100.43	100.90	99.96	99.37	99.70	99.52	99.91	99.41	100.23	99.53	100.05	99.75	100.61	100.45	100.66	100.75
Si	2.686	2.680	2.697	2.664	2.665	2.686	2.679	2.705	2.681	2.669	2.706	2.997	2.998	2.981	2.998	2.995	2.991	2.998
Ti	0.000	0.002	0.000	0.001	0.002	0.000	0.001	0.001	0.001	0.001	0.000	0.000	0.001	0.000	0.002	0.000	0.000	0.000
Al	1.318	1.321	1.308	1.333	1.335	1.312	1.323	1.286	1.317	1.334	1.297	1.005	1.004	1.026	1.004	1.008	1.016	1.005
Fe^{2+}	0.000	0.002	0.005	0.014	0.002	0.000	0.000	0.001	0.002	0.003	0.002	0.000	0.000	0.001	0.002	0.000	0.003	0.001
Mn	0.000	0.000	0.000	0.001	0.001	0.000	0.003	0.001	0.001	0.002	0.000	0.000	0.000	0.001	0.000	0.000	0.000	0.001
Mg	0.001	0.000	0.001	0.000	0.000	0.000	0.000	0.002	0.001	0.001	0.000	0.001	0.001	0.000	0.000	0.001	0.001	0.000
Ca	0.311	0.305	0.289	0.309	0.325	0.304	0.311	0.305	0.310	0.315	0.288	0.002	0.003	0.005	0.003	0.003	0.005	0.003
Na	0.661	0.681	0.678	0.677	0.655	0.699	0.667	0.684	0.677	0.660	0.688	0.175	0.198	0.170	0.184	0.215	0.194	0.193
K	0.018	0.016	0.020	0.014	0.018	0.014	0.015	0.019	0.018	0.015	0.018	0.815	0.782	0.812	0.794	0.771	0.777	0.791
Ab	67	68	69	68	66	69	67	68	67	67	69	18	20	17	19	22	20	20
An	31	30	29	31	33	30	31	30	31	32	29	0	0	0	0	0	0	0
Or	2	2	2	1	2	1	1	2	2	2	2	82	80	82	81	78	80	80

Table S6: continued.

Position	Feldspars in leucosome															
	Plagioclase										K-feldspar					
Na_2O	8.13	8.20	8.37	8.29	8.20	8.08	8.33	8.31	8.47	8.73	2.22	2.58	2.49	1.81	2.03	2.42
MgO	0.00	0.00	0.02	0.00	0.01	0.01	0.01	0.02	0.02	0.00	0.00	0.02	0.01	0.01	0.00	0.00
Al_2O_3	23.62	24.12	24.24	24.09	23.71	23.98	24.02	24.11	24.43	24.33	19.11	18.85	19.09	18.95	19.04	19.15
SiO_2	62.59	62.07	61.83	62.39	62.47	62.06	62.09	61.75	61.31	61.13	65.66	66.42	67.08	65.99	66.27	66.41
K_2O	0.79	0.58	0.83	0.59	0.76	0.77	0.73	0.97	0.76	0.68	12.28	11.90	11.60	12.90	12.28	12.43
CaO	4.97	5.26	5.21	4.80	4.82	5.01	4.75	4.99	5.34	5.32	0.12	0.07	0.09	0.08	0.09	0.11
TiO_2	0.02	0.01	0.00	0.00	0.00	0.01	0.06	0.01	0.02	0.00	0.01	0.00	0.00	0.01	0.01	0.00
MnO	0.00	0.03	0.02	0.03	0.00	0.01	0.02	0.00	0.00	0.00	0.01	0.00	0.00	0.03	0.01	0.00
FeO	0.02	0.00	0.01	0.00	0.00	0.03	0.02	0.00	0.00	0.02	0.00	0.00	0.00	0.02	0.02	0.00
Tot.	100.14	100.27	100.52	100.19	99.97	99.95	100.03	100.16	100.35	100.20	99.39	99.83	100.36	99.80	99.74	100.52
Si	2.771	2.747	2.736	2.758	2.769	2.754	2.753	2.742	2.721	2.719	2.998	3.013	3.018	3.006	3.010	3.000
Ti	0.001	0.000	0.000	0.000	0.000	0.000	0.002	0.000	0.001	0.000	0.000	0.000	0.000	0.000	0.000	0.000
Al	1.232	1.258	1.264	1.255	1.239	1.254	1.255	1.262	1.278	1.275	1.028	1.008	1.012	1.017	1.019	1.020
Fe^{2+}	0.001	0.000	0.000	0.000	0.000	0.001	0.001	0.000	0.000	0.001	0.000	0.000	0.000	0.001	0.001	0.000
Mn	0.000	0.001	0.001	0.001	0.000	0.000	0.001	0.000	0.000	0.000	0.000	0.000	0.000	0.001	0.000	0.000
Mg	0.000	0.000	0.001	0.000	0.001	0.001	0.000	0.002	0.001	0.000	0.000	0.001	0.001	0.001	0.000	0.000
Ca	0.236	0.249	0.247	0.227	0.229	0.238	0.226	0.237	0.254	0.254	0.006	0.003	0.004	0.004	0.004	0.006
Na	0.698	0.704	0.718	0.711	0.705	0.696	0.716	0.715	0.728	0.753	0.197	0.227	0.217	0.160	0.179	0.212
K	0.045	0.033	0.047	0.033	0.043	0.043	0.041	0.055	0.043	0.039	0.715	0.688	0.666	0.749	0.711	0.716
Ab	71	71	71	73	72	71	73	71	71	72	21	25	25	18	20	23
An	24	25	24	23	23	24	23	24	25	24	1	0	0	0	0	1
Or	5	3	5	3	4	4	4	5	4	4	78	75	75	82	80	77

Table S7: Representative microprobe analyses of **feldspar** in **mylonite**. All Fe considered as Fe^{2+}.

Position	Feldspars in neosome																			
	Plagioclase								Plagioclase included in K-feldspar					K-feldspar						
Na_2O	7.84	7.87	8.47	7.95	7.86	8.20	7.76	8.51	7.65	8.31	7.86	7.96	7.54	2.04	2.68	2.02	1.84	2.41	1.87	1.65
MgO	0.00	0.00	0.00	0.00	0.00	0.01	0.00	0.00	0.00	0.01	0.00	0.01	0.00	0.01	0.00	0.01	0.02	0.00	0.00	0.00
Al_2O_3	24.78	24.72	24.27	24.43	24.44	24.14	24.42	24.02	25.05	24.38	24.93	24.51	24.70	19.25	19.30	19.22	18.85	18.95	18.95	18.85
SiO_2	60.50	60.44	61.27	60.73	60.53	61.26	61.27	61.68	60.33	61.05	60.71	60.94	60.69	67.06	66.11	66.62	66.21	66.87	66.71	66.77
K_2O	0.23	0.36	0.23	0.47	0.37	0.31	0.31	0.29	0.28	0.34	0.27	0.27	0.26	11.91	11.66	12.06	12.86	11.64	12.32	12.62
CaO	6.36	6.03	5.43	5.98	5.94	5.86	6.28	5.27	6.53	5.58	6.39	6.04	6.37	0.07	0.09	0.06	0.01	0.07	0.01	0.04
TiO_2	0.01	0.00	0.00	0.06	0.01	0.00	0.00	0.00	0.03	0.00	0.03	0.05	0.00	0.00	0.00	0.04	0.03	0.00	0.03	0.02
MnO	0.03	0.00	0.00	0.00	0.00	0.01	0.02	0.00	0.06	0.03	0.00	0.06	0.02	0.00	0.00	0.01	0.02	0.00	0.00	0.00
FeO	0.02	0.06	0.06	0.05	0.01	0.02	0.00	0.00	0.05	0.08	0.21	0.12	0.16	0.01	0.03	0.00	0.02	0.00	0.01	0.00
Tot.	99.77	99.48	99.73	99.68	99.16	99.82	100.07	99.77	99.98	99.78	100.40	99.96	99.74	100.35	99.86	100.03	99.84	99.92	99.89	99.93
Si	2.698	2.702	2.728	2.711	2.713	2.728	2.720	2.743	2.686	2.720	2.693	2.711	2.705	3.017	2.997	3.011	3.012	3.021	3.021	3.025
Ti	0.000	0.000	0.000	0.002	0.000	0.000	0.000	0.000	0.001	0.000	0.001	0.002	0.000	0.000	0.000	0.001	0.001	0.000	0.001	0.001
Al	1.302	1.302	1.274	1.285	1.291	1.267	1.278	1.259	1.315	1.280	1.303	1.285	1.297	1.021	1.031	1.024	1.011	1.009	1.011	1.006
Fe^{2+}	0.001	0.002	0.002	0.002	0.000	0.001	0.000	0.000	0.002	0.003	0.008	0.005	0.006	0.000	0.001	0.000	0.001	0.000	0.000	0.000
Mn	0.001	0.000	0.000	0.000	0.000	0.000	0.001	0.000	0.002	0.001	0.000	0.002	0.001	0.000	0.000	0.000	0.001	0.000	0.000	0.000
Mg	0.000	0.000	0.000	0.000	0.000	0.001	0.000	0.000	0.000	0.001	0.000	0.001	0.000	0.001	0.000	0.001	0.002	0.000	0.000	0.000
Ca	0.304	0.289	0.259	0.286	0.285	0.280	0.299	0.251	0.312	0.266	0.304	0.288	0.304	0.003	0.005	0.003	0.000	0.003	0.001	0.002
Na	0.678	0.682	0.731	0.688	0.683	0.708	0.668	0.734	0.660	0.718	0.676	0.687	0.652	0.178	0.235	0.177	0.162	0.211	0.164	0.145
K	0.013	0.020	0.013	0.027	0.021	0.018	0.018	0.016	0.016	0.019	0.015	0.015	0.015	0.683	0.674	0.695	0.746	0.671	0.712	0.729
Ab	68	69	73	69	69	70	68	73	67	72	68	69	67	21	26	20	18	24	19	17
An	31	29	26	29	29	28	30	25	32	27	31	29	31	0	1	0	0	0	0	0
Or	1	2	1	3	2	2	2	2	2	2	2	2	2	79	74	79	82	76	81	83

Table S7: continued.

2) XRF analyses of migmatites

	Whole rock				Neosome		Leucosome			
	Mtx			Mln	Mtx	Mln	Mtx			Mln
	ALP1	ALP2	ALP3	ALP13	ALP1	ALP13	ALP1	ALP1	ALP1	ALP13
wt%										
SiO_2	71.86	71.16	71.30	74.04	70.64	73.04	73.56	72.49	80.92	74.53
TiO_2	0.47	0.44	0.46	0.30	0.65	0.46	0.16	0.15	0.09	0.07
Al_2O_3	14.53	14.66	14.46	14.09	14.39	14.02	14.54	14.71	10.20	14.14
$Fe_2O_3^*$	3.07	2.87	2.88	2.04	4.28	2.84	1.04	1.03	0.64	0.71
MnO	0.05	0.05	0.05	0.04	0.06	0.05	0.02	0.02	0.02	0.02
MgO	0.75	0.69	0.77	0.50	1.07	0.73	0.27	0.26	0.18	0.21
CaO	1.32	1.19	1.34	1.02	1.39	1.12	1.02	0.93	1.01	0.81
Na_2O	2.20	2.22	2.23	2.31	1.94	2.19	2.33	2.28	1.96	2.32
K_2O	4.65	5.16	5.23	4.84	3.47	4.27	6.13	6.76	4.15	5.83
P_2O_5	0.24	0.24	0.25	0.18	0.29	0.20	0.14	0.14	0.11	0.13
L.O.I	0.72	0.83	0.85	0.54	0.99	0.63	0.48	0.53	0.36	*0.58*
Tot	99.86	99.50	99.80	99.90	99.17	99.55	99.69	99.31	99.64	99.33
ASI	1.31	1.29	1.23	1.29	1.52	1.37	1.18	1.15	1.07	1.22
Mg#	0.49	0.49	0.52	0.49	0.50	0.50	0.50	0.50	0.53	0.54
ppm										
V	50	38	38	28	64	44	17	12	9	10
Cr	27	24	16	21	37	26	<6	<6	<6	7
Ni	11	8	9	6	14	9	4	3	<3	8
Rb	175	207	198	174	180	173	174	197	120	194
Sr	129	120	123	92	97	83	157	153	114	101
Y	19	18	21	17	27	20	7	7	5	6
Zr	159	165	164	111	210	164	63	63	55	19
Nb	12	12	12	8	15	12	6	6	5	<3
Ba	367	367	371	252	235	221	520	562	342	262
La	40	17	40	21	47	40	12	<10	<10	23
Ce	49	56	58	39	89	58	11	27	12	<10
Nd	28	17	22	11	34	27	<10	<10	<10	<10
Pb	20	26	22	42	15	34	30	36	21	48

Table S8: Major and trace element compositions of whole migmatites, neosomes and leucosomes. Mtx: metatexite. Mln: mylonite.
*Total Fe as Fe_2O_3
ASI = mol. $Al_2O_3/(CaO+Na_2O+K_2O)$
#Mg = mol. MgO/(MgO+FeO)

3)EMP analyses of preserved glassy melt inclusions

SiO_2	68.42	71.70	68.95
TiO_2	0.00	0.00	0.24
Al_2O_3	11.57	12.16	11.63
FeO*	1.26	1.26	1.07
MnO	0.19	0.03	0.04
MgO	0.06	0.05	0.10
CaO	0.31	0.25	0.60
Na_2O	3.37	2.96	2.93
K_2O	4.05	4.07	4.45
P_2O_5	0.04	0.00	0.49
Total	89.27	92.47	90.50
Na_2O/K_2O	0.83	0.73	0.66
ASI	1.10	1.25	1.08
#Mg	0.07	0.06	0.14
CIPW norm			
Qtz	31.50	37.21	33.98
Crn	1.19	2.42	1.99
Or	23.92	24.06	26.31
Ab	28.50	25.05	24.78
An	1.25	1.24	0.00

Table S9: EMP analyses of preserved **glassy melt inclusions** in **metatexite**.
*Total Fe as FeO; ASI = mol. $Al_2O_3/(CaO+Na_2O+K_2O)$
#Mg = mol. $MgO/(MgO+FeO)$

Position	n	n	n	n	n	n	n	n	n	n	n	n	n	n	n
SiO_2	74.25	76.01	76.64	76.58	76.93	75.65	73.91	74.22	77.93	76.77	77.81	76.62	75.92	78.04	77.29
TiO_2	0.17	0.00	0.13	0.01	0.00	0.00	0.00	0.00	0.00	0.00	0.12	0.06	0.20	0.02	0.00
Al_2O_3	10.15	11.05	11.28	11.21	10.97	12.04	10.61	11.66	11.22	11.17	11.53	10.81	11.82	11.34	11.16
FeO*	1.31	1.14	0.82	1.34	1.20	0.99	2.05	2.06	1.35	1.41	1.06	1.36	1.25	1.13	1.13
MnO	0.00	0.11	0.00	0.00	0.00	0.00	0.10	0.10	0.04	0.00	0.10	0.10	0.00	0.14	0.00
MgO	0.16	0.12	0.13	0.06	0.13	0.10	0.26	0.31	0.07	0.13	0.04	0.02	0.04	0.07	0.00
CaO	0.17	0.04	0.01	0.10	0.06	0.01	0.00	0.06	0.05	0.04	0.04	0.12	0.09	0.00	0.05
Na_2O	1.63	1.89	2.24	1.68	2.41	2.06	1.76	2.15	2.46	2.30	1.83	1.84	2.83	2.02	2.44
K_2O	5.48	5.11	6.49	6.28	5.89	6.33	6.01	5.93	5.20	5.95	5.26	6.40	5.94	6.20	5.91
P_2O_5	n.d.	n.d.	n.d.	n.d.	n.d.	n.d.	0.48	0.09	0.00	0.04	0.04	0.00	0.09	0.13	0.04
Tot.	93.33	95.46	97.75	97.25	97.59	97.17	95.18	96.58	98.32	97.80	97.83	97.33	98.18	99.10	98.03
Na_2O/K_2O	0.30	0.37	0.35	0.27	0.41	0.33	0.29	0.36	0.47	0.39	0.35	0.29	0.48	0.33	0.41
ASI	1.14	1.27	1.05	1.15	1.05	1.17	1.13	1.16	1.15	1.09	1.32	1.06	1.05	1.13	1.06
#Mg	0.18	0.14	0.22	0.07	0.16	0.15	0.18	0.20	0.09	0.14	0.06	0.02	0.05	0.09	0.00
CIPW norm															
Qtz	42.22	44.16	37.94	41.38	39.05	38.44	38.45	36.74	42.32	39.27	46.10	39.96	35.77	41.40	39.55
Crn	1.23	2.34	0.54	1.47	0.53	1.77	1.20	1.70	1.44	0.95	2.83	0.65	0.73	1.30	0.75
Or	32.36	30.18	38.37	37.10	34.79	37.40	35.52	35.03	30.72	35.16	31.09	37.83	35.10	36.61	34.91
Ab	13.81	16.02	18.99	14.20	20.41	17.45	14.93	18.22	20.85	19.43	15.48	15.59	23.95	17.12	20.63
An	0.85	0.19	0.05	0.50	0.28	0.05	0.00	0.00	0.25	0.00	0.00	0.57	0.00	0.00	0.00

Table S10: EMP analyses of preserved **glassy type I melt inclusions** in **mylonite**. *Total Fe as FeO; ASI = mol. $Al_2O_3/(CaO+Na_2O+K_2O)$; #Mg = mol. MgO/(MgO+FeO); n.d.= not detected; n=MI hosted in neosome garnet; l= MI hosted in leucosome garnet.

Position	n	n	l	l	l	l	n	n	n	n	n	l	n	l	l
SiO_2	76.60	75.68	74.52	78.45	77.59	78.10	76.92	78.14	76.61	74.57	75.98	77.10	75.80	77.06	72.14
TiO_2	0.00	0.00	0.19	0.00	0.09	0.00	0.08	0.06	0.00	0.00	0.00	0.00	0.29	0.03	0.07
Al_2O_3	10.80	11.86	10.21	11.84	11.08	12.06	11.51	11.51	11.31	11.25	12.22	12.35	11.82	11.48	11.33
FeO*	1.11	2.30	2.88	1.45	1.80	1.35	2.05	2.04	1.94	1.90	1.35	1.95	2.02	1.70	2.55
MnO	0.01	0.05	0.17	0.06	0.17	0.00	0.03	0.13	0.21	0.14	0.00	0.08	0.00	0.12	0.09
MgO	0.00	0.30	0.30	0.14	0.29	0.14	0.33	0.17	0.20	0.19	0.20	0.28	0.19	0.18	0.43
CaO	0.06	0.02	0.14	0.06	0.07	0.07	0.12	0.08	0.11	0.12	0.06	0.14	0.07	0.13	0.05
Na_2O	2.17	2.22	1.72	2.32	1.57	1.72	1.83	2.00	1.55	1.31	2.00	1.75	1.96	1.30	1.74
K_2O	5.90	5.58	5.58	5.74	5.74	5.71	5.31	5.46	5.89	5.75	5.87	5.56	5.39	5.58	5.30
P_2O_5	0.00	0.45	0.09	0.26	0.75	0.00	0.31	0.00	0.18	0.53	0.31	0.53	0.39	0.31	0.61
Tot.	96.64	98.45	95.80	100.33	99.15	99.16	98.49	99.59	97.99	95.75	97.99	99.73	97.93	97.89	94.30
Na_2O/K_2O	0.37	0.40	0.31	0.40	0.27	0.30	0.34	0.37	0.26	0.23	0.34	0.31	0.36	0.23	0.33
ASI	1.07	1.22	1.12	1.17	1.24	1.32	1.28	1.23	1.24	1.31	1.25	1.35	1.29	1.37	1.31
#Mg	0.00	0.18	0.15	0.14	0.21	0.15	0.22	0.12	0.14	0.14	0.21	0.20	0.14	0.15	0.22
CIPW norm															
Qtz	40.38	39.03	40.26	41.49	44.49	44.76	43.77	43.44	42.97	42.96	40.47	43.55	42.01	46.38	38.96
Crn	0.75	2.17	1.30	1.80	2.29	2.92	2.75	2.17	2.38	2.87	2.59	3.46	2.76	3.31	2.73
Or	34.85	32.97	32.97	33.94	33.94	33.76	31.39	32.24	34.79	34.00	34.67	32.85	31.88	32.97	31.33
Ab	18.33	18.77	14.55	19.65	13.24	14.54	15.48	16.90	13.12	11.07	16.90	14.78	16.57	10.99	14.69
An	0.28	0.00	0.10	0.00	0.00	0.36	0.00	0.42	0.00	0.00	0.00	0.00	0.00	0.00	0.00

Table S10: continued.

Position	n	n	l	l	l	l	n	n
SiO_2	79.27	78.49	73.73	77.45	73.66	75.11	75.90	74.19
TiO_2	0.09	0.00	0.00	0.19	0.00	0.05	0.08	0.13
Al_2O_3	10.69	10.17	11.59	10.54	12.12	11.51	11.98	11.81
FeO*	1.26	1.36	1.88	1.48	1.72	0.97	0.97	1.09
MnO	0.18	0.00	0.07	0.00	0.20	0.02	0.09	0.09
MgO	0.00	0.00	0.36	0.30	0.28	0.08	0.00	0.15
CaO	0.08	0.00	0.09	0.03	0.07	0.31	0.05	0.50
Na_2O	3.02	2.92	3.09	2.28	3.10	4.07	3.23	2.72
K_2O	3.98	3.86	3.75	3.54	4.62	4.23	3.81	4.01
P_2O_5	n.d.	n.d.	0.49	0.00	0.40	0.13	0.00	0.72
Total	98.57	96.80	95.05	95.81	96.16	96.48	96.11	95.41
Na_2O/K_2O	0.76	0.76	0.82	0.64	0.67	0.96	0.85	0.68
ASI	1.13	1.13	1.25	1.38	1.19	0.97	1.26	1.21
#Mg	0.00	0.00	0.25	0.27	0.20	0.13	0.00	0.18
CIPW norm								
Qtz	45.16	45.59	39.25	49.01	35.91	34.02	41.58	41.90
Crn	1.27	1.19	2.45	2.89	2.02	0.00	2.44	2.99
Or	23.50	22.83	22.16	20.93	27.32	25.02	22.53	23.68
Ab	25.57	24.70	26.12	19.29	26.23	34.46	27.33	23.05
An	0.39	0.00	0.00	0.16	0.00	0.63	0.27	0.00

Table S11: EMP analyses of preserved **glassy type II melt inclusions** in **mylonite**. *Total Fe as FeO; ASI = mol. $Al_2O_3/(CaO+Na_2O+K_2O)$; #Mg = mol. MgO/(MgO+FeO); n.d.= not detected; n=MI hosted in neosome garnet; l= MI hosted in leucosome garnet.

4) EMP analyses of remelted melt inclusions in metatexite

SiO_2	69.19	69.24	70.16	65.34	67.07	70.96	69.22	73.29	72.14	70.54	68.24	69.15	69.45	67.97
TiO_2	0.00	0.00	0.15	0.00	0.08	0.00	0.19	0.00	0.00	0.13	0.09	0.00	0.02	0.14
Al_2O_3	10.98	10.82	10.37	9.98	10.55	11.48	10.47	11.83	13.19	13.29	12.81	12.20	12.43	12.92
FeO*	1.91	1.88	2.29	2.85	1.82	2.09	2.62	2.25	2.41	2.33	2.68	2.39	2.06	4.43
MnO	0.24	0.36	0.18	0.13	0.05	0.00	0.20	0.17	0.05	0.09	0.07	0.19	0.20	0.39
MgO	0.12	0.14	0.15	0.19	0.19	0.18	0.22	0.08	0.16	0.16	0.19	0.17	0.21	0.35
CaO	0.58	0.39	0.33	0.36	0.35	0.56	0.43	0.62	0.51	0.56	0.48	0.44	0.53	0.47
Na_2O	2.81	1.94	2.99	2.25	2.24	2.48	2.50	2.73	2.91	2.02	2.15	2.50	2.16	2.32
K_2O	2.77	3.92	4.20	3.76	4.18	3.25	2.69	4.09	3.14	4.34	4.17	4.48	3.82	4.29
P_2O_5	n.d.	n.d.	n.d.	n.d.	n.d.	n.d.	n.d.	0.09	0.71	0.27	0.13	0.22	0.18	0.48
Tot.	88.60	88.69	90.82	84.87	86.53	91.00	88.55	95.13	95.22	93.71	91.01	91.75	91.05	93.76
Na_2O/K_2O	1.01	0.49	0.71	0.60	0.53	0.76	0.93	0.67	0.93	0.47	0.51	0.56	0.57	0.54
ASI	1.26	1.33	1.03	1.18	1.19	1.33	1.34	1.18	1.45	1.47	1.44	1.25	1.44	1.39
#Mg	0.09	0.10	0.10	0.10	0.15	0.14	0.12	0.05	0.10	0.11	0.11	0.11	0.14	0.11
CIPW norm														
Qtz	38.99	40.03	33.79	34.29	35.51	40.86	40.93	38.57	40.91	39.57	36.62	34.70	39.40	33.64
Crn	2.30	2.67	0.29	1.54	1.71	2.86	2.67	2.00	5.01	4.89	4.21	2.96	4.19	4.47
Or	16.39	23.18	24.80	22.22	24.73	19.19	15.87	24.14	18.53	25.62	24.66	26.50	22.59	25.32
Ab	23.80	16.41	25.33	19.07	18.93	21.01	21.15	23.08	24.63	17.13	18.18	21.15	18.31	19.60
An	2.89	1.94	1.66	1.79	1.72	2.78	2.14	2.51	0.00	1.03	1.50	0.76	1.47	0.00

Table S12: EMP analyses of remelted melt inclusions **at 800 °C, dry conditions**. *Total Fe as FeO; ASI = mol. $Al_2O_3/(CaO+Na_2O+K_2O)$; #Mg = mol. MgO/(MgO+FeO); n.d.= not detected.

SiO_2	68.20	70.06	68.49	69.23	70.21	71.44	70.92	67.61	70.63	69.35	68.05	69.77	72.14	71.57
TiO_2	0.00	0.18	0.00	0.06	0.00	0.00	0.03	0.19	0.02	0.00	0.15	0.05	0.10	0.15
Al_2O_3	11.98	11.56	12.45	10.99	12.46	12.65	11.98	12.76	11.17	13.39	11.55	11.33	11.45	12.92
FeO*	2.37	2.02	3.50	2.28	1.72	2.29	2.05	3.05	2.43	2.72	2.90	1.84	1.93	2.96
MnO	0.14	0.15	0.31	0.15	0.19	0.32	0.25	0.38	0.02	0.05	0.10	0.07	0.20	0.43
MgO	0.30	0.03	0.33	0.09	0.07	0.18	0.14	0.44	0.23	0.27	0.19	0.11	0.15	0.37
CaO	0.51	0.27	0.48	0.48	0.47	0.43	0.51	0.54	0.64	1.07	0.35	0.35	0.35	0.31
Na_2O	2.22	3.86	2.85	2.66	3.44	2.96	1.96	2.53	3.27	3.14	1.88	2.18	2.15	3.40
K_2O	3.96	3.29	4.08	2.97	3.44	4.12	4.36	3.98	3.34	4.51	3.67	3.71	4.22	3.50
P_2O_5	n.d.	n.d.	n.d.	n.d.	n.d.	n.d.	n.d.	n.d.	n.d.	n.d.	0.31	0.22	0.18	n.d.
Tot.	89.69	91.42	92.49	88.92	91.99	94.39	92.19	91.49	91.74	94.50	89.16	89.65	92.88	95.60
Na_2O/K_2O	0.56	1.18	0.70	0.90	1.00	0.72	0.45	0.64	0.98	0.70	0.51	0.59	0.51	0.97
ASI	1.35	1.11	1.25	1.30	1.22	1.25	1.35	1.35	1.10	1.12	1.50	1.37	1.31	1.30
#Mg	0.17	0.03	0.13	0.06	0.06	0.11	0.09	0.19	0.14	0.15	0.10	0.09	0.11	0.16
CIPW norm														
Qtz	36.49	32.69	31.60	39.19	34.36	35.06	39.64	33.09	35.08	28.82	40.40	41.04	41.28	34.43
Crn	3.11	1.15	2.48	2.52	2.24	2.54	3.11	3.29	1.01	1.41	4.49	3.62	3.13	2.96
Or	23.40	19.41	24.14	17.57	20.30	24.36	25.76	23.55	19.71	26.65	21.71	21.93	24.96	20.67
Ab	18.79	32.70	24.08	22.54	29.09	25.05	16.57	21.43	27.69	26.58	15.88	18.44	18.18	28.81
An	2.55	1.35	2.36	2.38	2.32	2.13	2.55	2.69	3.17	5.29	0.00	0.31	0.58	1.54

Table S13: EMP analyses of remelted melt inclusions **at 800 °C**, **wet conditions**. *Total Fe as FeO; ASI = mol. $Al_2O_3/(CaO+Na_2O+K_2O)$; #Mg = mol. MgO/(MgO+FeO); n.d.= not detected.

SiO_2	67.62	67.54	65.83	70.60	68.69	72.12	68.66	69.86	71.94	67.03	66.28	72.62	70.63	71.78	68.47	68.08
TiO_2	0.00	0.26	0.03	0.07	0.00	0.00	0.06	0.13	0.00	0.00	0.15	0.00	0.05	0.06	0.04	0.00
Al_2O_3	12.74	12.39	13.96	12.61	11.42	12.91	10.49	12.05	12.71	14.28	13.65	11.39	12.09	12.99	11.79	12.93
FeO*	2.16	1.91	3.26	2.02	2.68	1.31	2.83	1.54	1.77	2.78	1.64	2.79	2.21	2.38	1.92	1.96
MnO	0.12	0.00	0.57	0.02	0.37	0.00	0.22	0.24	0.25	0.48	0.47	0.23	0.19	0.39	0.45	0.26
MgO	0.30	0.11	0.33	0.14	0.21	0.07	0.24	0.10	0.14	0.44	0.45	0.40	0.20	0.21	0.26	0.23
CaO	0.46	0.43	0.62	0.42	0.46	0.45	0.23	0.33	0.45	0.58	0.41	0.48	0.43	0.36	0.46	0.40
Na_2O	3.31	2.42	2.10	2.35	2.25	3.86	2.32	3.27	3.14	2.70	2.86	2.80	2.43	2.98	2.64	2.50
K_2O	3.96	4.02	3.65	4.55	4.10	4.71	3.85	3.98	4.12	4.25	3.49	4.27	4.11	3.62	3.72	4.14
P_2O_5	n.d.	n.d.	n.d.	n.d.	n.d.	n.d.	n.d.	n.d.	n.d.	n.d.	n.d.	n.d.	n.d.	n.d.	0.00	0.44
Tot.	90.67	89.08	90.34	92.78	90.18	95.43	88.89	91.51	94.52	92.54	89.40	94.97	92.34	94.77	89.74	90.94
Na_2O/K_2O	0.83	0.60	0.58	0.52	0.55	0.82	0.60	0.82	0.76	0.64	0.82	0.65	0.59	0.82	0.71	0.60
ASI	1.21	1.36	1.64	1.32	1.27	1.05	1.25	1.17	1.22	1.41	1.48	1.13	1.31	1.37	1.28	1.39
#Mg	0.19	0.09	0.13	0.11	0.11	0.08	0.12	0.09	0.11	0.19	0.28	0.19	0.13	0.12	0.16	0.15
CIPW norm																
Qtz	29.89	35.60	34.66	36.76	36.05	29.46	37.10	33.33	35.04	30.45	33.10	35.87	37.55	37.24	35.55	35.52
Crn	2.17	3.28	5.44	3.06	2.44	0.63	2.11	1.76	2.27	4.18	4.43	1.30	2.85	3.51	2.59	4.34
Or	23.40	23.77	21.56	26.87	24.21	27.83	22.74	23.55	24.36	25.10	20.60	25.25	24.29	21.41	22.00	24.44
Ab	27.97	20.46	17.77	19.90	19.07	32.70	19.62	27.69	26.58	22.82	24.21	23.66	20.60	25.19	22.34	21.15
An	2.30	2.12	3.06	2.06	2.27	2.24	1.12	1.63	2.22	2.89	2.01	2.36	2.15	1.81	2.26	0.00

Table S14: EMP analyses of remelted melt inclusions **at 750 °C**, **dry conditions**. *Total Fe as FeO; ASI = mol. $Al_2O_3/(CaO+Na_2O+K_2O)$; #Mg = mol. MgO/(MgO+FeO); n.d.= not detected.

SiO_2	66.95	70.18	73.64	68.81	71.14	67.38	69.34	69.80	70.61	64.81	72.27	68.03
TiO_2	0.00	0.00	0.00	0.04	0.06	0.09	0.00	0.01	0.18	0.00	0.05	0.15
Al_2O_3	11.71	12.88	12.39	13.26	12.64	12.30	12.86	12.94	11.83	13.01	12.62	12.65
FeO*	2.53	2.46	2.29	2.45	2.36	2.31	2.75	1.68	2.31	2.40	1.62	2.36
MnO	0.08	0.16	0.25	0.00	0.03	0.34	0.42	0.11	0.07	0.70	0.27	0.09
MgO	0.22	0.14	0.02	0.17	0.25	0.31	0.50	0.33	0.25	0.41	0.23	0.25
CaO	0.45	0.53	0.39	0.60	0.43	0.56	0.74	0.60	0.48	0.56	0.41	0.50
Na_2O	2.68	2.30	3.17	2.38	2.18	1.79	2.98	2.50	2.72	3.04	3.32	2.49
K_2O	3.82	3.61	4.02	4.31	3.96	3.96	4.63	4.36	4.58	2.79	4.33	2.83
P_2O_5	n.d.	n.d.	n.d.	n.d.	n.d.	n.d.	n.d.	n.d.	n.d.	n.d.	n.d.	0.00
Tot.	88.44	92.26	96.18	92.03	93.05	89.03	94.22	92.33	93.03	87.71	95.13	89.34
Na_2O/K_2O	0.70	0.64	0.79	0.55	0.55	0.45	0.64	0.57	0.59	1.09	0.77	0.88
ASI	1.25	1.49	1.20	1.37	1.46	1.49	1.14	1.30	1.15	1.44	1.16	1.57
#Mg	0.13	0.09	0.02	0.11	0.16	0.17	0.22	0.25	0.16	0.19	0.18	0.15
CIPW norm												
Qtz	33.26	39.43	36.79	34.89	40.04	38.00	29.30	35.31	33.96	32.03	33.59	39.35
Crn	2.35	4.22	2.10	3.58	3.98	4.05	1.61	3.01	1.51	3.96	1.71	4.58
Or	22.59	21.33	23.77	25.47	23.40	23.40	27.39	25.76	27.09	16.46	25.62	16.72
Ab	22.68	19.48	26.86	20.18	18.46	15.14	25.19	21.15	23.06	25.75	28.11	21.06
An	2.22	2.63	1.94	2.99	2.13	2.79	3.65	2.98	2.36	2.79	2.04	2.47

Table S15: EMP analyses of remelted melt inclusions **at 750 °C**, **wet conditions**. *Total Fe as FeO; ASI = mol. $Al_2O_3/(CaO+Na_2O+K_2O)$; #Mg = mol. MgO/(MgO+FeO); n.d.= not detected.

SiO_2	73.57	70.30	67.68	67.23	67.67	71.10	68.38	67.96	70.21	71.81	71.65	72.02	72.43	72.50	65.97
TiO_2	0.01	0.08	0.02	0.00	0.00	0.00	0.00	0.00	0.15	0.00	0.23	0.00	0.06	0.00	0.00
Al_2O_3	12.48	10.81	12.41	11.07	11.28	11.96	11.74	11.56	11.31	10.34	11.71	11.36	12.40	11.11	14.08
FeO*	1.82	2.07	2.02	1.86	1.55	1.74	1.60	1.84	1.45	1.94	1.77	1.52	1.42	1.67	1.40
MnO	0.12	0.23	0.45	0.18	0.21	0.17	0.18	0.14	0.11	0.02	0.22	0.11	0.02	0.17	0.21
MgO	0.11	0.12	0.20	0.07	0.26	0.16	0.17	0.11	0.01	0.05	0.19	0.09	0.17	0.06	0.00
CaO	0.43	0.36	0.53	0.53	0.42	0.41	0.46	0.83	0.29	0.42	0.31	0.46	0.36	0.35	0.55
Na_2O	2.48	2.79	3.44	2.42	2.56	2.75	2.84	2.50	3.02	2.38	3.10	2.35	2.82	2.93	3.54
K_2O	4.29	4.76	4.31	4.31	3.72	4.66	3.61	3.67	3.75	3.99	3.56	4.12	3.97	4.51	3.57
P_2O_5	0.21	0.21	0.00	0.76	0.63	0.40	0.22	0.00	0.00	0.00	0.49	0.40	0.09	0.26	0.22
Tot.	95.52	91.72	91.06	88.45	88.30	93.36	89.19	88.62	90.29	90.94	93.22	92.43	93.76	93.57	89.54
Na_2O/K_2O	0.58	0.58	0.80	0.56	0.69	0.59	0.79	0.68	0.81	0.60	0.87	0.57	0.71	0.65	0.99
ASI	1.31	1.04	1.10	1.15	1.25	1.16	1.25	1.20	1.18	1.15	1.23	1.24	1.29	1.07	1.32
#Mg	0.09	0.08	0.12	0.06	0.21	0.13	0.14	0.09	0.01	0.04	0.15	0.09	0.17	0.06	0.00
CIPW norm															
Qtz	40.63	33.64	27.71	34.83	36.67	35.43	35.96	35.75	36.47	40.09	38.24	41.06	38.86	36.56	29.83
Crn	3.48	0.91	1.12	2.42	3.04	2.39	2.85	1.96	1.76	1.34	2.77	3.03	3.01	1.41	3.93
Or	25.32	28.15	25.47	25.49	21.97	27.51	21.32	21.69	22.14	23.55	21.03	24.37	23.48	26.67	21.10
Ab	21.00	23.57	29.09	20.47	21.69	23.30	24.01	21.18	25.55	20.16	26.19	19.90	23.88	24.78	29.91
An	0.76	0.43	2.64	0.00	0.00	0.00	0.86	4.13	1.44	2.08	0.00	0.00	1.23	0.01	1.30

Table S16: EMP analyses of remelted melt inclusions **at 700 °C**, **dry conditions**. *Total Fe as FeO; ASI = mol. $Al_2O_3/(CaO+Na_2O+K_2O)$; #Mg = mol. MgO/(MgO+FeO).

SiO_2	65.74	69.14	70.18	69.26	67.97	71.60	72.57	70.77	68.62	68.03	68.86	70.30	71.80
TiO_2	0.00	0.03	0.01	0.08	0.10	0.11	0.00	0.00	0.26	0.07	0.05	0.02	0.00
Al_2O_3	12.40	11.98	12.03	12.17	12.22	12.40	11.84	12.92	11.39	12.53	11.05	11.78	12.08
FeO*	1.73	1.89	1.27	1.97	1.78	1.99	1.44	1.75	1.82	1.66	2.02	1.35	1.96
MnO	0.19	0.05	0.06	0.30	0.13	0.09	0.17	0.38	0.12	0.25	0.05	0.15	0.14
MgO	0.01	0.11	0.07	0.23	0.16	0.05	0.06	0.16	0.18	0.14	0.18	0.13	0.06
CaO	0.52	0.45	0.45	0.47	0.51	0.52	0.33	0.39	0.52	0.61	0.47	0.32	0.25
Na_2O	3.10	2.25	3.14	2.32	2.34	2.55	3.57	3.81	2.58	2.37	3.02	3.06	2.94
K_2O	3.49	4.24	4.05	4.25	4.22	3.92	4.48	4.02	4.18	3.97	4.34	3.54	4.40
P_2O_5	0.35	0.44	0.22	0.27	0.18	0.40	0.18	0.09	0.11	0.36	0.21	0.00	0.04
Tot.	87.53	90.57	91.47	91.32	89.60	93.62	94.63	94.28	89.78	89.98	90.25	90.65	93.67
Na_2O/K_2O	0.89	0.53	0.77	0.55	0.55	0.65	0.80	0.95	0.62	0.60	0.70	0.86	0.67
ASI	1.26	1.32	1.16	1.31	1.31	1.32	1.05	1.14	1.17	1.35	1.05	1.25	1.20
#Mg	0.00	0.09	0.08	0.15	0.13	0.04	0.06	0.12	0.14	0.12	0.13	0.13	0.05
CIPW norm													
Qtz	32.63	38.10	34.91	37.05	35.85	40.03	33.05	30.63	35.08	37.01	32.30	36.82	35.61
Crn	3.42	3.70	2.21	3.53	3.31	3.95	0.95	1.81	1.92	4.09	1.02	2.33	2.14
Or	20.65	25.04	23.91	25.11	24.96	23.18	26.45	23.77	24.73	23.43	25.63	20.94	25.99
Ab	26.19	19.00	26.53	19.66	19.80	21.57	30.17	32.22	21.85	20.07	25.58	25.90	24.89
An	0.28	0.00	0.77	0.58	1.35	0.02	0.50	1.34	1.88	0.66	0.99	1.58	0.95

Table S17: EMP analyses of remelted melt inclusions **at 700 °C**, **wet conditions**. *Total Fe as FeO; ASI = mol. $Al_2O_3/(CaO+Na_2O+K_2O)$; #Mg = mol. MgO/(MgO+FeO).

5) X-ray maps of nanogranites

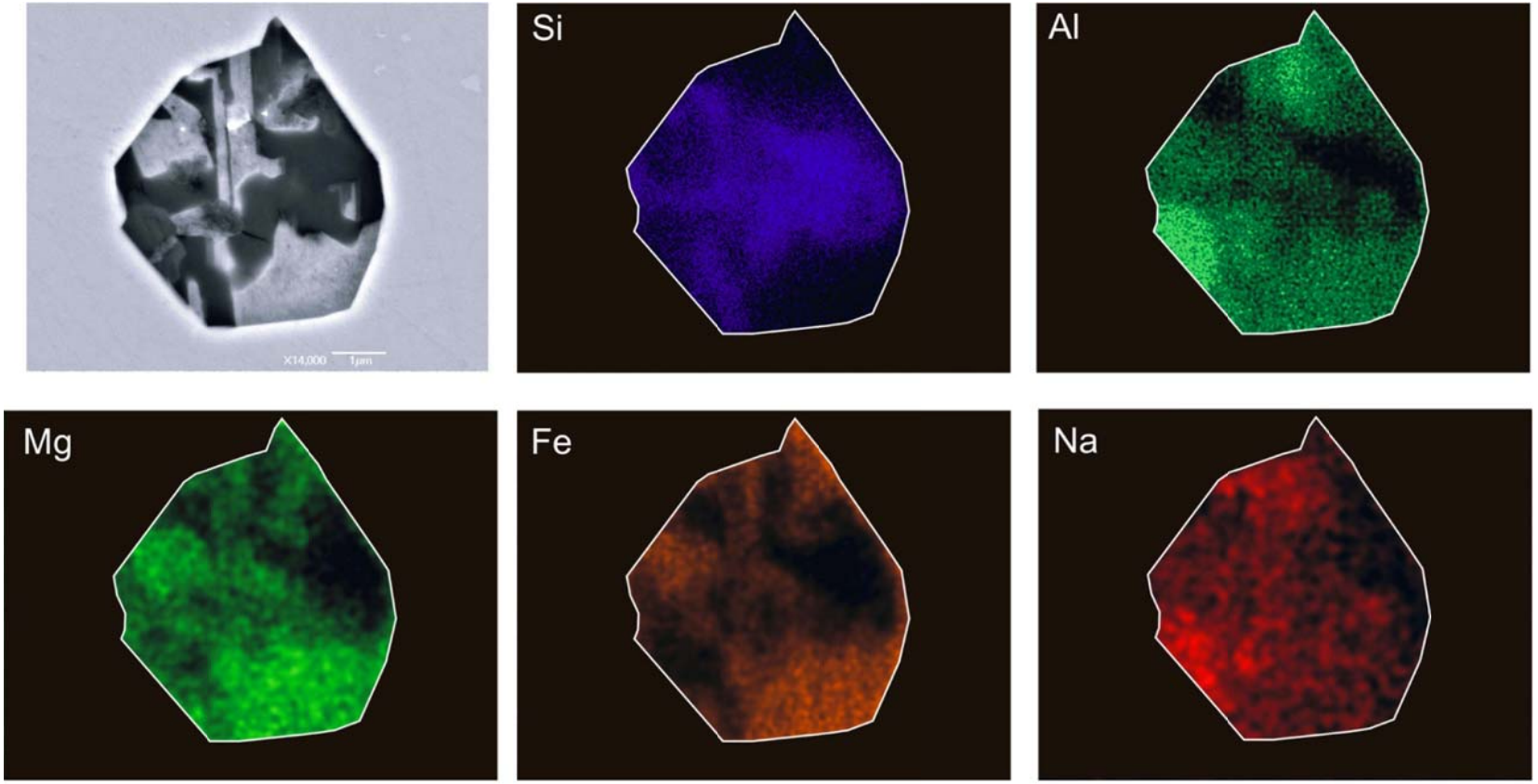

Figure S1: X-ray maps of a nanogranite inclusion in metatexite.

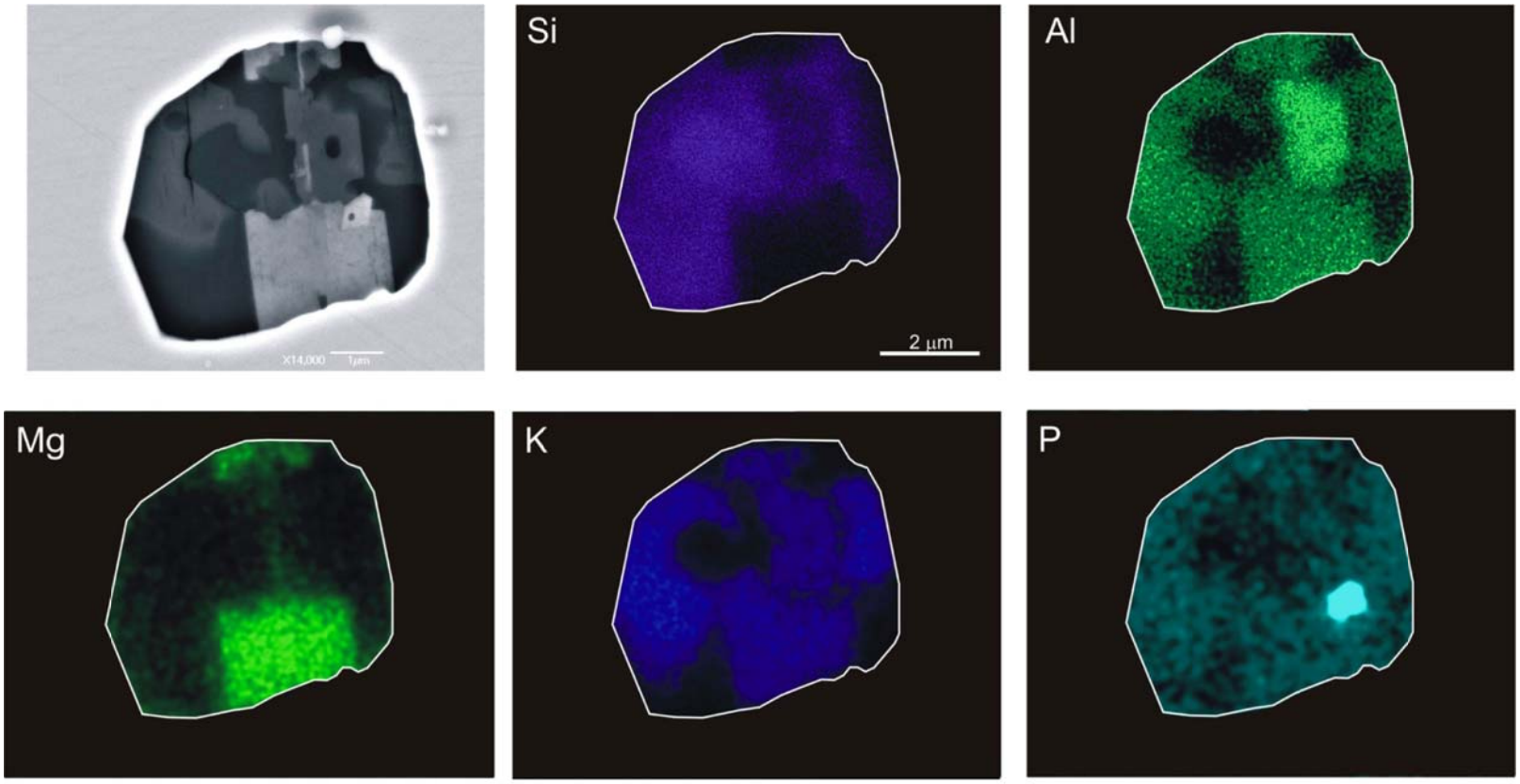

Figure S2: X-ray maps of a nanogranite inclusion in mylonite.

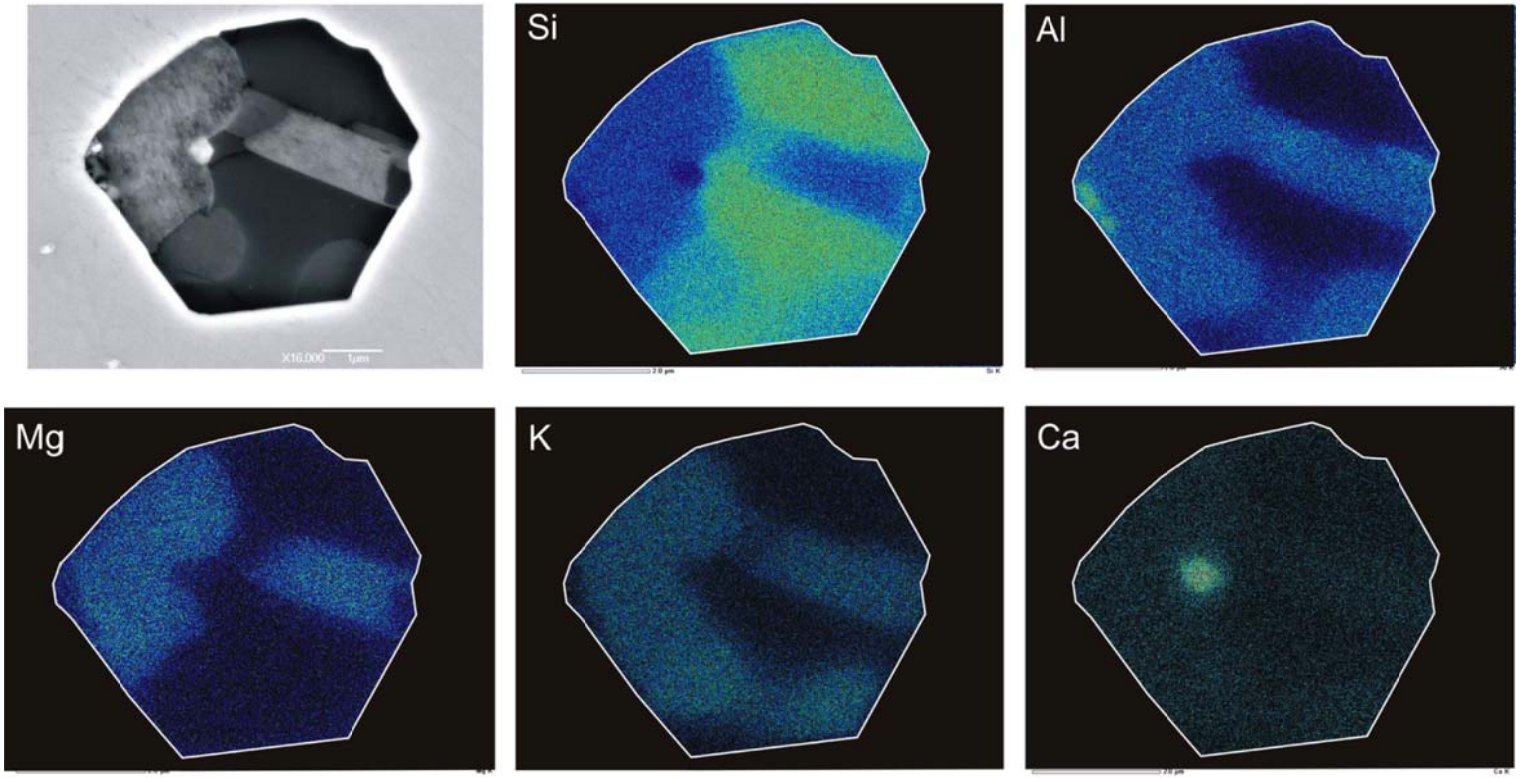

Figure S3: X-ray maps of a nanogranite inclusion in mylonite.